Using Microscopy to Manipulate and Visualize Signal Transduction in Living Cells

Eric Adam Vitriol

A dissertation submitted to the faculty of the University of North Carolina at Chapel Hill in partial fulfillment of the requirements for the degree of Doctor of Philosophy in the Department of Cell and Developmental Biology.

Chapel Hill

2009

Approved by:

Ken Jacobson, Ph.D.

Klaus Hahn, Ph.D.

Gary Johnson, Ph.D.

Keith Burridge, Ph.D.

James Bear, Ph.D.

ABSTRACT

Eric Adam Vitriol

Using Microscopy to Manipulate and Visualize Signal Transduction in Living Cells

(Under the direction of Ken Jacobson, Ph.D. and Klaus Hahn, Ph.D.)

Signaling events in cells are often localized and transient. Understanding how these pathways are regulated in space and time requires the development of new tools that reveal spatiotemporal transduction. Subcellular events can be visualized in real-time by high-resolution light microscopy. Technological advances in live-cell imaging have offered the means to not only observe the phenotypic consequences of signaling events, but to visualize and manipulate the activity of their components. This dissertation describes four studies in which microscopy is implemented to manipulate or visualize signal transduction in living cells. The first study demonstrates contributions to Chromophore Assisted Laser Inactivation, a light-mediated loss of function tool. The second study describes the generation of a new probe to visualize the activation of Src-family kinases. The third study utilizes a biosensor for the GTPase RhoA to reveal novel information about how this signaling component is spatiotemporally regulated in neurons. Finally, the fourth study describes a new computational method for the automated identification and tracking of protein structures called focal adhesions. Together these studies demonstrate the power of using microscopy to gain key insights to the spatiotemporal details of signal transduction.

Dedication

- To my daughter Josefine, who forced me to make my time spent in the lab important so that I could spend every other moment with her.

- To my wife Tracy-Ann, who always made it look so easy.

I love you both dearly.

Acknowledgments

I would like to specifically acknowledge the following people who have helped shape my scientific career:

- My advisors Dr. Ken Jacobson and Dr. Klaus Hahn. It has been an honor and a privilege studying under you both. I became the scientist I am today mainly through the experiences and opportunities you provided.

- My committee members Dr. Gary Johnson, Dr. Keith Burridge, and Dr. James Bear. Thank you for your enthusiasm, guidance, and support. I feel fortunate to have a committee composed of scientists that I have great admiration for.

- Dr. Louis Hodgson, who taught me more about microscopy than any other; and who showed me almost any experiment is possible if approached through determination, hard work, and creativity.

- Dr. Vytas Bankaitis, whose Grantsmanship class for second-year graduate students was the best educational experience of my academic career.

- Dr. Richard Cheney. It was during my interview with him watching movies of Myosin X motility in filopodia that made me realize that I *needed* to become a microscopist.

- Dr. Charlie Ray (Palm Beach Community College), the best teacher that I ever had. Because I enjoyed his classes so much, I took them all. Before I knew it I was majoring in biology and my career path was set in motion.

- To all of my other colleagues and collaborators, to numerous to name. I have had so many positive experiences in my time as an undergraduate, research technician, and graduate student at the University of North Carolina at Chapel Hill. Thank you for helping to make the last years of my life so worthwhile.

TABLE OF CONTENTS

LIST OF TABLES

LIST OF FIGURES

LIST OF ABBREVIATIONS

CAD	Cath.a differentiated
CALI	Chromophore Assisted Laser Inactivation
CDC42	Cell division cycle mutant number 42
CFP	Cyan Fluorescent Protein
CP	CapZ capping protein
DRG	Dorsal Root Ganglion
ECFP	Enhanced Cyan Fluorescent Protein
EGFP	Enhanced Green Fluorescent Protein
EYFP	Enhanced Yellow Fluorescent Protein
FlAsH	Fluorescein Arsenical Hairpin
GAP	GTPase activating protein
GDI	Guanine nucleotide dissociation inhibitor
GDP	Guanosine diphosphate
GEF	Guanine nucleotide exchange factor
GTP	Guanosine triphosphate
KD	Knockdown
KDR	Knockdown/Rescue
FA	Focal adhesion
FALI	Fluorophore Assisted Light Inactivation
FN3	Fibronectin 10^{th} type III domain
FP	Fluorescent Protein
FRAP	Fluorescence Recovery after Photobleaching

FRET	Förster Resonance Energy Transfer
JNK	c-Jun N-terminal kinase
LPA	Lysophosphatidic Acid
MEF	Mouse embryonic fibroblast
Mero 53	Merocyanine dye 53
MERO-CBD	Merocyanine-labeled Cdc42 Binding Domain
MENA	Mammalian Enabled
Myr-RFP	Myristolated Red Fluorescent Protein
NIH 3T3	National Institute of Health; 3-day transfer, inoculum 3 x 10^5
PDGF	Platelet Derived Growth Factor
PTK1	*Potorous tridactylus* kidney 1
RBD	Rho binding domain
ReAsH	Resorufin arsenical hairpin
RHOA	Ras homolog gene family, member A
ROS	Reactive Oxygen Species
SH3	Src Homology 3 domain
SFK	Src Family Kinase
SRC	kinase first identified in the Rous Sarcoma virus
TIR-FM	Total Internal Reflection Fluorescence Microscopy
YFP	Yellow Fluorescent Protein

CHAPTER 1: Introduction

Overview

The complex system of cellular communication consists of a vast array components, pathways, and hierarchical networks. These must be precisely regulated for a cell to function properly. Many signaling events are localized and transient; in part this is how specificity is achieved. To better understand the spatiotemporal component of signal transduction, new tools designed specifically to study it must be developed and utilized. Subcellular events can be visualized in real-time by high-resolution light microscopy. Technological advances in live-cell imaging have offered the means to not only observe the phenotypic consequences of signaling events, but to visualize and manipulate the activity of their components. This allows for a more complete comprehension of how signaling pathways are compartmentalized and temporally controlled.

This dissertation contains three methodologies (Chromophore Assisted Laser Inactivation, Biosensors, and Computer Assisted Image Analysis) that utilize live-cell microscopy to study spatiotemporal signal transduction. Because the biological scope of this thesis is vast, the background of Chromophore Assister Laser Inactivation and Biosensors will be introduced in Chapter 1 and the relevant biology for each study will be disclosed in the introduction section of its respective chapter.

Chromophore Assisted Laser Inactivation

Although analysis of loss of function phenotypes leads to important clues about protein function, long-term global protein inactivation via gene knockout or RNA interference (RNAi) can lead to compensatory changes at the molecular level that are difficult to detect or control. Use of pharmacological inhibitors is limited by a lack of subcellular spatial resolution and transport across the plasma membrane. By contrast, instantaneous and spatially precise protein inactivation through chromophore-assisted laser inactivation (CALI),[1, 2] in principle, avoids these issues. In CALI, a photosensitizer chromophore is attached to a target protein within a cell. An area of interest is then irradiated with an intense beam of light. Absorption of light by the chromophore leads to the production of highly reactive free radicals, including reactive oxygen species (ROS) that in turn inactivate the proximate target(s). Because the free radical species generated during CALI are short-lived, the damage radius has been reported to be limited to proteins that are immediately adjacent to the irradiated chromophore.[3, 4] Given that inactivation can be accomplished within short timescales (often <1 s) and that the inactivating light beam can be directed to small regions within a single cell, the technique provides a spatially and temporally controlled loss of function tool for cell and developmental biology.

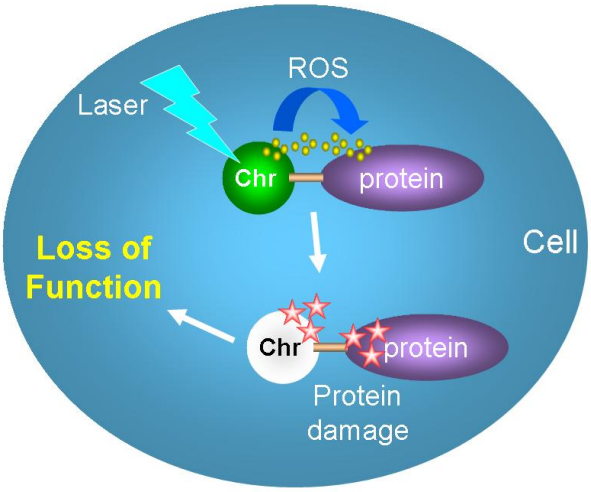

Figure 1.1. CALI schematic. Excitation of the chromophore with laser light leads to production of free radicals, predominantly in the form of reactive oxygen species (ROS). ROS are highly destructive, immediately damaging the protein and destroying the chromophore. However, the short half-life of ROS keeps the destruction radius to just a few nanometers and only the protein directly adjacent to the chromophore is effected. Combined with the ability to direct light anywhere within the cell, CALI has the potential for local and instantaneous loss of function.

Methods for CALI

CALI requires that a photosensitizer chromophore is placed immediately adjacent to a protein of interest. Over the years there have been several creative strategies to achieve light inactivation, with innovations made in both the type of chromophore used and how it is directed to its intended target. Here are the methods used to achieve CALI to date:

Malachite green or fluorescein conjugated antibodies. In the original demonstrations of CALI by D.G. Jay and colleagues, the dye malachite green was conjugated to a target-specific non-function blocking antibody that was microinjected into the cell.[1, 5-19] This methodology is still being employed today.[20, 21] Later malachite green was substituted with the fluorescent dye fluorescein, due to its more efficient generation of free radical species.[22] The use of fluorescein as a photosensitizer also prompted a name change to FALI (Fluorophore Assisted Light Inactivation). Though effective, this technique never became widely used most likely because it combines the

need to microinject live cells and requires a reagent that is not available for most targets (non-function blocking antibody).

FlAsH and ReAsH. More recently, methodologies have been described using membrane-permeable fluorescent ligands that bind to genetically encoded target sequences. These strategies vastly expand the pool of potential CALI targets, as non-function-blocking antibodies that are specific for a single target are fairly rare. They also avoid having to use microinjection for cytoplasmic targets. The first method uses the biarsenical dyes ReAsH (resorufin-based arsenical hairpin binder)[23] and FlAsH (fluorescein-based arsenical hairpin binder).[24] ReAsH and FlAsH have an intrinsic high-affinity interaction with the tetracysteine motif Cys-Cys-Pro-Gly-Cys-Cys (Kd in the pM or lower range). ReAsH-based CALI was used to inactivate connexin 43 that was expressed as a tetracysteine fusion, and loss-of-function was monitored electrophysiologically by the decrease in intracellular coupling mediated by gap junctions.[25] FlAsH was demonstrated to label synaptogamin-I into which the tetracysteine motif was engineered and expressed in synaptogamin-I null Drosophila mutants. CALI of dissected larvae that had been labeled with FlAsH impaired neurotransmitter release from the neuromuscular junction by interfering with the synaptic vesicle post-docking fusion mechanism.[26]

FK-FALI. An alternative targeting strategy was subsequently developed that exploited the high-affinity interaction between FKBP12 (F36V), a protein that binds to the natural ligand FK506, and its synthetic ligand for FKBP12 (SLF′) (Kd ~10 pM).[27] In

this methodology, the protein target is expressed as a fusion with FKB12 and the cell is incubated with fluorescein-labeled SLF′. SLF is membrane permeable and thus avoids the need to microinject any reagents. It was demonstrated that CALI of fluorescein-labeled SLF′ targeted to β-galactosidase could inactivate this enzyme both in vitro and when expressed in fibroblasts.

Environment-sensitive photosensitizers. To reduce off-target effects of non-specific labeling, compounds termed Environment-sensitive photosensitizers (ESPers) have been developed that consist of a CALI chromophore, a targeting ligand and a polarity-sensitive electron-donor moiety, all covalently conjugated.[28] The electron donor quenches singlet-oxygen production by the excited CALI-chromophore in aqueous environments; however, when this new class of CALI reagent is bound to a hydrophobic environment of a target receptor, singlet-oxygen generation occurs and inactivates the receptor. Using this new strategy, the inactivation of the inositol (1,4,5)-trisphosphate [Ins(1,4,5)P3] receptor in DT40 cells was demonstrated by monitoring the inhibition of calcium release from the endoplasmic reticulum (ER) into the cytoplasm upon Ins(1,4,5)P3 stimulation.

Suicide enzyme systems. Recent development of protein tags that form a covalent bond with their ligands has expanded the repertoire of *in vivo* protein labeling. These include HaloTag® and Snap-tag labeling systems: the former utilizes a hydrolase, the latter an alkylase. These genetically-encoded small enzymes are translationally added to the target protein and form covalent attachments at their active sites to their respective

ligands, preventing reaction with additional substrates. For both systems, membrane-permeable fluorescently labeled substrate reagents are commercially available. Additionally, both the enzyme dependent linkage of labeling agent to target protein and the subsequent stable structures that are formed decrease the risk of non-specific labeling. HaloTag® CALI has been demonstrated but only *in vitro*,[29] while CALI of fluorescein labeled α nd γ-tubulin SNAP-tag fusions has been demonstrated in living cells.[30]

Genetically encoded fluorescent protein fusions. There is only one CALI methodology which obviates the need to add any exogenous labeling agents, and that is using fluorescent protein fusions. In both single photon and multiphoton excitation applications, enhanced green fluorescent protein (EGFP), a widely used fluorescent protein, has been shown to be an effective CALI chromophore. Using cells expressing EGFP-α-actinin, CALI was employed to demonstrate that α-actinin provides a mechanical link between stress fibers and focal adhesions.[31] Furthermore, EGFP-connexin 43 expressed in HeLa cells could be inactivated by two-photon excitation with the result that electrical coupling between cells was abrogated.[32] The same study also showed that two-photon CALI of EGFP-Aurora B disrupts mitosis; Aurora B is a kinase essential for mitosis.

Although many fluorescent proteins are weak singlet-oxygen producers, an efficient genetically encoded ROS generator, Killer Red,[33] results in cell lethality at high illumination doses; at lower doses, killer red fusions with pleckstrin homology domains leads to dissociation of the domain from the plasma membrane, indicating specific CALI action. Recent structural analysis has determined that the ability of Killer Red to act as a

super-photosensitizing FP lies within a water channel that connects the chromophore to the environment, allowing a more unrestricted transport of oxygen into and ROS out of the FP β-barrel.[34]

Mechanism of Inactivation by CALI

Overall, several different molecules have been shown to be adequate CALI reagents, as assessed by the production of distinct loss-of-function phenotypes. These results beg the question of how the selective inactivation occurs. CALI-induced photodamage is photodynamic, meaning that, in addition to the CALI reagent acting as a photosensitizer, the process involves light and oxygen. In CALI target proteins are inactivated by ROS. These are generated when chromophores that have become excited through light absorption react with oxygen in the environment. The toxicity of ROS is a consequence of their ability to oxidize proteins, lipids, DNA and carbohydrates.[35] In most cases, the predominant ROS causing CALI is thought to be singlet oxygen ($^1O_2$).[22, 25, 36] Though evidence does exist that CALI can be mediated by other ROS in the case of malachite green (OH radicals)[4] and Killer Red (superoxide anions in addition to $^1O_2$).[33]

Once $^1O_2$ (and other ROS) is produced, it can either react with cellular targets including proteins, nucleic acids and lipids, or be physically quenched by reaction with other compounds in the cellular environment. The reactions with proteins predominate and are of immediate interest for CALI. $^1O_2$ can oxidize side chains of amino acid residues including histidine, tyrosine, tryptophan, methionine and cysteine, leading to both intramolecular and protein–protein cross-linking and aggregation, loss of enzyme and other functional activities.[37, 38] The most detailed information to date regarding the

mechanism of CALI inactivation was obtained by Yan et al.[36], who showed that oxidative photodamage to illuminated FlAsH-labeled calmodulin results in sulfoxide formation on surface methionine residues, which disrupts the binding interface between calmodulin and its partners. No dependence on the distance between FlAsH and particular methionines was found, indicating that reaction with rather than diffusion of $^1O_2$ was rate-limiting. In addition, reactive histidine intermediates were formed, leading to potential cross-linking to binding partners.[36] Crosslinking as also been shown subsequent to *in vitro* EGFP-CALI of glutathione-*S*-transferase.[39]

Caveats of CALI Methods

Successful inactivation of a target protein through CALI depends upon two principal factors: the effectiveness of the chromophore in generating ROS and the reliability of chromophore targeting. It is only when these two factors fruitfully combine that CALI can occur without causing artifacts due to collateral damage. Every methodology involves a trade-off between these two characteristics.

With regards to photosensitization, it is clear that non-specific photodamage can be caused through the absorption of visible light by the cellular environment; the more light used to achieve CALI, the greater the risk. Small molecule dyes of the xanthene family are much better photosensitizers than fluorescent proteins.[40, 41] It can be presumed that because fluorescent proteins (FPs) appear in organisms exposed to sunlight, evolution would require that FPs do not produce abundant ROS upon illumination.[42] With GFP and all other fluorescent proteins, the chromophore is surrounded by a β-can structure of the protein with 'lids' at either end.[43] This physically hinders interaction

between the chromophore and molecular oxygen, the source for singlet-oxygen production. Additionally it prevents release of reactive oxygen products once produced. Presumably this is the reason that it takes much more light (orders of magnitude) to produce a demonstrable CALI effect when EGFP, rather than small organic dyes, is employed as a chromophore.[41]

The super-photosensitizing FP Killer Red subverts the β-can structure through the introduction of a water channel that allows for a less restricted passage of oxygen and its reactive products,[34] thus requiring less light for CALI to occur. However, Killer Red is currently an obligate dimer and may not be suitable for labeling all targets. Additionally, it has a partially mature green intermediate state that is photoresistant until it is photobleached.[34] This requires a pre-bleaching period for Killer Red to reach its full CALI potential.

There also may be such a thing as photosensitizer that is too effective, expanding the damage radius beyond specificity. This question was addressed for fluorescein-CALI and researchers provided compelling evidence by using sensitive transport assays that the inactivation radius for fluorescein extends beyond its immediate target.[44] CALI of a glutamine receptor that modulates N-type calcium channels in neurons was performed. The receptor was modified so that it could be labeled with fluorescein α-bungarotoxin. It was found that CALI significantly affected calcium transport modulated by a glutamate receptor, as expected. However, if the α-bungarotoxin site was engineered into other unrelated transporters, modulation of N-type calcium channels was also reduced. Moreover, even voltage-dependent but receptor-independent modulation of N-type calcium transport could be disrupted by CALI of a non-GPCR labeled with fluorescein α-

bungarotoxin. Other evidence of non-specific damage from fluorescien includes CALI of labeled antibodies to the K_i-67 nuclear protein which caused it to be crosslinked to its upstream binding factor.[45]

Secondly, and of equal importance as chromophore selection, is the targeting method used for directing the chromophore to the protein of interest. If there is any residual chromophore present in the cell after labeling or if it is non-specifically attached to something other than the target then there is a strong chance of collateral damage during irradiation, even with the lower light doses that can be used for strong photosensitizers. Such a risk is incurred by the methodologies that rely on exogenously added labeling reagents that require the washing out of excess unbound chromophore. Non-transfected cell lines that exhibit background staining after incubation with the labeling reagent cannot be used. Dyes such as FlAsH and ReAsH and their antidotes can produce non-specific labeling and resultant toxicity.[46, 47] Specificity can also be problematic when the FKBP12 (F36V) mutant is fused to target proteins; although it is not supposed to be recognized any known proteins except the synthetic ligand conjugated to fluorescein (FL-SLF′), cells incubated with this ligand exhibited appreciable non-specific inactivation.[27]

Summary

As described above, every CALI strategy has its own trade-offs involving choice of chromophore and targeting method. ReAsH-CALI requires minimal light but has a large risk of off-target labeling while EGFP-CALI requires the most light but eliminates the risk of collateral damage due to non-specific labeling. What is clear is that any further

validation of or modification to the above techniques that increases their effectiveness will allow more researchers to utilize these valuable tools to inactivate their protein of choice with spatial and temporal precision. Chapter 2 of this dissertation provides a study about validating and increasing the effectiveness of EGFP-CALI.

Biosensors

Signaling for most cellular process is localized and transient. To better understand how these signals are regulated in space and time, probes need to be developed that not only report the localization about a molecule of interest, and also provide information about its activation state. While some signaling proteins become discretely localized as they assert function, many are broadly distributed and it is only their regulated activity that is spatially discrete (Figure 1.2). For these proteins, biosensors can be used to study their function. Biosensors are fluorescent indicators of activation and are designed for use in high-resolution imaging applications. They offer a living window into the signaling mechanisms of a cell and can yield information about transduction pathways that is not obtainable through conventional methods.

Biosensor Strategy

Biosensors for protein activation consist of two core components: an affinity reagent and a fluorescent binding reporter. The affinity reagent provides the means to localize a specific target within a cell while the binding reporter provides a unique signal that quantifies this interaction (Figure 1.3). The affinity reagent detects activation of a protein either through binding selectively to its activated confirmation or by recognizing

a molecule formed by the activated target (i.e. a phosphorylated kinase substrate or a lipid synthesized by the activated enzyme). The binding of the affinity reagent then leads to a change in fluorescence of the binding reporter via one of several mechanisms: simple accumulation of fluorescent affinity reagent near activated targets, effects on Förster resonance energy transfer (FRET), or fluorescence of environmentally sensitive dyes. Many creative combinations of affinity reagent and binding reporter have been developed. The design of a biosensor can have profound effects both on its capability to detect signaling events and its performance in living cells. Different designs encompass a spectrum of trade-offs between specificity, sensitivity, cell perturbation, and difficulty of use. These design strategies and their pros and cons are discussed below. For the purpose of this introduction, only biosensors that can detect protein activation and be used in living cells will be discussed.

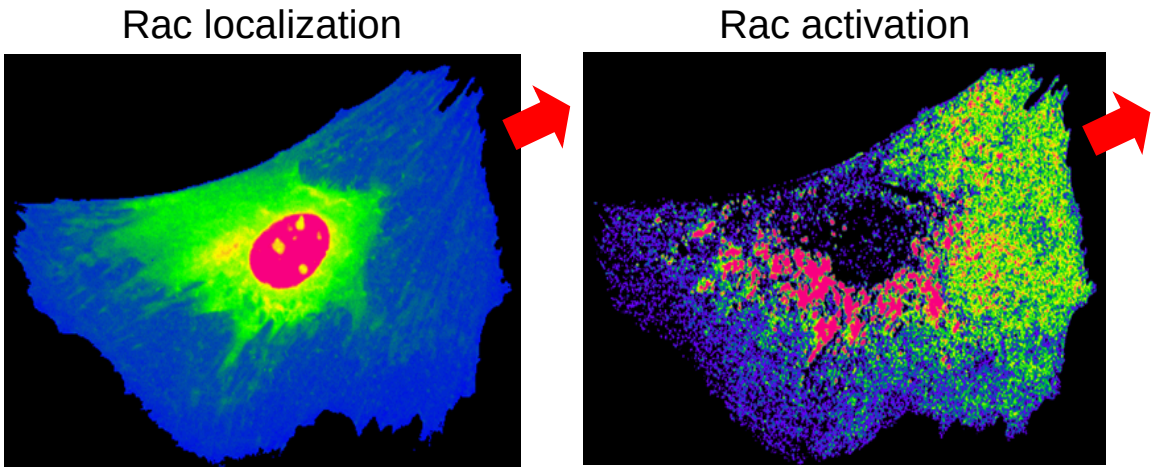

Figure 1.2. Localization vs. activation of signaling proteins. The images above show a fibroblast that is migrating in the direction of the red arrow. Psuedocoloring is used to display fluorescent intensity, with warm colors indicating high intensity. A biosensor for the GTPase Rac is used to distinguish between its localization (left panel) and activation (right panel). Rac is localized diffusely (the increase of intensity around and in the nucleus are due to volume changes in the cell) but is activated in a spatially discrete manner at the front of the migrating cell.[65]

Biosensor Designs

Tagged Domains. There are occasions when an affinity reagent for an activated protein or its modified substrate is robustly localized within the cell. For these cases it may be sufficient to simply label the affinity reagent with a fluorescent protein or dye and observe its subcellular translocation. The two most prevalent adaptations of this concept have used either phosphoinositide-binding pleckstrin homology domains or phosphor-tyrosine binding SH2 domains labeled with a fluorescent protein variant. Using this approach researchers have demonstrated: the redistribution of both phosphatidylinositol 4,5-bisphosphate[48] and tyrosine phosphorylation[49] downstream of cell surface receptor activation; the accumulation of phosphatidylinositol-3,4,-trisphosphate and phosphatidylinositol-3,4,5-trisphosphate at the front of chemotaxing *Dictyostelium*;[50, 51] tyrosine phosphorylation within individual focal adhesions of migrating cells;[52-55] and Src-dependent tyrosine phosphorylation at the tips of growth cone filopodia[56] among numerous other studies. Of note is that though this technique is the easiest to implement, it is also the least sensitive, requiring substantial localization increases over background to visualize discreet signals. It is also most prone to specificity artifacts if the affinity reagent is at all promiscuous. Furthermore, there are many examples in cell signaling where localization of an activated protein or the byproduct its activity cannot be discretely localized (Figure 1.2). For these cases more sophisticated means of reporting binding interactions must be used.

Fluorescence Resonance Energy Transfer. When the binding interactions between an affinity reagent and its target are not robust, one case use Fluorescence

Resonance Energy Transfer (FRET). A fluorescent molecule is excited by light at one wavelength and emits light at a higher, lower energy wavelength. If this fluorophore is paired with a second fluorescent molecule that so that the emission wavelength of one (donor) overlaps with the excitation wavelength of the other (acceptor), excitation of the donor will result in an energy transfer to and excitation of the acceptor if the two fluorophores are within 60-80 Å of each other.[57, 58] The efficiency of this reaction is extremely distance sensitive, determined by the inverse sixth power of the distance between donor and acceptor.[59] FRET is fast, reversible and quantifiable and can thus be used to visualize and measure the interaction between two components with great sensitivity. Affinity reagent specificity is "enhanced" as only interactions with the labeled target will be reported. The caveat of FRET is that it requires numerous processing steps of the raw images to generate the final result.[60, 61] If this is not done with great care, or if the optical configuration of the microscope is problematic, then it is easily possible to generate false positive or negative FRET signals. FRET biosensors come in two different variations: dual-chain and single chain, which are discussed below.

Dual Chain FRET. When two proteins or a protein and an affinity reagent form a direct interaction, dual-chain FRET can occur if one of the partners is labeled with a donor fluorophore and the other an acceptor. FRET is commonly achieved between two fluorescent proteins because of the ease of genetically encoded expression; one of the catalysts for mutating GFP after its discovery was to produce color variations that could undergo FRET.[62] In recent years there have been numerous advances in fluorescent protein biology that have produced excellent FRET pairs.[63] However, FRET between a dye and a FP,[64-66] or between two dyes has also been performed.[67-69] A point-in-case of

this is the biosensor for the GTPase Rac, developed by Klaus Hahn and collegues.[65] The original configuration of the biosensor consisted of Rac labeled with the FRET donor GFP. This portion of the biosensor was genetically encoded. Then an activity-specific binding domain of a Rac effector (PBD) was labeled with the acceptor fluorescent dye Alexa 546. This portion of the biosensor was produced *in vitro* and microinjected into the cell. This biosensor was used to show Rac activation in migrating cells (see Figure1.2 for an example), [65, 70, 71] and in response to integrin regulation[71, 72] and mechanical tension.[73] Subsequently, the same affinity reagent and target where tagged with the genetically encoded fluorescent protein FRET pair (the CFP and YFP variants CyPet and YPet) to produce a biosensor that was entirely genetically encoded with very large dynamic range.[74] The Rac indicator is only one of numerous other dual-chain sensors have been produced.[66, 68, 69, 75-78]

Dual-chain FRET requires the most intensive calibrations and image-processing steps.[61, 79] For example, coefficients for direct acceptor excitation and donor bleedthrough must be calculated and used when quantifying FRET; these should be calibrated with every experiment. Further, variable expression levels of donor and acceptor molecules can change the apparent FRET efficiency. These should be kept as constant as possible, with an ideal 1:1 ratio between donor and acceptor. [61] It is difficult to achieve unimolecular concentrations if the two components must be introduced separately. This is also true at the subcellular level- a loss of FRET will be registered if one of the fluorophores is excluded from a particular compartment.[72]

Single Chain FRET. FRET partners can also be engineered into a single molecule which undergoes a conformational change upon activation. This can occur if the fluorophores are integrated in such a way that that their FRET efficiency changes either through distance or dipole orientation in response a conformational shift of the protein(s) they are attached to. The single-chain approach overcomes the stoichiometry issues associated with dual-chain FRET, guaranteeing a unimolecular concentration and equal subcellular distribution of the two fluorophores. Also, FRET can simply be calculated by exciting the donor and measuring the ratio between the acceptor and donor emissions.[79] Finally, nearly all of the single-chain biosensors made to date have been genetically encoded and are thus easily introduced into cells. All of these features have combined to make single-chain FRET biosensors more widely accessible to biologists than their dual-chain counterparts.

The principal drawback of the single-chain design is the difficulty of orienting the FRET partners on the same molecule so that they undergo a significant FRET shift when the molecule changes conformation. Not every protein undergoes a substantial structural change as it switches between active and inactive states or as it interacts with binding partners. In order to enhance the conformational shift of a single-chain sensor, a popular design has been implemented consisting of the two FRET partners, the target protein, and an affinity reagent that binds the target in an activity specific manner. Each of these is separated by a flexible protein linker; the order of components, linker lengths, and affinity reagent can be all be changed to enhance the maximum FRET response.[80, 81] This strategy has been used successfully for GTPases, kinases and others (reviewed in [81]). However, even when a significant FRET response can be achieved, it is usually on the

order of 30-60% total change from the inactive to active state of the biosensor. This is vastly reduced from the potential dynamic range of intermolecular FP FRET, which can exceed changes of 20-fold.[74] This is most likely due to the constrained movement of the two fluorophores that are covalently linked, preventing them from reaching the upper and lower limits of their FRET potential. Thus with single-chain biosensors sensitivity is sacrificed for ease of expression and calculation of FRET.

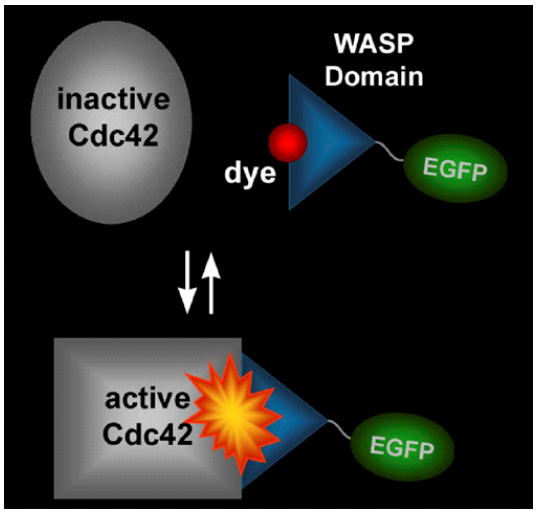

Figure 1.3. Biosensor schematic. Illustrated here is Mero-CBD, a biosensor for the GTPase Cdc42.[83] In this biosensors design, a domain of the protein WASP that only interacts with the active confirmation of Cdc42 serves as the affinity reagent. The binding reporter is an environmentally-sensitive fluorescent dye. When the affinity reagent interacts with active Cdc42, the dye increases its fluorescence intensity. This is measured quantitatively in cells by dividing the intensity of the dye's emission by that of the environment-insensitive EGFP.

Environment-sensitive fluorophores. An alternate approach to reporting binding interactions is to use fluorescent dyes that change their emission in response to their surrounding environment. Many environmentally sensitive dyes have been developed, but few of these have had any applications in living cells. Recently a new class of bright, photostable, water-soluble, solvatochromic merocyanine dyes suitable for live-cell imaging was developed by A. Toutchkine and colleagues.[82] The quantum yield of these merocyanine derivatives is highly related to the polarity of the solvent they are in. This means that in a cellular environment, they will alter their fluorescence intensity as they move from being exposed to the cytoplasm to being pressed against a hydrophobic

portion of a target protein. One of these dyes was incorporated onto a fragment of the protein N-WASP that only interacts with the active form of the GTPase Cdc42 to generate a biosensor for endogenous Cdc42 activation (Mero-CBD).[83] This biosensor exhibited a four-fold change in intensity when the probe was bound to active Cdc42, providing a large dynamic range for sensitive measurements. Mero-CBD has been used to show Cdc42 activation kinetics during cell migration, and to visualize Cdc42 activity in filopodia, the Golgi, and downstream of microtubules.[83-85] Feasibly, this dye or others like it could be attached to affinity reagents for other targets, vastly expanding the suite of tools available to visualize the activation kinetics of endogenous targets.

With domain-based biosensors using an intensity changing fluorescent dye, a second non-responsive fluorophore has to be added to the sensor design to account for intensity changes resulting from volume fluctuations or accumulation of the probe within the cell. Thus, ratio-imaging must be used. Additionally, these dyes do not exhibit the same stability in cells as fluorescent proteins and are not suitable for long-term experiments of more than a few hours.[86] Finally, there is currently no suitable method for introducing protein-based biosensors into cells for imaging purposes so these probes must be microinjected.

Affinity Reagents

Affinity reagents are a critical component to biosensor design. By selectively binding activated targets in cells, they provide the means for sensing conformational changes. Signaling pathway specificity is mediated by the discriminating interactions between its components.[87] Some of these interactions occur through effector binding

regions that are selective only for the active form of their binding partner or for a specific byproduct of a signaling event. To date these domains, isolated from the proteins from which they belong, have been the source for affinity reagents used to make biosensors.

A potential problem from using these affinity reagents is that can inhibit downstream signaling by occupying effector positions, preventing the real effectors from binding the target. For example, the affinity reagent used for a dual-chain biosensor for the GTPase Rac is the p21 binding domain (PBD) from p21-activated kinase. Expression of this domain alone sequesters the GTPase and prevents native effector binding.[88] When used as a biosensor, it is imperative to express it at tracer amounts so that it does not inhibit the signaling events it is trying to detect. Researches who developed the biosensor determined a concentration that could be microinjected into cells that did not inhibit Rac-dependent processes.[65] This issue is most compounded when the affinity reagent is used in a tagged domain or environmentally-sensitive dye based biosensor format. When used for dual-chain FRET, there is additional target that is introduced into the cell which may dampen its inhibition of endogenous processes. An affinity reagent is least likely to perturb in the single-chain format, as it will presumptively only bind to the target to which it is covalently linked.[89]

The second issue with affinity reagents is that they do not exist for many targets. Biosensor engineers are limited to what nature has provided. Even those that exhibit excellent selectivity for the active confirmation of their target may have specificity issues. Once again using PBD of p21-activated kinase as an example, this affinity reagent binds not only to Rac but also to the active confirmation of the similar GTPase Cdc42.[88]

Specificity of this probe is only achieved through FRET with its target. This is how the same affinity reagent has been used as a biosensor for two different targets.[65, 66] To sense endogenous Cdc42 activation with an environmentally-sensitive dye probe, a different affinity domain had to be used.[83] What the biosensor field needs is a way to generate selective and specific binders on a made-to-order basis. It would also be beneficial if these binders recognized the active form of its target without inhibiting its activity or native behavior.

Summary

Biosensors represent a powerful set of tools that can be used to visualize and quantify spatiotemporal signaling events. Every biosensor design has its advantages and limitations; these must be carefully balanced to generate a successful probe. There are two directives that drive the biosensor field. The first is the generation of new probes, either by exploiting existing methodologies or inventing new ones. Chapter 3 of this dissertation will discuss a study regarding the creation of a new biosensor for endogenous Src-family kinase activation based on an artificial affinity reagent that was generated by screening a library of potential biosensor scaffolds. Secondly, biosensors are validated by their subsequent use to generate exciting new biological results. Many probes are made as a proof of concept and then never revisited; the ones that find their way into additional studies are testaments that this approach really does work. Chapter 4 of this dissertation will discuss the use of a single-chain FRET biosensor for the GTPase RhoA to demonstrate novel spatiotemporal RhoA signaling in differentiating neurons.

CHAPTER 2

Enhanced EGFP-CALI using deficient cells rescued with functional EGFP-fusion proteins

Eric A. Vitriol[*†‡], Andrea C. Uetrecht*[†], Feimo Shen[‡], Ken Jacobson*[†§], James E. Bear*[†§]

[*]Department of Cell & Developmental Biology, [†]Lineberger Comprehensive Cancer Center and [‡]Department of Pharmacology; UNC-Chapel Hill, Chapel Hill, NC 27599

[§]Corresponding Author: Ken Jacobson: 120 Taylor Hall, Campus Box #7090, Chapel Hill, NC 27599; Phone: 919-966-5703; Email: frap@med.unc.edu; James E. Bear: 102 Mason Farm Road, Campus Box #7295, Chapel Hill, NC 27599; Phone: 919-966-5471; Fax: 919-966-3015; Email: jbear@email.unc.edu

Abstract

Chromophore Assisted Laser Inactivation (CALI) is a light-mediated technique that offers precise spatiotemporal control of protein inactivation, enabling better understanding of the protein's role in cell function. Enhanced Green Fluorescent Protein (EGFP) has been used effectively as a CALI chromophore and its co-translational attachment to the target protein avoids having to use exogenously added labeling reagents. A potential drawback to EGFP-CALI is that the CALI phenotype can be obscured by the endogenous, unlabeled protein that is not susceptible to light inactivation. Performing EGFP-CALI experiments in deficient cells rescued with functional EGFP-fusion proteins permits more complete loss of function to be achieved. Here we present a novel lentiviral system for rapid and efficient generation of knockdown cell lines complemented with physiological levels of EGFP-fusion proteins. We demonstrate that CALI of EGFP-CapZβ increases uncapped actin filaments, resulting in enhanced filament growth and the formation of numerous protrusive structures. We show that these effects are completely dependent upon knocking down the endogenous protein. We also demonstrate that CALI of EGFP-Mena in Mena/VASP deficient cells stabilizes lamellipodial protrusions.

Introduction

Analysis of loss of function phenotypes often leads to critical insights about protein function. However, long-term global protein inactivation via gene knockout or RNAi can lead to compensatory changes at the molecular level that are difficult to detect or control. Chromophore Assisted Laser Inactivation (CALI) circumvents these issues through instantaneous and spatially precise protein inactivation.[1] With CALI, target proteins are inactivated by reactive photoproducts such as reactive oxygen species (ROS) that are generated by intense irradiation of photosensitizer chromophores.[15] The short half-life of these ROS ensures that only proteins immediately adjacent to the chromophore are affected.[3] CALI has been used to inactivate varied protein targets, but some skepticism remains about the specificity of this approach and its general applicability.

CALI specificity is achieved by selectively labeling the target protein with a chromophore. This was originally done by microinjecting non-function blocking antibodies labeled with malachite green or fluorescein into cells[2], a methodology that has proven to be technically difficult and has only been used by a limited number of laboratories. More recently CALI strategies have been developed that utilize membrane permeable chromophore components that recognize genetically encoded tags. These include the biarsenical dyes FlAsH[26, 90] and ReAsh[25] which specifically recognize 12 amino acid tetracystine motifs, and a fluorescein-conjugated ligand (SLF') whose intracellular target protein is FKBP12(F36V) .[27] These membrane permeable labeling strategies have increased the potential utility of CALI, but still suffer from having to use

exogenously added reagents which introduces the risk of non-specific labeling and collateral photodamage during irradiation.[25, 44]

A third CALI approach is to use fluorescent proteins as photosensitizers. CALI using fluorescent protein fusions offers the unique advantage of having a CALI system in which all of the components are genetically encoded, thereby avoiding having to label the protein of interest with exogenous reagents. Co-translational attachment of the fluorescent protein to its target provides the highest possible degree of specificity. EGFP is a widely used fluorescent protein that has been previously shown to be an effective CALI chromophore with both single photon[31] and multiphoton excitation[32]. While EGFP has many advantages for studies of protein localization, the drawback to using this fluorescent protein as a CALI chromophore is that it is a relatively poor photosensitizer. This must be compensated for by using irradiation doses that are substantially higher than what is needed for inactivation by fluorescein, FlAsH, or ReAsH.[41] Any changes in the experimental procedure of EGFP-CALI that improves its efficacy would allow more researchers to use this technique to locally and acutely inactivate proteins using CALI while retaining the benefits of EGFP as a localization tool.

One such improvement would be to perform CALI experiments in cells where the only functional version of the protein is EGFP-labeled. The presence of endogenous, unlabeled protein that is resistant to light inactivation has the potential to compensate for the loss of EGFP-tagged proteins, and can therefore mask the CALI effect. To address this problem one can use cells that are deficient for the endogenous protein and rescued with the EGFP-fusion complement. To facilitate production of complemented cell lines, we present a novel system where knockdown of endogenous protein and rescue with an

EGFP-fusion protein can be accomplished in a single step. We demonstrate the CALI of EGFP-Capping protein (CP) in rescued deficient cells and show that knockdown of the endogenous protein is essential for CP loss of function following laser irradiation. As a second example of this approach, we also demonstrate the CALI of EGFP-Mena in rescued fibroblasts derived from Mena$^{-/-}$VASP$^{-/-}$ mice.

Capping protein and Mena both localize to the barbed ends of actin filaments where they either negatively or positively regulate filament elongation; antagonism between the two factors governs the supramolecular organization of actin filaments in motile cells and has a profound effect on motility and migration.[91-98] With EGFP-CALI, we recapitulate the loss-of-function phenotypes of Capping protein and Mena reported previously: CALI of capping protein creates a local increase in barbed ends and F-actin resulting in numerous protrusive structures,[99] while CALI of Mena induces larger and more stable lamellipodial protrusions.[95] CALI of CP and Mena cause distinct changes in local subcellular structure despite the overlapping localization of both proteins at the leading edge. In both cases, the phenotypic changes that occur upon CALI are positive (eg. the generation of a new structure), strongly suggesting that CALI is leading to highly specific protein inactivation under these conditions.

Results

A lentivirus system for single-step generation of deficient cells complemented with EGFP-fusion proteins. In order to rapidly generate knockdown cells rescued with a functional EGFP-fusion protein, we modified a lentiviral vector to concomitantly express an shRNA from the PolIII U6 promoter and a functional EGFP-fusion protein from the 5'

LTR promoter of the Murine Stem Cell Virus (MSCV) (Fig. 2.1*A*). The LTR promoter drives modest expression levels,[93] a detail that is important if a physiological level of the rescue protein is desired. This simultaneous knockdown/rescue system requires the complementing EGFP-fusion protein to be resistant to the RNAi due to mismatches in the RNAi target sequence. This system allows the production of deficient cells rescued with EGFP-fusions without having to generate a knockout mouse or having to perform multiple transfections with siRNA oligonucleotides and/or expression vectors. An additional advantage of simultaneous knockdown/rescue is that knockdown occurs in the presence of a functional copy of the knocked down gene, reducing the risk of coordinate regulatory and compensatory changes as the endogenous protein is lost.

Capping protein (CapZ, abbreviated CP throughout) is an obligate heterodimer of alpha and beta subunits and is the predominant actin filament capping protein in most cells.[100] To create a knockdown/rescue vector for CP, we utilized an shRNA that specifically targets rat CapZβ and an RNAi-resistant EGFP-human CapZβ (hereafter referred to as EGFP-CP) fusion. The phenotypic effects of CP knockdown using this shRNA sequence have been previously characterized and serve as a useful point of comparison for our studies.[99] The loss of CP has dramatic effects on the actin cytoskeleton, most notably a substantial increase in filopodia. We confirmed this phenotype by infecting Rat2 fibroblasts with a version of the lentiviral vector that expresses only the knockdown shRNA, but not the rescue component (Fig. 2.1*B*, middle panel). In addition to increased filopodia, we also observed a large increase of ruffling in these cells (data not shown). Both of these effects are consistent with loss of CP activity and the subsequent increase in uncapped and rapidly growing actin filaments.

We infected Rat2 fibroblasts with the CP knockdown/rescue lentivirus and identified a clonal derivative with no detectable expression of endogenous CPβ that was complemented with a physiological level of EGFP-CP (Fig 2.1*C*). This knockdown/rescue cell line was phenotypically indistinguishable from the control Rat2 cells (Fig. 2.1*B*, top and bottom panels), indicating that the EGFP-CP functionally complemented the shRNA-induced phenotype. This is consistent with data showing that *Xenopus* CPβ tagged with EGFP at the same terminus is functional and has similar on-rate and dissociation constants to actin barbed ends as unlabeled CP.[101]

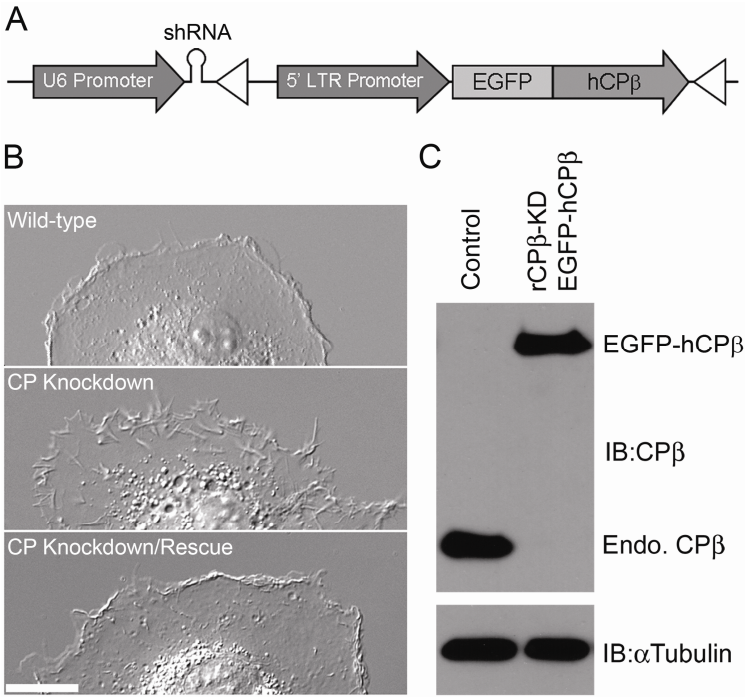

Figure 2.1. A lentiviral system for simultaneous knockdown and rescue with a functional EGFP-fusion complement. (*A*) Schematic of the lentiviral expression vector used for simultaneous knockdown of rat CPβ (rCPβ) and rescue with EGFP-human CPβ (EGFP-hCPβ), open triangles represent LoxP sites. (*B*) DIC images of a wild-tpe Rat2 fibroblast (top panel) and Rat2 fibroblasts infected with only the knockdown portion of the vector (middle panels) or the complete knockdown/rescue construct (bottom panel), scale bar is 20μm. (*C*) Western blot of wild-type Rat2 fibroblasts (left lane) and a clonally derived Rat2 cell line infected with the knockdown/rescue vector.

CALI of EGFP-CP acutely induces the formation of dorsal protrusions in deficient cells, but not in cells retaining endogenous CP expression. We performed CALI of EGFP-CP in both knockdown/rescue (KDR) cells and cells which expressed EGFP-CP without knockdown of the endogenous gene. In both cell lines, EGFP-CP was expressed a comparable levels (data not shown). Cells were irradiated with light from the 488nm

line of an argon ion laser focused on the specimen plane with a beam diameter of about 23μm (approximately 1/4 to 1/6 of total cell area; Fig. 2*A*, white circle). After administration of 100ms dose of 1.5 mW/μm^2 laser light, KDR cells exhibited dynamic changes on the dorsal surface of the cell, forming numerous protrusions (Fig. 2.2*A* and *B*). However, in contrast to the filopodia phenotype that is seen with long-term CP depletion (Fig. 2.1*B*, middle panel) many of these structures most strongly resembled intrapodia, actin-based protrusions that occur on the dorsal surface of migrating growth cones.[102, 103] The difference may represent the effects of long-term vs. instantaneous loss of CP. The formation and curvilinear extension of these protrusions was exclusive to the area that was irradiated (Fig. 2.2*A*). When these cells were irradiated with a smaller beam size (5μm; 6.1 mW/μm^2), no change in the dorsal surface was apparent (data not shown), despite the increase in photon flux. These data are qualitatively consistent with the rapid fluorescence recovery after photobleaching kinetics for EGFP-CP (Table 2.1: note that diffusional recovery would scale as bleached region diameter squared and substantial recovery would therefore only occur after approximately 150s, a time in agreement with when the phenotype begins to reverse as seen in Figure 2*D*) and suggest that the CP CALI effects require inactivating a large enough fraction of the EGFP-CP pool to avoid rapid compensation from intact, non-irradiated EGFP-CP diffusing in from surrounding areas.

When cells expressing EGFP-CP without knockdown of endogenous CPβ were irradiated with the full light dose, no detectable effect was observed (Fig. 2.2*B*), indicating that the unlabeled endogenous CP in these cells is resistant to CALI and completely masks the effect of EGFP-CP inactivation. As an additional control, we

irradiated Rat2 cells expressing soluble EGFP to test for nonspecific laser-induced effects and again observed no morphological change in the irradiated area.

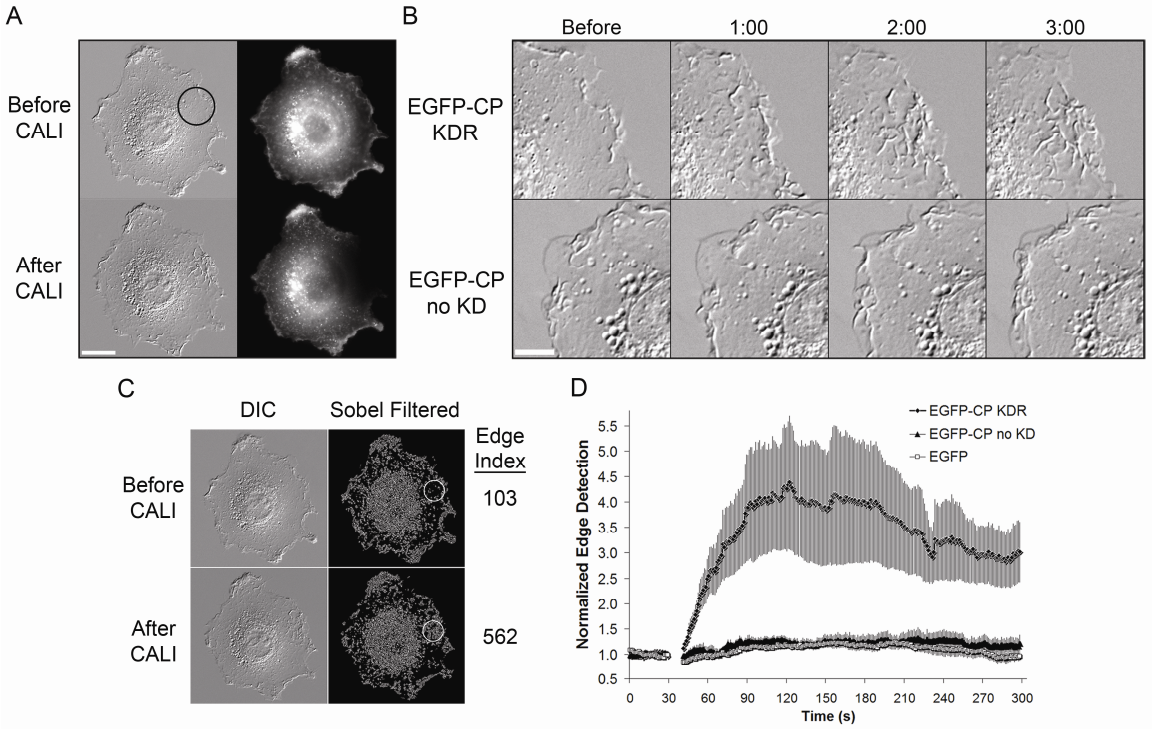

Figure 2.2. CALI of EGFP-CP induces the formation of dorsal ruffles and filopodia only in the knockdown/rescue background. (*A*) DIC images of Rat2 EGFP-CP knockdown/rescue (KDR) cell line before and three minutes after CALI of EGFP-CP (left panels) and fluorescent images of EGFP-CP before and immediately after CALI (right panels), area of irradiation is indicated with a black circle, scale bar is 20μm. (*B*) Time-lapse images of the irradiated regions of EGFP-CP KDR cells (top panels) and cells expressing EGFP-CP without knockdown of endogenous CP (EGFP-CP no KD, bottom panels) before and after CALI, scale bar is 10μm. (*C*) DIC images (left panels) and Sobel filtered binary images (right panels, for details see Methods) before (top panels) and two minutes after (bottom panels) CALI. The white circle represents the 12μm diameter center of the irradiated area that was used to measure the local edge detection index. Raw edge index values are shown next to their respective images. (*D*) Plot showing the normalized edge detection values in the irradiated region over time for EGFP-CP KDR cells (n = 20), EGFP-CP no KD cells (n = 8), and cells expressing EGFP (n = 12), the break in each line represents when the movies were paused to perform laser irradiation, error bars are s.e.m.

To objectively quantify the magnitude of the morphological effect induced by CALI, we analyzed the DIC time-lapse images with an edge detection method (see Methods for details). Application of a Sobel edge detection kernel to DIC images resulted in increased edge detection in regions that contained dorsal structures (Fig. 2.2*C*). A normalized index of these structures was generated and plotted against time to display the kinetics of this event (Fig. 2.2*D*). CALI of EGFP-CP in KDR cells resulted in an immediate increase in dorsal structures that peaked at approximately 80s after irradiation. This activity then gradually declined (Fig. 2.2*D*) until it eventually returned to pre-CALI levels (10-15min after irradiation, data not shown). The same quantification scheme applied to cells expressing EGFP-CP (no knockdown) or EGFP alone showed no detectable increase in edge content in the irradiated area (Fig. 2.2*D*).

CALI of EGFP-CP induces a local increase in dorsal F-actin and barbed ends. The morphological changes induced by CALI in the KDR cells were consistent with loss of actin filament capping activity, but we sought to confirm the underlying mechanism of this effect using fluorescent assays of filament growth. To verify that the dorsal protrusive structures observed after CALI of EGFP-CP in KDR cells contained F-actin, cells were fixed and stained with fluorescent phalloidin after laser irradiation. There was perfect co-localization between the phalloidin signal and the dorsal protrusive structures observed with CALI treatment (Fig. 2.3*A*), showing that the dorsal protrusions induced by CALI were actin-based.

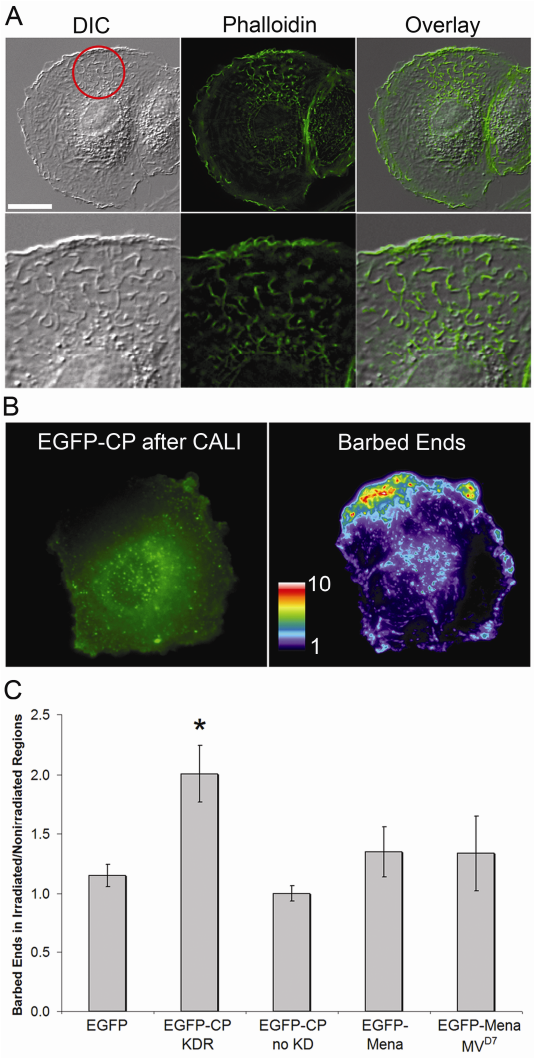

Figure 2.3. CALI of EGFP-CP in KDR cells generates a local increase in barbed ends of actin filaments and dorsal F-actin. (*A*) DIC image (left panel), fluorescent image of Alexa568-labeled phalloidin from a deconvolved three-dimensional stack (center panel), and overlay (right) from an EGFP-CP KDR cell after CALI, area of irradiation is represented by the red circle, scale bar is 20μm.The bottom panels are zoomed versions of the top panels. (*B*) Fluorescent image of EGFP-CP immediately after laser irradiation (left) and a pseudocolored fluorescent image of actin filament barbed-ends labeled with Alexa568-conjugated G-actin at 3 minutes post-CALI. (*C*) Graph showing the relative barbed end increase in the irradiated regions of Rat2 fibroblasts expressing the following contructs: EGFP (n = 12), EGFP-CP KDR (n = 19), EGFP-CP no KD (n = 7), EGFP-Mena (n = 9), and Mena/VASP null MEFs (MV^{D7} cells) expressing EGFP-Mena (n = 5), error bars are 95% C.I, asterisk indicates $p < 0.01$ compared to all other groups (Tukey's HSD post-hoc test; ANOVA $p = 6.8 \times 10^{-8}$).

Acute loss of CP activity should result in an increased number of barbed ends and enhanced filament growth. To test for increased numbers of barbed ends after CALI of EGFP-CP, we utilized a fluorescent assay that specifically detects them. This assay involves gently permeabilizing cells and adding fluorescently labeled actin monomers that polymerize onto free barbed ends *in situ*. Following fixation, the fluorescent signal quantitatively reports the density of free or growing barbed ends in a particular cellular location[104]. We compared the barbed end signal of the irradiated region with similar non-irradiated regions in the CALI-treated cells. CALI of EGFP-CP in KDR cells produced a two-fold average increase in barbed ends where the cells were irradiated (Fig. 2.3*B* and

C), while there was no detectable increase when we irradiated non-knockdown cells expressing EGFP-CP or soluble EGFP (Fig. 2.3*C*). As an additional control to ensure that the local barbed end increase was due to *bona fide* CP loss of function and not to non-specific damage caused by irradiating EGFP at the ends of actin filaments, we also irradiated EGFP-Mena in Rat2 and in Mena/VASP null fibroblasts (MV^{D7} cells). In both cell lines, no significant barbed end increase was observed in the irradiated area (Fig. 2.3*C*).

CALI of EGFP-Mena in rescued deficient cells induces larger, more stable lamellipodial protrusions. To verify the increased effectiveness of EGFP-CALI in the absence of endogenous proteins, we performed CALI of EGFP-Mena in the Mena/VASP null MV^{D7} cells. Loss of Mena/VASP at the leading edge of migrating cells results in altered lamellipodial dynamics: lamellipodia protrude more slowly and persist for longer periods, which correlates with faster whole cell migration speeds.[93] MV^{D7} cells rescued with EGFP-Mena were irradiated for 300ms with a laser power of 6.1 $mW/\mu m^2$ distributed over a 5μm diameter beam. Irradiation parameters were changed from the CP experiments because FRAP analysis of EGFP-Mena revealed less total recovery and slower recovery kinetics than EGFP-CP (Table 2.1), indicating that CALI could be performed in smaller regions. Also MV^{D7} cells are approximately 50% smaller than Rat2 fibroblasts. Lamellipodial protrusions were analyzed using kymography, which characterizes the kinetic signature of lamellipodia undergoing cycles or protrusion and retraction.[40, 95]

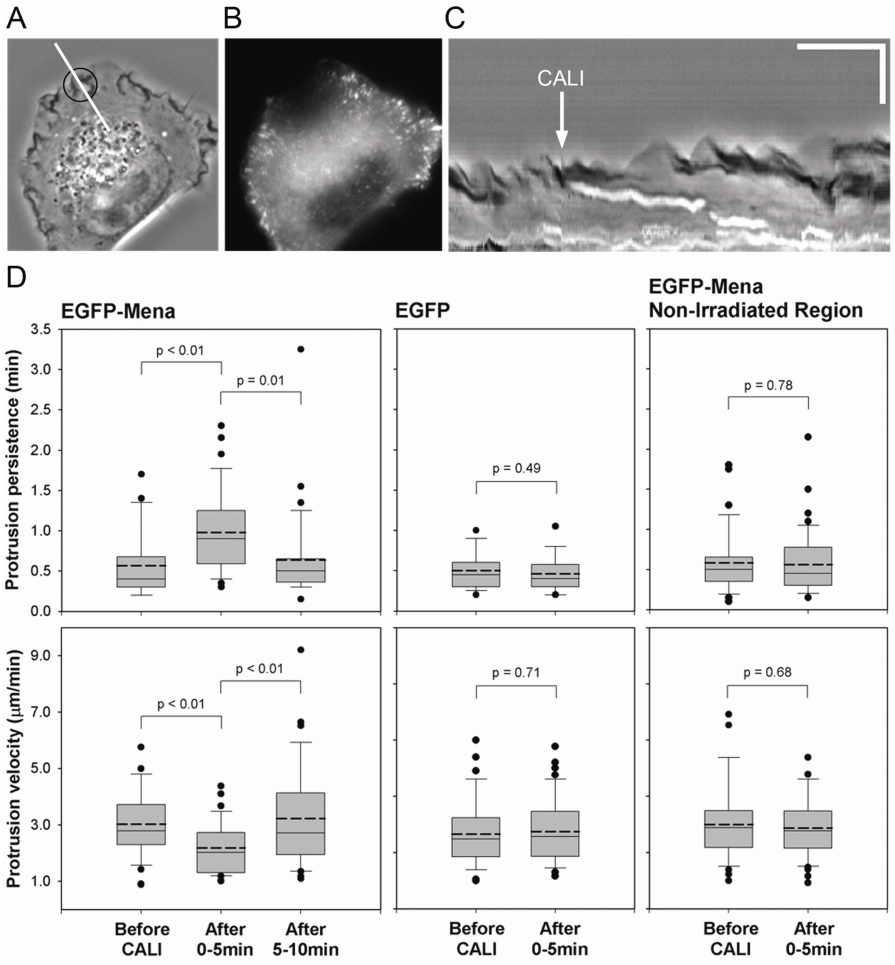

Figure 2.4. CALI of EGFP-Mena in Mena/VASP deficient cells induces more stable lamellipodial protrusions. (*A*) Phase contrast image of an MV^{D7} cell (*B*) fluorescent image of EGFP-Mena immediately after laser irradiation and (*C*) kymograph of a representative EGFP-Mena CALI experiment (*A*) area of irradiation is indicated with the black circle, the line used to generate the kymograph in is indicated by the white line. (*C*) horizontal scale bar is 3min, vertical scale bar is 5μm. (*D*) Box and whisker plots displaying results from kymograph analysis. Kymographs were drawn in the irradiated regions of cells expressing either EGFP-Mena (34 protrusions before CALI, 38 protrusions 0-5min after CALI, 34 protrusions 5-10min after CALI, n =11 experiments), or EGFP (39 protrusions before CALI, 49 protrusions after CALI, n =9 experiments), and also in the non-irradiated regions of cells expressing EGFP-Mena (37 protrusions before CALI, 53 protrusions 0-5min after CALI, n = 11 experiments). The top whisker indicates the 90^{th} percentile, the top line of the box is the 75^{th} percentile, the middle line of the box is the 50^{th} percentile, the bottom of the box is the 25^{th} percentile, the bottom whisker indicates the 10^{th} percentile, the mean is indicated with the dotted line, and outlying points are shown as closed black circles, p-values for EGFP-Mena experiments are Tukey's HSD post-hoc test (persistence ANOVA p = 0.01, velocity ANOVA p = 0.02), p-values for all other experiments are from student's t-test.

One of the hallmarks of using CALI to subcellularly inactivate target proteins is that the effect should be reversible providing that there is sufficient exchange of non-irradiated and irradiated protein: fluorescence recovery is indicative of nondamaged protein entering the effected region. FRAP analysis of EGFP-Mena revealed that there was a substantial local exchange of Mena (Table 2.1). [Note that while lateral transport of "unCALI'ed" protein is a requisite step in local functional exchange, additional reactions at barbed ends may delay the complete restoration of functionalilty.]

To test for reversibility of the CALI effects, protrusion parameters from these experiments were grouped into three categories: before CALI, 0-5min after CALI, and 5-10min after CALI. Irradiation of EGFP-Mena at the leading edge resulted in a transient change in lamellipodial dynamics: protrusion persistence increased while protrusion velocity decreased in the first 5 min after CALI (Fig. 24*C* and *D*). This occurred in a manner that was consistent in direction and magnitude with previously published results.[95] Both protrusion parameters returned to pre-CALI levels 5-10 min after irradiation (Fig. 2.4*C* and *D*), showing the CALI effect was in fact reversible. Also, the effect was limited to the subcellular area that was irradiated as no effect on lamellipodial dynamics was observed in non-irradiated regions (Fig. 2.4*D*). To test for nonspecific effects of local fluorophore excitation, we irradiated MV^{D7} cells expressing soluble EGFP and observed no effect on lamellipodial dynamics (Fig. 2.4*D*).

Table 2.1 Cytoplasmic mobility of Capping Protein and Mena

Protein	Cell line	Percent Recovery	$t_{1/2}$ (s)	n
EGFP-CP	Rat2 EGFP-CP KDR	69.2 ± 1.9	6.6 ± 0.4	14
EGFP-Mena	MV^{D7}	50.3 ± 5.6	17.4 ± 3.9	10

Values are reported ± s.e.m

Discussion

Our results support a number of important conclusions about the use of EGFP as a CALI chromophore and more generally about the CALI technique. First, despite its low efficiency production of reactive photoproducts, our studies demonstrate that EGFP can be an effective CALI chromophore, confirming previous work.[31, 32] Using two different proteins, we show that light-induced inactivation of functional EGFP-fusions lead to expected loss of function phenotypes. Second, EGFP-CALI can lead to highly selective protein inactivation without significant non-specific photodamage. In the two examples of CALI reported here, the loss of function phenotypes induced by CALI led to positive changes in cellular structures or behaviors, suggesting that the effects are highly specific. Third, CALI of some proteins requires the elimination of unlabeled endogenous protein to be effective. Our knockdown/rescue lentivirus system will greatly facilitate the generation of cell lines meeting this criterion. Finally, different proteins will require empirically developed CALI regimes based on the rate of exchange between bound protein and the cytosolic pool as well as the diffusional mobility of the protein in the cytoplasm.

Is EGFP a suitable live-cell CALI chromophore? The answer is yes, but it must be recognized that EGFP is a low efficiency photosensitizer and requires excitation with intense light to achieve CALI. Neither a 100W mercury arc lamp nor laser scanning confocal illumination produced CALI phenotypes in the EGFP-CP KDR cells (data not shown). At this juncture, suitable irradiation sources for EGFP-CALI include focused 488nm laser light from high-powered Argon ion lasers or multiphoton excitation using a frequency doubled Ti-sapphire laser.[32] However, the high-energy requirements of EGFP-CALI hold a hidden benefit: routine imaging and protein inactivation can be performed separately since very distinct excitation regimes are required for normal imaging and target inactivation. Newly developed fluorescent proteins such as Killer Red produce reactive photoproducts much more efficiently, and therefore illumination must be carefully controlled to avoid unintended photodamage during imaging.[33] Moreover, since many functional EGFP fusions already exist, this technique can readily be applied to many proteins with minimal time spent generating new reagents.

Is protein inactivation by EGFP-CALI specific? Since most previous examples of CALI resulted in the loss of a cellular structure or disruption of a process, it was easy to dismiss them as resulting from non-specific photodamage or phototoxicity rather than specific protein inactivation. In the case of Capping protein and Mena, these proteins restrain or inhibit cellular processes and inactivation by CALI leads to positive changes in cellular properties. It is highly unlikely that non-specific photodamage could account for our observed positive cellular phenotypes. Because non-specific damage is such an important concern with this technique, extensive controls were performed that ensured that laser irradiation alone had no detectable effects in any of our quantitative phenotypic

assays. In the case of CP CALI, irradiation of EGFP-CP in cells without knockdown provided the best possible control for non-specific CALI effects as it is the same functional protein with identical subcellular localization as the protein that induced the loss of function. Together, these results strongly argue against non-specific effects due to phototoxicity and support the idea that EGFP-CALI can be used to specifically inactivate proteins with high spatial and temporal precision.

This study is the first demonstration that deficient cells complemented with tagged proteins are the ideal setting for a CALI experiment. We have identified a case with EGFP-CP where the presence of endogenous protein can completely mask CALI loss of function. While EGFP-CALI has been shown to work in cells that retain expression of the endogenous protein (eg. α-actinin[31]), this may reflect a special case where the EGFP-tagged protein oligomerizes with the endogenous protein.[105] In the CALI of EGFP-CP in KDR cells, we were able to use light fluxes that were 84% lower than the previously reported CALI of EGFP-α-actinin[31] (1.5 mW/μm^2 vs. 10.5 mW/μm^2, respectively) with identical irradiation times, thus showing that EGFP-CALI can be achieved with almost an order of magnitude less light delivery. The increased sensitivity of EGFP-CP to CALI is likely due to the fact that all of the CP is fused with EGFP, although other factors such as the intrinsic efficiency of protein inactivation due to the local protein environment of the EGFP tag may be involved.

In the case of CALI of CP we found differences between the RNAi knockdown phenotype and the CALI phenotype: while long-term depletion of CP generated a mass increase in filopodia, instantaneous inactivation of CP produced a large number of intrapodia-like protrusions. Both of these phenotypes are consistent with actin

polymerization.[99, 102] One explanation of this difference is that in the case of CP RNAi, the cell has days to upregulate pathways to deal with its lost ability to negatively regulate filament growth. For example, it has been recently shown that the actin bundling protein fascin is essential for filopodia formation[106] suggesting that fascin or other functional homologues may be upregulated or activated when CP is knocked down. The dorsal protrusions induced by the instantaneous activation of CP with EGFP-CALI may reflect true function of CP on the actin network with minimal additional regulation. In this regard, it is of interest that intrapodia in growth cones can be strongly induced by washout of cytochalasin D,[102] which depolymerizes actin filaments by capping them at their barbed ends.[107] Thus the washout of the drug would result in rapid "uncapping" of actin filaments, a similar event to acute loss of CP through CALI. It will be of interest to compare the complementary effects of CALI and RNAi on other actin binding proteins.

With the two examples presented in this study, the total number of proteins inactivated by EGFP-CALI now stands at five. Our results further validate the use of this technique and demonstrate that is a viable and efficient means of generating spatiotemporal protein inactivation. Our observation that endogenous, untagged protein can mask CALI effects is important for the design and interpretation of future CALI experiments. The knockdown/rescue lentiviral vector described in this work should greatly facilitate the application of CALI to other proteins. Since EGFP has many advantages for imaging and has been widely used to generate functional fusion proteins, EGFP-CALI using this approach will be a useful addition to the cell biologist's toolbox.

Methods

Generation of CP single-step knockdown/rescue vector. The human CPβ coding sequence was amplified by PCR from cDNA and cloned into the pMSCV vector downstream of EGFP. A 5'LTR-EGFP-CPβ PCR product was generated by splice-overlap extension PCR and cloned as a NotI/MfeI fragment into the pLenti-Lox 3.7 vector[108] to produce pLL5.0-EGFP-CPβ. The CPβ shRNA was generated using the target sequence GCACGCTGAATGAGATCTA [referred to as T2 in [99]] and was cloned into pLL5.0-EGFP- CPβ to produce pLL5.1-shCP-EGFP- CPβ.

Cell culture & generation of CP knockdown/rescue cells. Rat2 and MV^{D7}fibroblasts were cultured as previously described.[93] pLL5.1-shCP-EGFP-CPβ was used generate lentivirus by standard protocols.[108] Rat2 fibroblasts infected with this virus were cloned by fluorescence-activated cell-sorting and screened for CPβ expression by western blot. Antibodies against CPβ (mAb 3F2.3) and α-Tubulin (E7) used for western blotting were obtained from the Developmental Studies Hybridoma Bank at the University of Iowa; the CPβ antibody recognizes both the rat and human form of the protein.

CALI protocol. EGFP-CP CALI experiments were performed using a Spectra Physics 164 (Spectra Physics Laser Incorporated) argon ion laser (488nm line, 2W of beam power at the laser head) focused onto a 23.4μm diameter spot ($1/e^2$ diameter) through a 60X 1.45 NA PlanApo TIRF objective (Olympus). Irradiation was controlled with a fast Uniblitz (Vincent Associates) shutter. Laser power at the specimen plane dropped to 625mW due to optical losses and was measured by placing the sensor of a laser power

meter (Model FM with LS 10 head, Coherent Inc.) directly above the objective. Irradiation time was 100ms, resulting in a 62.5mJ dose of energy for the CALI experiment. Laser light was focused onto the specimen plane through a 488nm laser filter set (Z488/10, HQ525/50, Z488RDC, Chroma Technology Corporation), which had significantly higher light yield than the filter set described above used to visualize EGFP. EGFP-Mena CALI was performed essentially as above with the following modifications: laser light was focused on the specimen plane through a 100X PlanApo 1.3 Phase objective to produce a spot with a 5.0μm diameter. 525mW of power at the laser head resulted in 120mW irradiation power at the specimen plane after optical losses. Irradiation time was 300ms, resulting in a total energy dose of 36mJ for the CALI experiment.

Live-cell imaging. For live-cell experiments, Rat2 cells were plated onto 35mm glass-bottomed dishes (MatTek Corporation) coated with 10μg/mL fibronectin (Sigma). Twenty minutes after plating, media was changed to DMEM without phenol red supplemented with 10% FBS, L-glut, and pen/strep. MV^{D7} cells were plated onto glass bottomed dishes coated with 1μg/mL fibronectin and maintained in their normal culture medium. Imaging was performed on an Olympus IX81 inverted microscope equipped with a 100W mercury arc lamp, a cooled 12-bit digital CCD camera (Sensicam QE, Cooke Corporation), and a heated chamber (Werner Instruments) with CO_2 flow. All images were acquired with MetaMorph software (Version 6.0, Universal Imaging Corporation). Fluorescence imaging was conducted using the following filter sets: EGFP

(Z488/10, HQ525/50, Q495LP); Alexa568 (HQ535/50, HQ610/75, Q565LP) (Chroma Technology Corporation).

FRAP analysis. FRAP experiments were performed on an Olympus IX81 FV1000 laser scanning confocal microscope. A standardized 5.0μm diameter circular region was placed at the leading edge of cells. This region was photobleached with the 405nm line for 200ms at full power using the tornado scan mode while EGFP fluorescence was simultaneously monitored using the 488nm line at 1.0% power and a 2μs/pixel scan speed. Images were acquired and analyzed using Fluoview FV10-ASW software (Version 1.4a, Olympus Corporation) and exported into Microsoft Excel for further analysis. Curve fitting, percent recovery, and half recovery times ($t_{1/2}$) of photobleach corrected values were calculated as described[109] using a custom written MATLAB script.

Quantification of dorsal structures using Sobel edge detection. To objectively quantify the dorsal activity following EGFP-CALI of CP, DIC images were acquired every second with 2 × 2 binning. A MATLAB (Version 7.0, Natick, MA) script was written to automatically process the 12-bit grayscale DIC images. For each frame the image was read into memory and convolved with a Sobel edge detection filter. The filter is an approximation to the derivative and is consisted of two two-dimensional kernels (one horizontal and the other one vertical).[110] The sensitivity threshold value of the magnitude was set to 6×10^{-4}, below which edges are ignored. The convolution output, which was a binary image, was then masked by multiplying a binary image of the laser spot or annulus to segment the area of interest. The sum of the pixels values of the

masked edge image were obtained and normalized to the average of the pre-CALI values to create an index of dorsal activity before and after irradiation.

Visualization and analysis of F-actin and barbed ends after CALI. All labeling experiments were performed on the microscope stage. To visualize F-actin, cells were fixed with 4% paraformaldehyde for 10min , permeabilized with 0.1% Triton-X (in PBS) for 5min, and labeled with Alexa568 conjugated phalloidin (Molecular Probes) for 10min. Images were acquired by taking a 4.5μm Z-series with a 100nm step size and 2 × 2 binning. To remove out of focus fluorescence, background-subtracted image stacks were deconvolved using AutoDeblur (Version 9.2, AutoQuant Imaging Corporation) software (adaptive blind deconvolution, 80 total iterations).

To visualize barbed ends, cells were permeabilized with saponin buffer (20 mM HEPES, 138 mM KCl, 4 mM $MgCl_2$, 3 mM EGTA, 0.2mg/ml saponin, 1% BSA, 1 mM ATP, 3 μM phalloidin) for 1 min, washed once in saponin-free buffer, and labeled for 3 min at 37°C with 0.4 μM Alexa-568-G actin (Molecular Probes). Images were acquired by taking a 4.5μm Z-series with a 100nm step size and 2 × 2 binning. To quantify barbed ends, background subtracted z-series were condensed into a single image using a maximum pixel intensity projection (MetaMorph). A standardized circle with a 12μm diameter was placed in the center of the irradiated region and all other homologous, non-overlapping regions of the cell (1-8 per cell, depending on number of similar regions). Average pixel intensity was acquired in these regions and the value for the irradiated region was divided by the average value of the non-irradiated region(s). Images were prepared and analyzed using MetaMorph software.

Quantification of lamellipodial dynamics. Lamellipodial dynamics were quantified as described.[95, 111] Images were taken every 3s at 100X with 1 × 1 binning. Only cells producing new protrusions every three minutes or less were included in the analysis. Single lines were drawn in within the 5μm radius of where the cell was irradiated; kymographs were generated and analyzed with MetaMorph software and values were exported into Microsoft Excel for further analysis.

Statistical analysis. Single comparisons were made using unpaired student t-tests. Multiple comparisons from a single data set were analyzed using ANOVA. Data sets found to be significant were then further analyzed using Tukey's HSD post-hoc test

CHAPTER 3

A Biosensor for Endogenous Src-Family Kinase Activation Generated by Screening from a Library of Engineered Biosensor Scaffolds

Akash Gulyani[1,*], Eric A. Vitriol [2,*], Brian J. Dewar[2], & Klaus M. Hahn[1,3]

[1]Department of Pharmacology, [2]Department of Cell and Developmental Biology, and [3]Lineberger Comprehensive Cancer Center, University of North Carolina, Chapel Hill, North Carolina 27599, USA

Correspondence to: Klaus M. Hahn[1,3] Correspondence and requests for materials should be addressed to K.M.H. (Email: khahn@med.unc.edu).

[*]these authors contributed equally to this work

Abstract

Elucidation of complex signaling pathways requires precise spatio-temporal information on the activation of key signaling components in live cells and tissues. While most current methods for studying protein activity involve expressing the protein of interest with fluorescent tags, exogenously expressing and tagging a signaling protein can be perturbing. Biosensors that report the activity of unmodified, endogenous proteins in live cells have been rare. One of the major obstacles in generating sensors for native targets has been the absence of readily available binding reagents that are selective and activity-specific. To address this issue we present a novel approach which couples high throughput screening for artificial state-specific binding elements with a fluorescence-based reporting system that turns these elements into biosensors We have generated a biosensor for endogenous Src-family kinases with this method. Using this new sensor we observe the dynamic regulation of Src activity during cell motility and growth factor stimulation. This work offers a generally applicable approach to generate new tools to study endogenous protein activation in living cells.

Introduction

Studying unmodified, endogenous proteins in live cells relies on two components: a state-specific binder that will bind only to the active form of the target protein and a reporter system that will enable visualization of target recognition, thus providing a precise readout of timing and location of the activity of the target protein in cells. Earlier, we developed a biosensor for endogenous Cdc42 (a small GTPase of the Rho family) wherein a domain from Cdc42 effector protein that binds only to the active form of

Cdc42 was labeled with a dye that is sensitive to its environment and is designed to report protein interactions in live cells.[83-85, 112] However, such naturally occurring, specific binding domains are often not available, which is a limiting factor to the development of new sensors for endogenous targets. It is therefore desirable to generate artificial target selective, activity specific binding elements on a made-to-order basis. High throughput (HT) screening of a library of binding elements offers the means to achieve this goal. Furthermore, HT screening can be combined with our highly sensitive and bright fluorescent dyes to build a highly modular and generalizable biosensor scaffold that can readily be used to generate multiple sensors.

One such potential biosensor scaffold is the FN3 monobody (antibody mimic) derived from the tenth type III domain of human fibronectin domain III (FN3). FN3 monobodies are a small (~ 95 residues), thermally stable domains with an immunoglobulin-like fold composed of seven beta strands. They are easy to produce and manipulate. The beta strands are connected by flexible loops that contain the residues which confer the binding specificity of the monobody; the loops can be randomized while keeping the core domain structure intact. Libraries of 10^9-10^{11} variants have been generated[113] and can be easily screened via phage display. All of these features combine to make the FN3 domain an attractive candidate for a generalizable biosensor design (Figure 3.1a).

High throughput phage-displayed screening involving randomly varying a total of ten residues in two surface exposed loops has yielded FN3 monobodies that bind various SH3 domains, including SH3 domains from Src family kinases (SFKs).[113] One of the SH3 binders, 1F11 specifically binds to SH3 domains from SFKs and shows no

binding to SH3 domains from closely related proteins.[113] The current model of Src activation suggests that a specific Src SH3 binder can provide the basis for an activity-specific biosensor for Src. Structural studies have shown that Src kinase activation involves attenuation of possibly two intermolecular interactions and an opening up of the protein, followed by auto-phosphorylation of a tyrosine (Y416) in the activation loop of the kinase[114]. Therefore, a binder that binds to the SH3 domain of Src should have preferentially higher binding to the active form the kinase compared to the inactive form, with the expectation that the SH3 domain is likely more accessible in open, active form of Src .

Src family kinases (SFKs) are excellent biosensor targets due their roles as key regulators of a variety of signaling networks.[115, 116] SFKs regulate various processes like cell division, cell migration, survival and are important in major diseases like atherosclerosis and cancer.[115, 117, 118] They are activated downstream of numerous cell surface receptors and in turn regulate a variety of processes through phosphorylating a large pool of substrates.[119] With regards to actin-dependent processes and cell motility, there are numerous instances in which SFKs have been implicated. Src kinases control the formation of dorsal ruffles and macropinocytic vesicles in response to growth factors.[120] Src kinases are also involved in coordinating cell migration and protrusions in concert with Rho family GTPases[121, 122] by directly regulating the actin polymerization machinery through phosphorylation of actin binding substrates including Cortactin and the 'WAVE' complex,[123] gelsolin, and pCAS.[124] Additionally, Src activity is involved in adhesion turnover especially at regions proximal to the leading edge leading to lamellipodial extension.[125, 126] Since SFKs are key nodes in multiple pathways and have

multiple functions in cells, their activation must be tightly regulated in space and time. While Src substrate phosphorylation in cells has been reported,[127, 128] we wanted to examine the direct activation of endogenous SFKs especially in the context of actin reorganization and in cell migration. Using a novel, widely-applicable design strategy and an extremely sensitive biosensor we report the direct visualization of spatio-temporal activation of Src kinases in living cells.

Results and Discussion

We examined if 1F11 preferentially binds to the active form of Src kinases using pull-down assays with cell lysates from GN4 rat liver epithelial cells. GN4 cells show robust Src activation (over basal levels) when treated with the compound ciglitazone without changing total Src levels.[129] In this assay, hexahistidine-tagged 1F11 or the wild-type FN3 monobody (used as a non-binding control) was immobilized on Ni-NTA beads, incubated with cell lysates and examined for the ability to pull-down endogenous Src. As shown in Figure 3.1b, the 1F11 monobody pulls down substantially higher amount of Src from ciglitazone treated cells compared to untreated cells, indicating preferential binding to the activated form of the kinase. Wild-type FN3 domain or beads alone do not show any binding to Src in these assays. Pre-treatment of GN4 cells with the phosphatase inhibitor pervanadate dramatically attenuates 1F11 pulldown of Src (Figure 3.1b). In many cases, dephosphorylation of Tyrosine 529 is critical for Src achieve its “open” activated confirmation. This demonstrates that inhibiting Src from reaching activation prevents its interaction with the 1F11 monobody. It also shows that addition of 1F11 does not artificially activate Src.

Using substrate-based in-vitro kinase assays, we show that the SFKs pulled down by the biosensor are active. 1F11 beads that had been incubated with Ciglitazone-treated lysates, retained several fold higher kinase activity compared to wt-FN3 beads, control beads or even 1F11 beads that had been incubated with untreated lysates (Figure 3.1c). This observation once again supports that 1F11 is interacting with activated Src and that Src is a fully functional kinase when bound to 1F11.

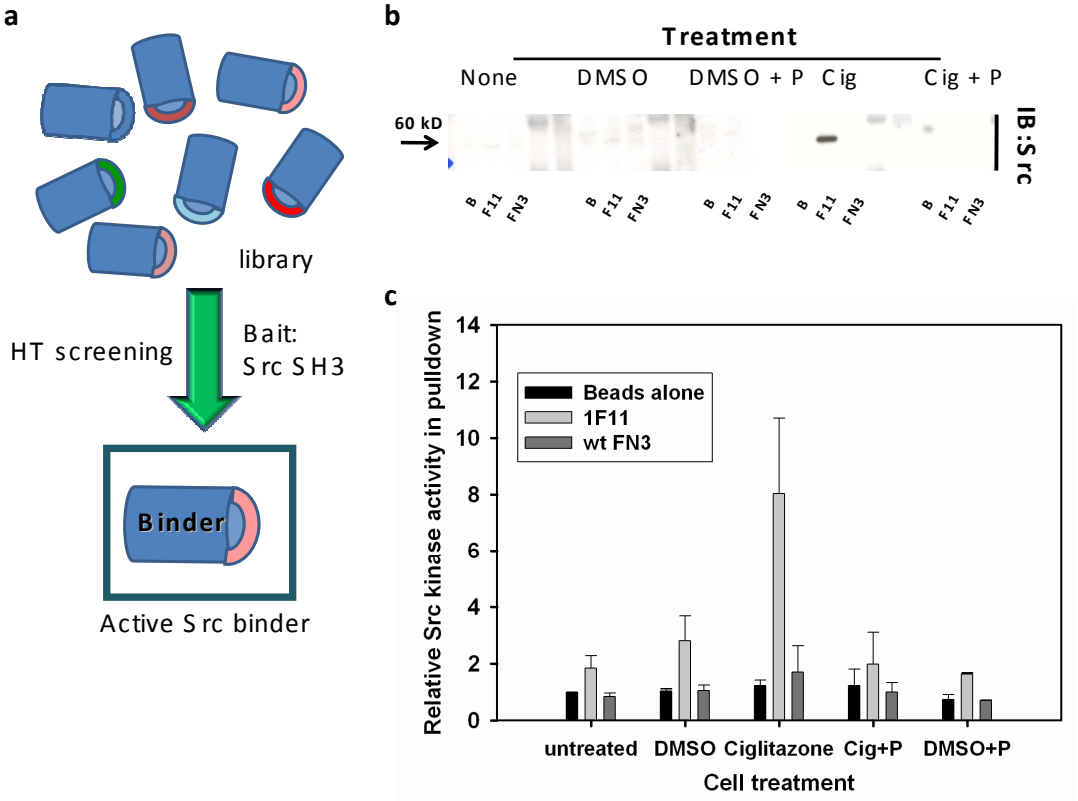

Figure 3.1: FN3 domain-based monobody 1F11 shows preferential binding to active Src. **a)** Schematic showing the generally applicable concept of using HT screening to identify a state-specific binder for active Src family kinases. In this case, Src SH3 domain was used as bait to find binders that binder SFK SH3 domains but show no binding to closely related SH3 domains. **b)** Immunoblot showing the amount of Src that binds to immobilized 1F11 or controls in a pulldown assay with GN4 cell lysates as a result of cell treatment. Cells were either untreated, treated with vehicle DMSO, Ciglitazone (Cig) or Ciglitazone with pervanadate pretreatment. As non-binding controls either beads alone (B) or immobilized wild-type FN3 domain (wt FN3) was used for the pulldown. **c)** Relative Src kinase activity in material bound to beads alone, immobilized WT FN3 or 1F11 after incubation with cell lysates from untreated or treated GN4 cells. Cells had been treated with DMSO, Ciglitazone or Ciglitazone after pervanadate pretreatment.

With 1F11 showing preferential binding to the active form of Src, the next step was to use this domain to construct a biosensor for Src that could be used in live cells. Our strategy involved covalently labeling 1F11 domain with an environmentally sensitive dye that would report binding of the sensor to its target. Environmentally sensitive, cysteine-reactive merocyanine dyes have been developed in our lab for the purpose of reporting protein interactions and are especially suited for live cell imaging owing to their brightness, long wavelengths and photostability.[112] As several of the dyes report target recognition through a change in fluorescence intensity, a second fluorophore was needed for ratiometric imaging. The emission from this second fluorophore would be insensitive to Src binding, therefore normalizing for changes in cell thickness, concentration of probe and uneven illumination.

Converting 1F11 into a biosensor involved optimizing three aspects of biosensor design to obtain a bright sensor with the necessary dynamic range: finding the right dye, determining the site for dye labeling and introducing a second fluorophore for ratio imaging without affecting target sensing. The details of the optimization will be discussed elsewhere but the key findings are summarized here. For introducing the second fluorophore, 1F11 was fused to the fluorescent protein, m-Cerulean.[130] In addition to providing a ratiometric fluorophore m-Cerulean fusion helped stabilize 1F11 and other FN3 variants in solution and in cells. A long flexible glycine-serine rich linker was used for the m-Cerulean fusion to 1F11 to minimize perturbation.[89] We found that short linkers adversely affected target binding.

1F11 contains no cysteine residues for dye-labeling, so we generated several different single-cysteine 1F11 fusion proteins. The positions selected for cysteine

replacements are shown in Figure 2. In order to reduce the possibility of off-target labeling, a surface exposed cysteine (residue 48) on m-Cerulean was also mutated. Several merocyanine dyes with varying side groups and donor-acceptor groups were examined for response and brightness. The response was evaluated by measuring the dye/m-Cerulean emission ratio changes due to purified target Src SH3 binding. Overall, Mero 53 (Figure 3.2a) emerged as the most suitable dye in terms of sensitivity and brightness. With several known solvatochromic dyes there is a tradeoff between dynamic range and brightness but Mero 53 was both sensitive and bright. This was consistent with previous studies of solvent-dependent fluorescence.[112] After testing different combinations of dyes and labeling positions, the version that showed the optimal results was 1F11 fusion labeled with Mero 53 at the residue 24 ($1F11_{A24C}$) (Figure 3.2b). Residue 24 is in the 'BC' loop of 1F11 close to the putative SH3 binding site.[113]

Figure 3.2c shows the ratiometric response (dye emission/mCerulean emission) of 1F11 biosensor measured with respect to increasing amounts of c-Src SH3. The biosensor exhibits a large (~50%) ratiometric increase (dye/FP). The increase in ratio is largely due to an increase in Mero 53 emission on target binding (Figure 3.2c); the mCerulean emission remains largely unaffected. The increase in Mero 53 emission is likely due to the dye experiencing a more hydrophobic environment when the sensor is SH3 bound. This is consistent with the dye emission being relatively quenched in polar, protic solvents in solvent studies.[112] We measured the apparent binding constant of the sensor towards its target SH3 from the fluorescence ratio changes (Figure 3.2d). A single-site binding analysis provides an apparent K_d of 0.69 μM. This is comparable to the binding constant obtained by isothermal titration calorimetry between unlabeled 1F11 and Src

SH3[113] indicating that labeling 1F11 and fusing it to mCerulean with the appropriate linker minimally perturbs binding to Src SH3. To examine if the fluorescence response we observe is due to target binding and not an artifact of the sensor design, we generated a control biosensor that is lacking a Proline residue on the 1F11 FG loop ($1F11_{P78A}$) that is required for target binding. The $1F11_{P78A}$ control biosensor showed no response to Src SH3 (Figure 3.2d) establishing that the sensor response is indeed due to target binding.

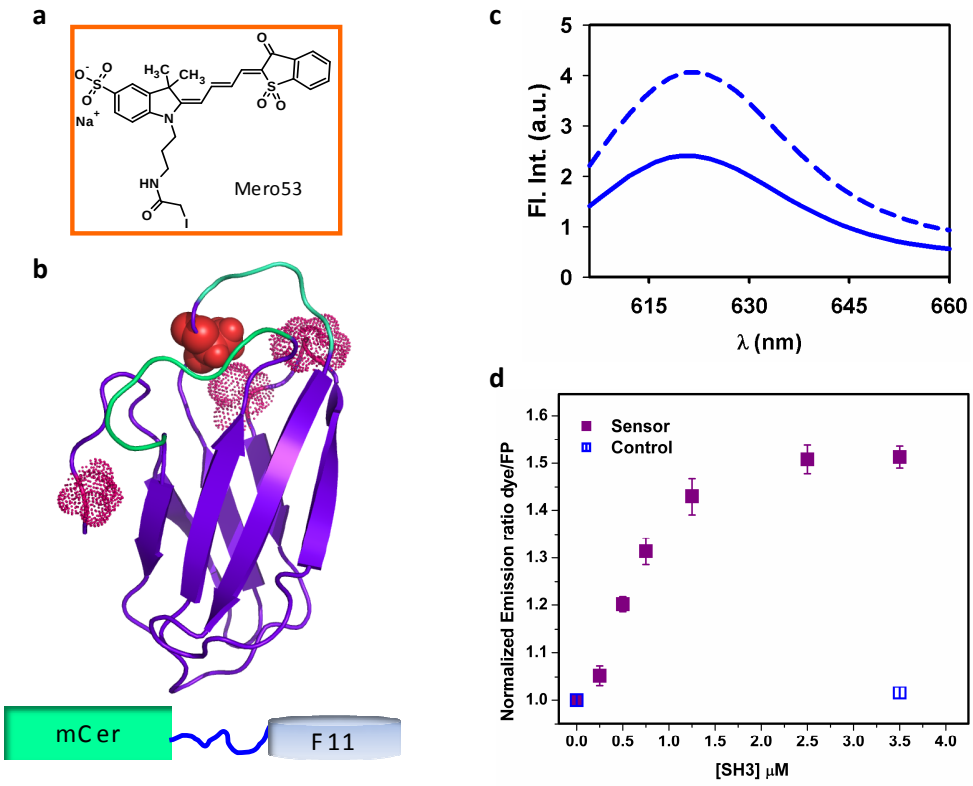

Figure 3.2. Design and *in vitro* validation of 1F11 Src biosensor. **a)** Structure of the environmentally sensitive merocyanine dye Mero53 **b)** Ribbon representation of 1F11 (based on FN3 domain structure) showing the residues used for single cysteine substitutions for covalent dye labeling. Alanine residue shown in bold was changed to cysteine in the final 1F11 sensor. Four residues highlighted with dots were also tested as part of the optimization process. Putative target binding loops are shown colored with cyan. Also shown schematically is the fusion of m-Cerulean to 1F11 via a flexible linker as part of sensor design. **c)** Mero53 emission change due to c-Src SH3 binding. Shown here is emission spectrum (λ_{ex} 590 nm) of 0.5 μM 1F11 biosensor alone (solid line) or with saturating amounts of purified c-Src SH3 domain (dotted line). **d)** Titration showing the change of normalized emission ratio Mero-53/m-Cerulean for 1F11 biosensor or control (0.5 μM) with increasing c-Src SH3. For dye, λ_{ex} 590nm and λ_{em} 620nm while for m-Cerulean λ_{ex} 433nm and λ_{ex} 477nm were used. Control sensor ($1F11_{P78A}$) has a critical Proline in the FG binding loop mutated to Alanine.

An important feature of the sensor is that the dye Mero 53 is extremely bright. The dyes are solvent sensitive so it is conceivable that they are not at high level of brightness when attached to the biosensors. Here, even in aqueous environments where dye emission is reduced, the dye emission was twofold greater than the emission from m-Cerulean. Further, the current sensor works through direct excitation of a high extinction coefficient, high quantum yield dye whereas FP FRET-based sensors rely on direct as well as indirect excitation of the functional fluorophores. This, in effect, makes the current dye-based sensor extremely sensitive in comparison with FRET sensors that have been extensively used in cell biology. Sensitivity and brightness of the sensor are extremely advantageous for live cell imaging since it is often imperative to minimize light exposure and the resultant photo-toxicity, in addition to the ability to visualize subtle signaling events.

We examined the ability of the biosensor to detect Src kinase activation in live cells. The sensor was microinjected into NIH 3T3 mouse embryonic fibroblasts (MEF) cells which were then stimulated with platelet derived growth factor (PDGF). PDGF stimulation of MEFs induces the formation of dorsal ruffles.[131, 132] It is known that Src activation is necessary for the formation of these large circular actin-based protrusions, and that active Src specifically localizes there.[120] Using the 1F11 biosensor, we see high dye/FP at dorsal ruffles from their induction until they submerge back into the cell body or close to become macropinosomes (Figure 3.3a); observation of active Src in these structures is consistent with previous findings using immunostaining in fixed cells.[120] In addition to validating that the biosensor reports local Src activity, this experiment is also critical in that it demonstrates that localized Src-dependent processes are not inhibited at

biosensor concentrations used for imaging. The brightness of the reporter dye in cells and the direct excitation of the fluorophores permit imaging at relatively low biosensor concentrations with minimum perturbation.

We examined Src at the cell periphery. It is also of note that there was no visible difference between the protrusive characteristics of cells injected with the biosensor, its control, or non injected cells, once again indicating that the presence of the sensor at imaging concentrations is not affecting cellular processes. This is important as Src activity and proper localization is required for cell migration and spreading. In MEFs, we saw high dye/FP ratios in lamellipodia in response to PDGF treatment. To further explore this we introduced the biosensor into PTK1 epithelial cells, which form very large, flat lamellipodia that constitutively undergo cycles of protrusion and retraction. In PTK1 cells, we discovered a concise band of high dye/FP ratio (~35% above local background) immediately adjacent to the protruding cell edge (Figure 3.3b,c). This band appears as soon as protrusions are initiated and disappears when the lamellipodia begins to retract. Interestingly, we also observed that the probe itself localized to cell edge protrusions, as detected with CFP fluorescence indicating significant enrichment of active Src at the cell edge (Figure 3.3d). As an imaging control, we used the $1F11_{P78A}$ variant of the biosensor and detected no change in dye/FP intensity at the cell edge (Figure 3.3c). Specificity of 1F11 to SFK SH3 domains has been extensively probed in original screening paper. We wanted to confirm specificity of the sensor in living cells by examining the effect of Src inhibitor PP2 on the sensor signal in cells. As shown in Figure 3.3d, both high dye/FP ratio and localization of the probe to the cell edge is immediately abolished subsequent to PP2 addition. Though Src is required for protrusions and migration[121, 133] and has many

known targets involved in actin reorganization,[123, 124] it has never been directly shown to be active in the lamellipodia. To our knowledge this is the first account of spatio-temporally localized Src activation in the lamellipodia and demonstrates that this activation occurs within 500nm of the cell edge and occurs in concert with protrusion initiation.

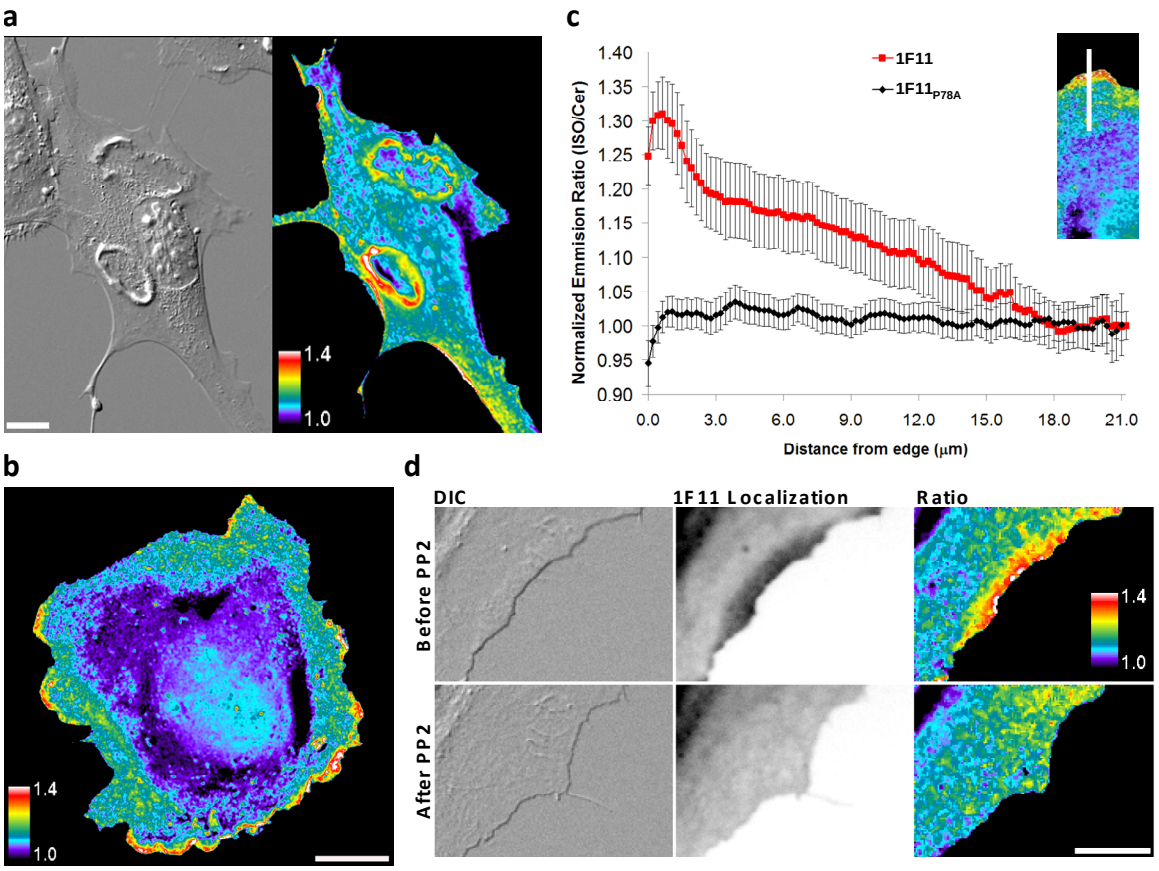

Figure 3.3. Spatiotemporal activation of endogenous SFKs in living cells. a) DIC (left panel) and Ratio (right panel) images of a PDGF-stimulated NIH 3T3 MEF microinjected with the 1F11 biosensor. Scale bar is 20μm. **b)** Ratio image of PTK1 cell microinjected with the 1F11 biosensor. Scale bar is 20μm. **c)** Linescan analysis of the leading edge of PTK1 cell lamellipodia microinjected with either the 1F11 biosensor or a non-binding control biosensor. 1F11: n = 10 cells, 166 linescans; $1F11_{P78A}$ monobody: n = 7 cells, 122 linescans. Error bars are 95% confidence intervals. Inset shows a representative ratio image of a PTK1 cell lamellipodia and line used for linescan analysis, solid white line is 20μm. **d)** DIC (left panels), ISO (1F11 Localization, middle panels), and Ratio (right panels) images from representative frames of a movie in which a PTK1 cell microinjected with the 1F11 biosensor was treated with the Src inhibitor PP2. Scale bar is 10μm.

The observation of a distinct band of endogenous Src activation close to the edge and the correlation of timing of Src activity with protrusion supports the notion that a dedicated pool of Src activity is involved in intricate control of cell protrusion machinery through actin cytoskeleton organization as well as adhesion signaling. The nodal role of Src is also highlighted by timing of Src activation in ruffles wherein we observe sustained bursts of Src activity coinciding with periods of actin organization. Src kinases perform multiple functions in cells and respond to different stimuli leading to the expectation that cells likely have distinct pools of Src activity. Our results clearly show this phenomenon with spatio-temporal resolution. The sensitive sensor offers a powerful tool to interrogate network dynamics controlling migration, adhesion and cytoskeletal dynamics.

In summary, we have demonstrated the efficacy of a generally applicable concept wherein HT screening can be used to generate biosensors for endogenous protein targets. Using this strategy, we developed a highly sensitive biosensor for endogenous Src family kinase activation in live cells. Furthermore, the sensor is modular in nature and this concept can now be extended to generate biosensors against multiple targets simply by changing the binding specificity of the FN3 domain. Finally, cell imaging using the sensor has provided novel insights into the activation dynamics of SFKs. Transient and localized Src activation was observed in dorsal ruffles and proximal to the leading edge in lamellipodial protrusions. Understanding the timing and location of SFK activation in these processes clarifies the critical role of SFK in regulating them.

Methods

Immunoprecipitation and pull-down assay. The antibodies for total c-Src, B-12 and N-16, were purchased from Santa Cruz Biotechnology. FN3 monobodies including the binder 1F11 and wt FN3 (non-binding control) were expressed in E.coli BL21 (DE3) as described previously[113]. The monobodies having a hexa-His tag were purified using Ni-affinity columns (His GraviTrap™) purchased from Amersham/GE healthcare as per manufacturers instructions, except in some cases a step gradient was used in the elution of the proteins from the His GraviTrap™ columns to increase purity.

The thiazolidinedione, ciglitazone, (±)-5-[4-(1-methylcyclohexylmethoxy)-benzyl] thiazolidine-2, 4-dione, is a PPAR ligand. Ciglitazone (Biomol) was prepared as stock solutions in dimethyl sulfoxide. GN4 cells grown as described above were left untreated before lysis, treated with DMSO, or treated with a solution of Ciglitazone in DMSO for either 10 or 30 minutes such that the final concentration of Ciglitazone was 50 μM. In order to inhibit phosphatases in a global manner, GN4 cells were pretreated with 50μM pervanadate for 5 minutes. For 'Cig+P', cells were pretreated with pervanadate, before the Ciglitazone treatment as described above. Prior to experiments, cells at 70–80% confluency were serum-starved overnight in Richter's minimum essential medium containing 0.1% fetal bovine serum. Following stimulation for the times indicated, media was aspirated, and the cells were rinsed twice with ice-cold PBS. The cells were then scraped into ice-cold RIPA buffer (150 mM NaCl, 9.1 mM Na_2HPO_4, 1.7 mM NaH_2PO4, 1% Nonidet P-40, 0.5% sodium deoxycholate, and 0.1% SDS, pH 7.4) with freshly added 200 μM Na_3VO_4, 250μM phenylmethylsulfonyl fluoride, 5 μg/ml leupeptin, and 10nm microcysteine. The cell lysates were clarified by centrifugation at 14,000 rpm for 10min

at 4 °C. Protein concentration of the supernatant was determined using the Coomassie protein assay reagent (Pierce).

For pull-down assays, 200 μg of lysates (in RIPA buffer, no SDS) from GN4 cells, treated as described above, were incubated with 100μg of either 1F11 or wt FN3 preabsorbed on 15 μL Ni sepharose (Qiagen) beads overnight with gentle agitation, in the presence of 20mM Imidazole. The beads were washed once with RIPA (no SDS), thrice with ice cold PB and then resuspended in 20μL Laemmeli buffer, boiled for 5 mintes, and subjected to SDS-PAGE, followed by analysis by western blots to look at total Src pulled-down by either the binder or control proteins. 10 μg of cell lysate was resuspended in SDS-PAGE sample buffer (0.5 M Tris, pH 6.8, 4% SDS, 20% glycerol, 10% β-mercaptoethanol, 0.1% bromphenol blue) and heated at 95°C for 5 min to denature proteins. The lysates were then resolved by SDS-PAGE on NuPAGE precast 10% Bis-Tris or NOVEX Tris-glycine gels (Invitrogen) and transferred to polyvinylidene fluoride (Immobilon-P; Millipore). The immunoblots were incubated with the appropriate primary antibody overnight at 4°C, washed three times with TBST, and probed with horseradish peroxidase-conjugated secondary antibodies for 1h at room temperature. Immunoblots were then developed with ECL (Amersham Biosciences) according to the manufacturer's instructions and visualized by autoradiography (Kodak X-Omat Blue film).

***In vitro* kinase assay.** Src kinase activity in Src protein pulled down by either the binder (1F11) or wt FN3 from stimulated or unstipulated GN4 cells was measured using a commercial Src assay kit (Upstate Biotechnology, Inc.) according to the manufacturer's instructions with slight modifications. Briefly, Src was subjected to FN3 pull-down as

described above from 200μg of cell lysate by overnight incubation with either the binder or control. Src activity present in FN3-bead complexes was assessed by measuring the transfer of the γ-phosphate of [γ-^{32}P]ATP to a specific Src substrate peptide for 10 min at 30°C. Phosphorylated substrate was then separated from residual [γ-^{32}P]ATP using P-81 phosphocellulose paper (Whatman) and quantified with a scintillation counter.

Purification and dye labeling of 1F11 monobodies. 1F11-mCerulean fusion proteins were expressed in E.coli BL21 (DE3) as described.[113] Briefly, 1L cultures were induced with 1mM IPTG at RT for 14-16 hours before harvesting the bacteria. The biosensor fusion proteins having hexa-His tag were purified using Ni-affinity columns (His GraviTrap™, GE healthcare) as per manufacturer's instructions, except in some cases a step gradient was used in the elution of the proteins from the His GraviTrap™ columns to increase purity. The proteins were examined for purity using SDS-PAGE.

Concentrated DMSO solutions of Cysteine reactive merocyanine dyes were added to 1F11-mCerulean fusion proteins present in 50 mM HEPES, 100 mM NaCl buffer pH 7.4 such that the dye was present in 5-10 fold molar excess and the DMSO in the reaction mixture was less than 10%. After reaction for 3-4 hours, excess dye was separated from labeled protein using size exclusion G-25 (GE Healthcare) columns. Labeled proteins were directly visualized after being subjected to SDS-PAGE electrophoresis and a single fluorescent band was observed. Also, no free dye was seen after size exclusion, where a clear separation was seen between the labeled protein band and the relatively immobile free dye. Coomassie labeling was also done to verify homogeneity of the sensor preparations. Labeling efficiency was calculated by measuring the dye and protein

concentrations of the labeled conjugate. Dye concentration was estimated using dye absorbance at 590 nm (ε = 140,000 cm^{-1} M^{-1}) while the protein concentration was estimated by using absorbance due to the mCerulean FP and its molar extinction coefficient of 43,000.[134] Labeling efficiency was in the range of 95-100 %. In order to minimize the likelihood of mCerulean getting labeled, Cysteine 48 was mutated to Alanine.

***In vitro* biosensor binding assays.** SH3 domain of from c-Src was expressed, purified and analyzed as described.[113] *In vitro* response of the labeled 1F11 or control monobody was tested by recording fluorescence spectra of samples where the biosensor has been incubated with increasing concentrations of Src SH3 domain in PBS pH 7.4 at room temperature, using SPEX fluorolog 3. Ratio-metric response was measured by recording dye fluorescence (λ_{Ex} = 590nm, λ_{EM} = 620nm) as well as the mCerulean fluorescence (λ_{Ex} = 433nm, λ_{EM} = 475 nm).

Cell Culture. GN4Rat liver epithelial cells were grown in Richter's minimal essential medium (Gibco) supplemented with 10% heat-inactivated fetal bovine serum and penicillin, streptomycin, and amphotericin B. NIH 3T3 fibroblasts (MEFs) and were cultured in 5% CO2 at 37°C in Dulbecco's modified Eagle's medium (DMEM, Mediatech) supplemented with 10 % fetal calf serum, 1 % L-Glutamine, and 1% penicillinstreptomycin. PTK1 cells (ATCC# CCL-35) were cultured in DMEM/F12 media (Gibco) supplemented with 8 % fetal calf serum, 1 % L-Glutamine, and 1% penicillinstreptomycin. MEFs and PTK1 cells were imaged in Ham's F-12K medium

without phenol red (SAFC Biosciences) with 2% fetal bovine serum, 15mM HEPES, 1 % L-Glutamine, and 1% penicillinstreptomycin. For imaging experiments MEFs and PTK1 cells were plated onto coverslips coated with 5μg/mL Fibronectin (Sigma) overnight. Culture media was exchanged for imaging media for one hour prior to microinjection. Cells were microinjected as described[83, 86] with a biosensor concentration of 40μM in the microinjection needle and were allowed to recover for 30-60min before imaging experiments began. MEFs were stimulated using 30ng/mL PDGF (Sigma). PTK1 cells were treated with 10μM PP2 (Sigma).

Microscopy. Imaging was performed on an Olympus IX81 motorized inverted microscope equipped with ZDC focus drift compensator, a cooled digital 12-bit CCD camera (CoolSnap, Roper Scientific), a 100W Mercury arc lamp, and MetaMorph imaging software. Images were acquired using a 40X UPlanFLN 1.3 NA oil immersion objective or a 60X 1.2 NA UApo N Silicon oil immersion objective. A Multi-pass dichroic mirror (89006bs, Chroma) was used with the following band pass filters: CFP (ET 436/20, ET 480/40) and ISO (HQ580/30, HQ 630/40). Images were acquired and processed as described.[83, 86] To generate activation profiles in protrusions, the linescan tool in MetaMorph was utilized.

CHAPTER 4

The Spatiotemporal Activation of RhoA during Growth Cone Advance and Collapse

Eric A. Vitriol[1], Youjun Chen[2], William D. Snider[2], & Klaus M. Hahn[3,4]

[1]Department of Cell and Developmental Biology, [2]Neuroscience Center, [3]Department of Pharmacology, and [4]Lineberger Comprehensive Cancer Center, University of North Carolina, Chapel Hill, North Carolina 27599, USA

Correspondence to: Klaus M. Hahn[3,4] Correspondence and requests for materials should be addressed to K.M.H. (Email: khahn@med.unc.edu).

Abstract

During development and regeneration, a growth cone guides the extending axon of a neuron through an environment of positive and negative cues until in reaches its specific destination. A principal target of these cues is the cytoskeleton and the molecules which regulate it. A large body of research has implicated that repulsive cues and collapse factors mediate their effects through the small GTPase RhoA. However, little is known about the subcellular regulation of RhoA during normal axon extension and how that changes in the presence of a repulsive agent. Here we utilize a genetically encoded biosensor to determine the spatiotemporal activation of RhoA during growth cone advance and collapse. We find that RhoA is active in the peripheral domain of migrating growth cones, and that this activation is persistently maintained during axon advance. We also show that although RhoA levels increase in the growth cone following the addition of a soluble collapse factor, they rapidly decrease after the growth cone initiates the collapse process while the cell body RhoA levels remain elevated. With novel spatiotemporal information, our results provide new mechanistic insight into the role of RhoA in growth cone behavior.

Introduction

There are two prominent instances in which neurons extend axons. The first is during embryonic development, when the primary goal of axon growth is to find the appropriate dendrite of another neuron to form a synapse. The second is during peripheral nerve response to injury. In mammals, the neurons from the central nervous system lack the ability to undergo regenerative growth, thus nerve wounding generates permanent

effects. In both cases, locally secreted factors stimulate an axon to extend and then guide it via its growth cone to its appropriate destination.[135, 136] A principal intracellular target of these external factors (these include neurotrophins, netrins, ephrins, and semaphorins) is the cytoskeleton and the molecules that regulate it, including the Rho-family of small GTPases.

Rho-family GTPases are centrally important regulators of the cytoskeleton. They hydrolyze GTP in order to switch between active (GTP-bound) and inactive (GDP-bound) states. Their activity is negatively regulated by GTPase activating proteins (GAPs) and GDP disassociation inhibitors (GDIs) and positively regulated by guanine nucleotide exchange factors (GEFs). Thus, Rho-family GTPases act as "molecular switches" that can be turned on or off with profound downstream effects.[137, 138] Of the Rho-GTPases, RhoA is one of the best characterized members. It controls a number of behaviors relevant to axon growth, including actin and microtubule dynamics, and actomyosin contractility.[137]

The current paradigm is that RhoA is a potent inhibitor of axon growth. In CNS injury, locally secreted factors in the wounded region activate RhoA, causing growth cone collapse and regeneration failure.[139]Axon retraction is predominantly mediated through RhoA stimulation of actomyosin contractility.[140] In experimental spinal chord injury models, inhibition of RhoA signaling has led to axon regrowth and partial recovery;[98, 140] currently the RhoA inhibitor BA-210 is in phase I/IIA trials for treatment of spinal chord injury.[141]

However, RhoA-mediated growth cone collapse is also a necessary component of guidance and therefore of appropriate forward movement;[104, 142, 143] the growing axon

must be able to dynamically switch between states of extension and retraction to respond appropriately to positive and negative guidance cues. Furthermore, there have been studies that have shown RhoA is a positive mediator of growth cone advance in a manner separate from its role in growth cone collapse.[144-147] These results are counterintuitive to the conventional model of RhoA has a growth inhibitor and lead to an important outstanding question in the field: how can RhoA both negatively and positively regulate axon growth?

During axon growth, microtubule dynamics are necessary for motility and guidance.[148-150] In the growth cone, the microtubule cytoskeleton is highly spatially organized. The majority of microtubules are localized to the central domain, which is immediately adjacent to the axon shaft. These microtubules are stable and relatively non-dynamic. A small subset of these microtubules invades the transition and peripheral domains; these are extremely dynamic, rapidly undergoing cycles of growth and shrinkage.[103] In growth cones, RhoA is responsible for corralling the microtubules into the central domain and for dampening their dynamic behavior.[151]

RhoA has the ability to organize and stabilize microtubules through both direct downstream signaling and through indirect effects resulting from actin-microtubule coupling. The former occurs through the RhoA effector mDia, which can interact with the microtubule tip-binding proteins EB1 and APC.[152, 153] The latter results from RhoA regulation of actin and actomyosin contractility; these effects generate actin structures which can shape and dynamically regulate the microtubule cytoskeleton through physical linkage.[103, 151] Furthermore, in addition to microtubules being downstream of RhoA, it has also been shown that they can act upstream of RhoA activation.[144, 154-156] What is

unclear in the growth cone is how the relationship between RhoA and microtubules is spatially defined, and how this relationship relates to growth cone motility.

The Hahn lab has engineered a genetically encoded Fluorescence Resonance Energy Transfer (FRET) biosensor to directly visualize the activation of RhoA in living cells.[89] The biosensor is a single-chain design consisting of full-length RhoA that is labeled at its N-terminus with YFP, followed by a flexible linker, CFP, and then the Rho-binding domain (RBD) of Rhotekin. In the inactive GDP-loaded state RhoA does not bind RBD, and there is little FRET between the adjacent fluorescent proteins. In the active GTP-bound state RhoA interacts with RBD and FRET is increased (Figure 1). By leaving the C-terminus of RhoA intact, this biosensor undergoes proper localization and responds correctly to GDI and to positive and negative regulation by GEFs and GAPs.[89]

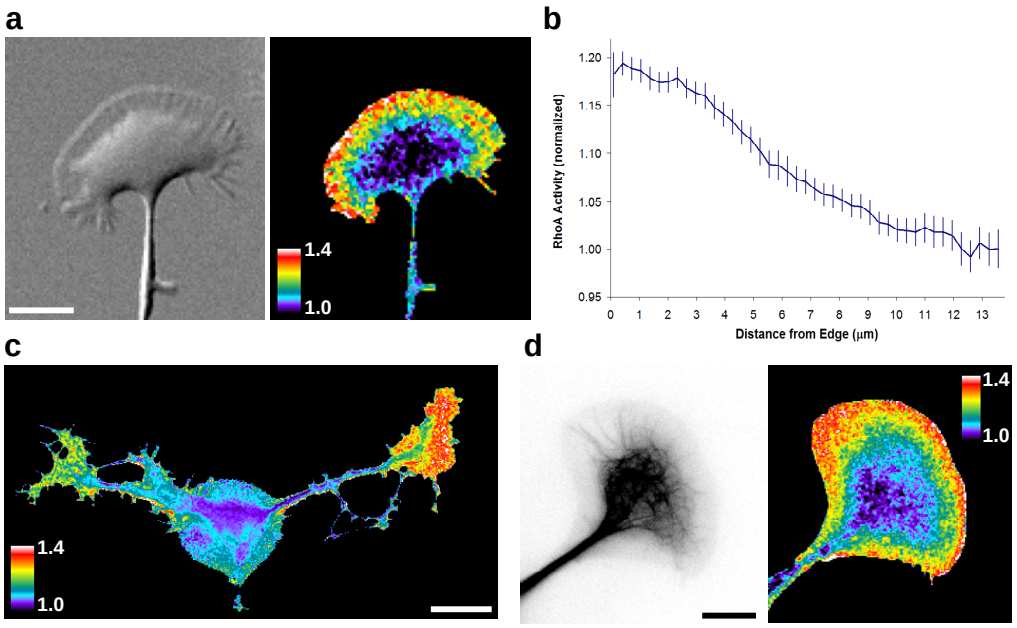

Figure 4.1. Localization of RhoA activation in growth cones. a,d Differentiated CAD cells and **c,** primary DRG neuron expressing the RhoA biosensor. **a,** DIC (left panel) and ratio (right panel) images of a CAD cell growth cone, scale bar is 10μm. **b,** RhoA activation profile in CAD cell growth cones (n = 70 linescans, 7 growth cones), error bars are 95% confidence intervals. **c,** ratio image of a DRG neuron, scale bar is 10μm. **d,** Microtubule (left panel, labeled with mCherry-β-Tubulin) and ratio images of a CAD cell growth cone, scale bar is 10μm.

Results and Discussion

We introduced the RhoA biosensor into CAD neuroblastoma cells. These cells can be induced to differentiate by serum withdrawal;[157] in early differentiation they extend axons with motile growth cone-like structures that phenotypically mimic growth cones found in primary neurons. In CAD cell growth cones we observe a band of high RhoA activation immediately adjacent to the leading edge that gradually tapers to the growth cone center where FRET/CFP ratio values are lowest (Figure 4.1a, b). Only 5% total change in the FRET/CFP ratio from the growth cone center to the edge was seen in CAD cells expressing a control biosensor lacking the Rho binding domain (RBD) (Figure 4.2a) with no peak near the periphery. Additionally, since RhoA is active at the plasma membrane there was a concern that the loss of activity in the growth cone center was a volume artifact caused by increased cell thickness in this region. To address this, we performed FRET imaging using Total Internal Reflection Fluorescence Microscopy (TIR-FM) to obtain a volume independent measurement and once again found the lowest FRET/CFP values in the center of the growth cone and the highest in the peripheral domain (Figure 4.2b). This broad gradient of RhoA activity at the growth cone periphery was also observed in mouse E14.5 DRG neurons (Figure 4.1c). The activation pattern observed in growth cones is different than what has been reported in the protruding lamellipodia of fibroblasts where all of the activity is contained in the first 2μm relative to the leading edge.[89] The axon stalk and cell bodies of DRG neurons contained the lowest FRET/CFP ratio values (Figure 4.1c). We then co-expressed mCherry-β-Tubulin in CAD cells to provide a cytoskeletal reference for growth cone morphology. The microtubule cytoskeleton in CAD cell growth cones was organized in a manner

consistent with previous studies of primary neurons: the microtubules are largely confined in the central domain with a few individual microtubules extending out into periphery (Figure 4.1d). In reference to this marker we see that RhoA activation is absent in the growth cone center where microtubules are abundant and increases immediately outside of this region (Figure 4.1d), hinting at a functional relationship between RhoA and microtubules.

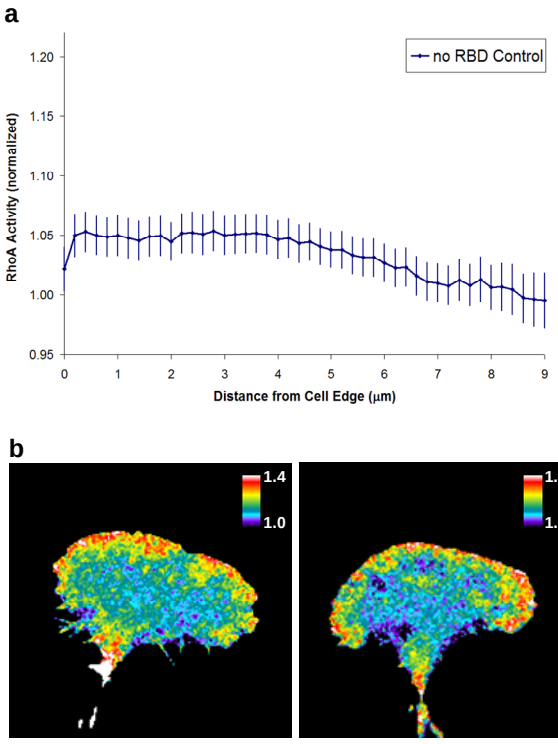

Figure 4.2. Controls for localization of RhoA activity. a, Activation profile of control RhoA biosensor that lacks the RBD binding domain (n = 269 linescans, 26 growth cones), error bars are 95% C.I. **b,** TIRF ratio images of CAD cell growth cones

We also performed time-lapse imaging of growth cones co-expressing mCherry-β-Tubulin. We observe that when bundles of microtubules are formed in the growth cone periphery in association with intrapodia there is a decrease in local RhoA activity levels, even in regions adjacent to the leading edge where FRET/CFP ratios are highest (Figure 4.3a). Combined with the observation that RhoA activity is lowest in the central domain where polymerized microtubules are most prevalent (Figure 4.1d) we hypothesized

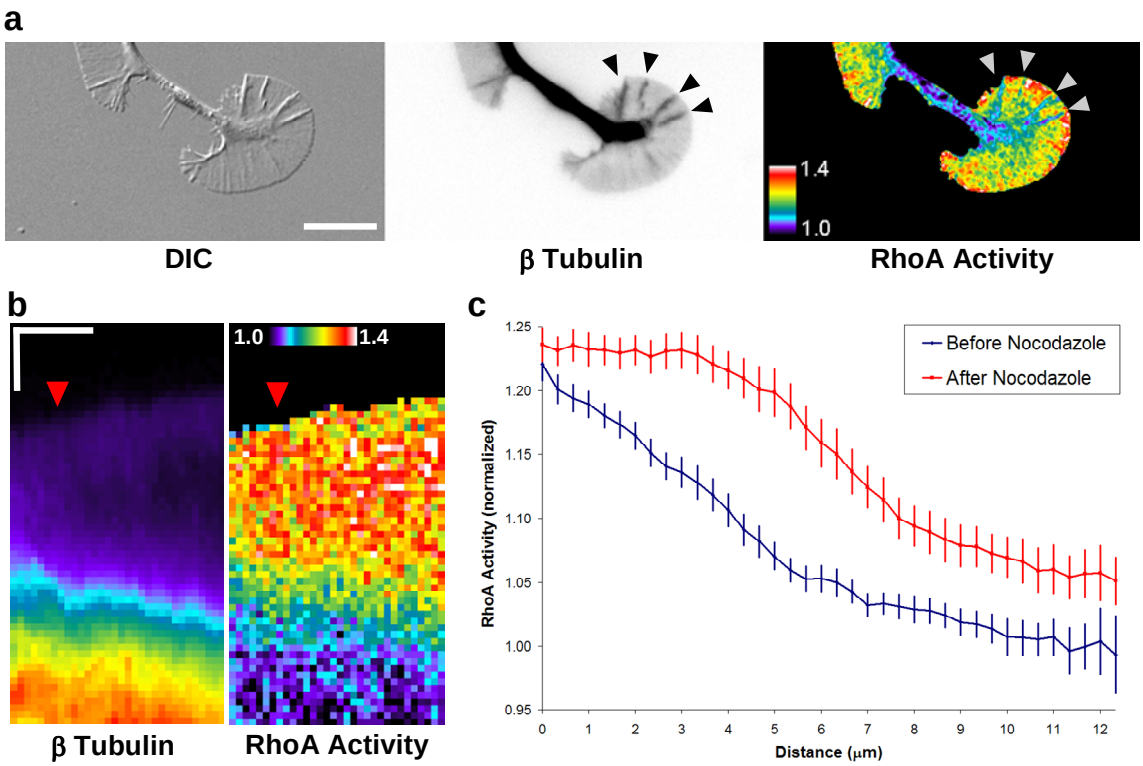

Figure 4.3. RhoA activation and microtubule polymerization are inversely related in the growth cone. a, DIC (left panel), microtubule (center panel) and ratio (right panel) images of a CAD cell growth cone, scale bar is 10μm. Arrows indicate regions of enriched microtubules (black arrows, center panel), which correspond to areas of low RhoA activity (white arrows, right panel). **b,** Kymographs of microtubule (left panel, psuedocolored) and ratio images from a CAD cell growth cone treated with nocodazole, vertical scale bar is 3μm, horizontal scale bar is 2min. Red arrow indicates nocodazole addition. **c,** RhoA activation profile in CAD cell growth cones before (blue line) and after (red line) nocodazole treatment (n = 70 linescans from 7 cells, the same cells were used for before and after measurements).

that microtubules inhibit RhoA in the growth cone and serve as guides for its pattern of activation. To directly test this hypothesis we depolymerized microtubules with nocodazole. Following addition of 300nM nocodazole, microtubules that extended past the central domain immediately began to retreat away from the growth cone edge (Figure 4.3b). Simultaneously, the zone of high RhoA activity expanded, invading into the central domain where FRET/CFP ratio values were initially low (Figure 4.3b). Linescan analysis performed on the same growth cones before and after nocodazole treatment (n= 7)

reveals that the pre-nocodazole peak of RhoA activity extends an additional 3-4μm into the central domain before it begins to taper down to lower levels (Figure 4.3c). These experiments prove the causal relationship between microtubules and RhoA. Previous work has shown that RhoA serves as an upstream regulator of microtubules in the growth cone, corralling them into the central domain through generation of actin arcs and actomyosin contractility.[151] Our results demonstrate that microtubules are also upstream regulators of RhoA. Together, this suggests that there is a feedback loop between the two components that maintains both the organization of microtubules and the localization of active RhoA in the growth cone during axon extension.

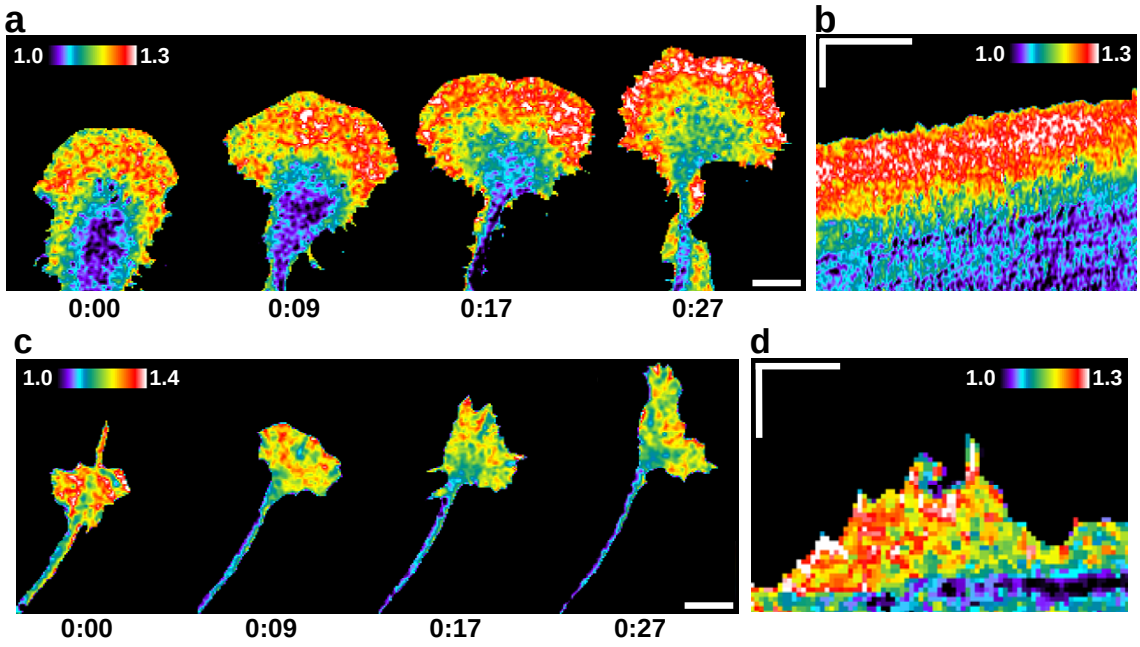

Figure 4.4. RhoA activation in advancing growth cones. a,b, Differentiated CAD cell and **c,d,** primary DRG neuron expressing the RhoA biosensor during growth cone migration. **a,** nascent CAD cell growth cone undergoing constitutive forward movement, scale bar is 10mm. **b,** Kymograph of growth cone in **a**, vertical scale bar is 10μm, horizontal scale bar is 10min. **c,** advancing DRG neuron, scale bar is 10μm. **d,** Kymograph of a DRG growth cone protrusion, vertical scale bar is 5μm, horizontal scale bar is 3min.

Time-lapse imaging of motile growth cones revealed that this pattern of RhoA activity is maintained during axon advance, even in growth cones undergoing long periods of constitutive forward movement (Figure 4.4a, b). DRG neurons also exhibited RhoA activation during migration (Figure 4.4c). Kymograph analysis of a DRG growth cone protrusion shows that RhoA is present at protrusion initiation and remains active for its entire duration (Figure 4.4d). These examples provide direct evidence that some RhoA activation is associated with positive growth cone motility and edge protrusion and not solely a mediator of retraction, collapse, and inhibition of movement.

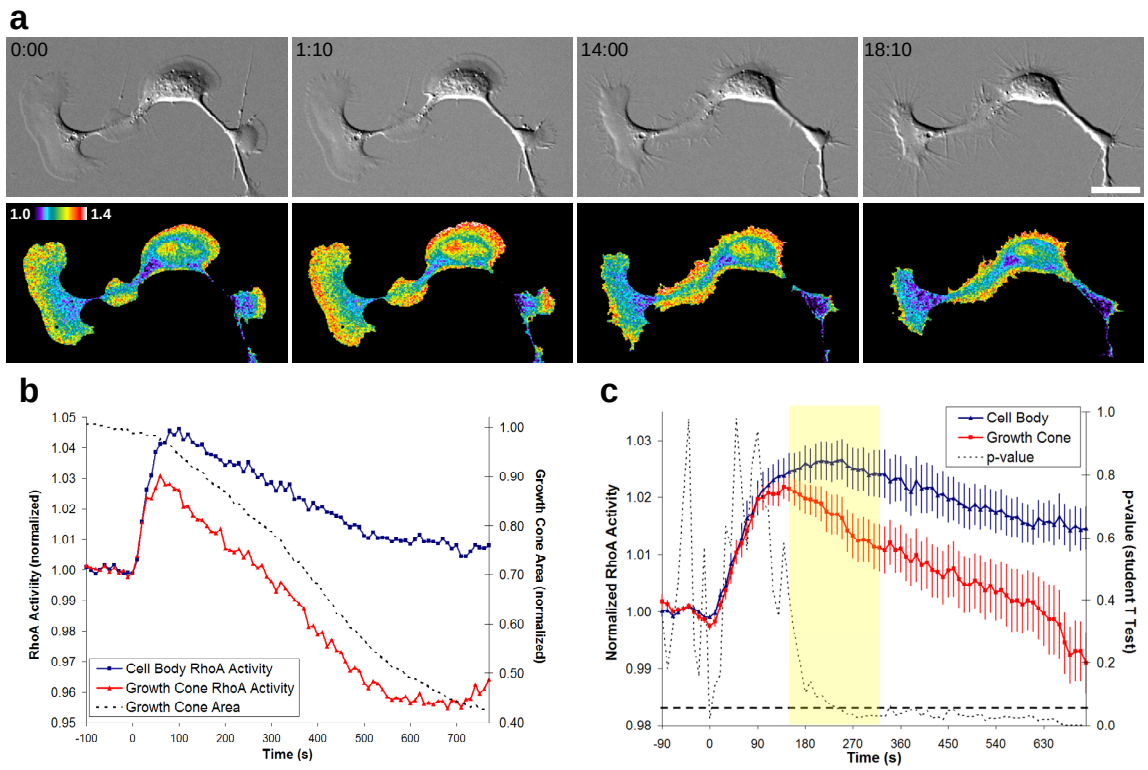

Figure 4.5. RhoA activation during growth cone collapse. a, DIC (top panels) and ratio (bottom panels) images of a differentiated CAD cell treated with LPA, scale bar is 10μm. LPA was added at time point 0:00. **b,** Graph of growth cone and cell body RhoA activity from the cell in **a**, growth cone collapse is indicated as a loss in growth cone area (dashed line). **c,** Graph showing average RhoA activity in all growth cones (red line) and cell bodies (blue line) (n = 31 growth cones, 24 cell bodies). Yellow bar indicates the average time to loss of 5% of initial growth cone area ± 95% confidence intervals (246.1s ± 86.2s). Error bars are s.e.m, dotted line indicates p-value of student's t-test between growth cone and cell body values, horizontal dashed line shows p = 0.05.

Numerous studies have shown that soluble factors that cause the growth cone to collapse mediate their effects through RhoA and its downstream upregulation of actomyosin contractility.[139] However, there is little known about how RhoA behaves at the subcellular level during this process. We utilized differentiated CAD cells to investigate the spatiotemporal regulation of RhoA during Lysophosphatidic acid (LPA)-mediated growth cone collapse. Following addition of 3μM LPA, we see an instantaneous and significant response of the biosensor in both growth cones and cell bodies (Figure 4.5a-c). No changes in RhoA activity were observed in control experiments using cells expressing a mutant biosensor (T19N) stimulated with LPA or cells expressing the wild-type biosensor stimulated with a bovine serum albumin (BSA) loading control (Figure 4.6). In growth cones, peak RhoA activation occurred earlier than cell bodies (Figure 4.5b, c), and on average preceded the initiation of growth cone collapse (Figure 4.5c). Following peak RhoA activity, the growth cone FRET/CFP ratio values degraded coincident with collapse while cell body RhoA was maintained at an elevated level (Figure 4.5b, c; see Figure 4.7a-c for a summary of all LPA experiments). At the latter stages of collapse, growth cone concentrations of active RhoA had fallen significantly below pre-LPA levels (Figure 4.7d). These results provide a new spatiotemporal insight into RhoA-mediated growth cone collapse and make two new suggestions as to the mechanism of which it occurs: that sustained elevation of RhoA activity in the cell body may play more of a role in collapse and retraction than once thought and that elevated RhoA levels in the growth cone are required to initiate but not sustain or complete collapse.

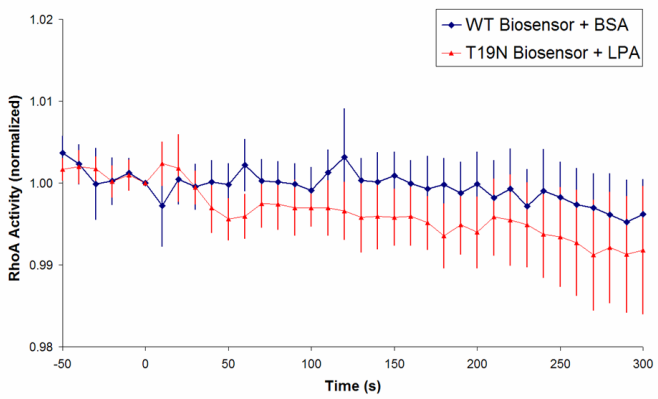

Figure 4.6. Controls for RhoA activity change following LPA stimulation. Graph shows average RhoA activity in cells expressing the wild-type (WT) biosensor treated with BSA (n = 9) and cells expressing the control biosensor containing the T19N dominant negative mutation treated with LPA (n = 11).

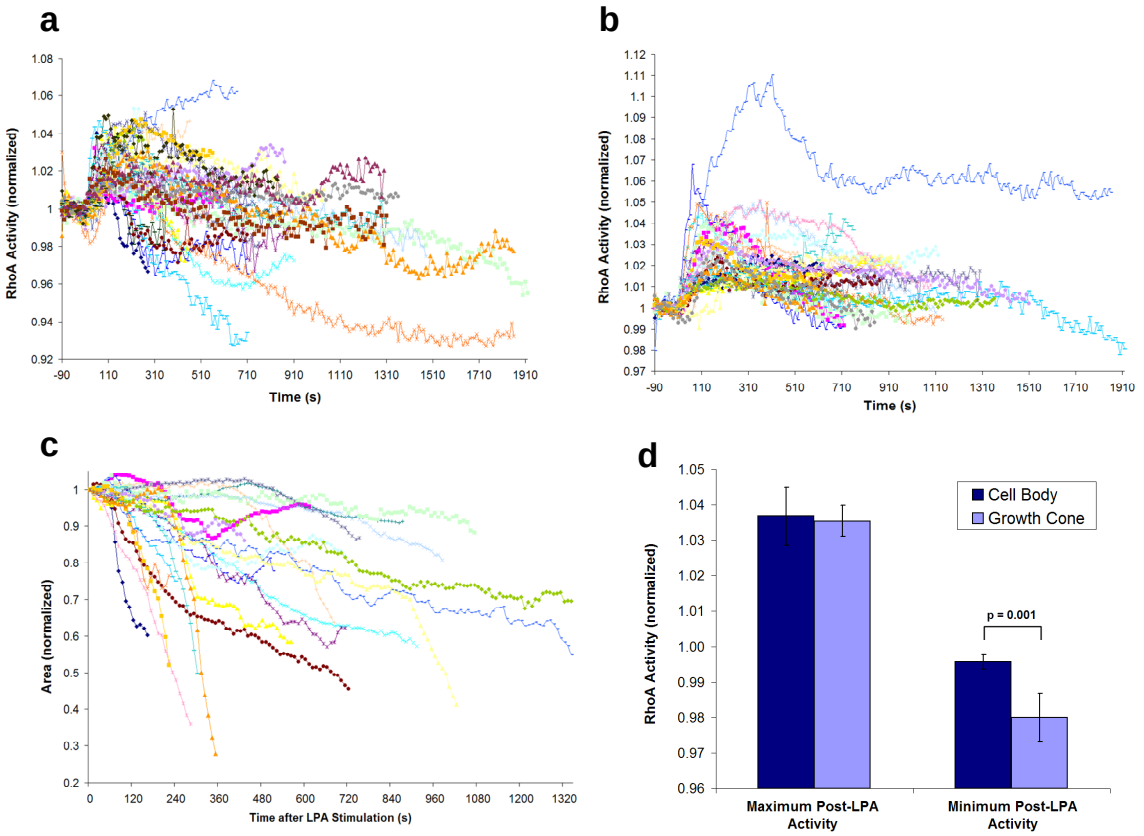

Figure 4.7. Summary of all LPA-induced collapse experiments. a, RhoA activation in all growth cones (n = 31) included in measurement. **b,** RhoA activation in all Cell Bodies (n = 24) included in measurement. **c,** Growth cone area loss (n = 23) for all growth cones included in measurement (includes all growth cones that lost > 5% of initial area). **d,** Graph showing maximum and minimum post-LPA average RhoA values in growth cones and cell bodies (n = 31 growth cones, 24 cell bodies). Error bars are 95% confidence intervals; p-value was derived from a student's t-test.

Methods

Cell Culture. CAD cells were cultured in DMEM/F12 medium (Gibco) supplemented with 8 % fetal calf serum, 1 % L-Glutamine, and 1% penicillinstreptomycin. They were imaged in Ham's F-12K medium without phenol red (SAFC Biosciences) supplemented with 15mM HEPES, 1 % L-Glutamine, and 1% penicillinstreptomycin. To induce differentiation, CAD cells were plated on coverslips coated with 18μg/mL Laminin (Sigma). After 90min, normal culture medium was exchanged for imaging medium. Cells were allowed to differentiate for an additional 90-120min prior to imaging. CAD cells were transfected 12-24hrs prior to imaging with the appropriate constructs using Fugene 6 (Roche) according to manufacturer's instructions. For LPA stimulation experiments, CAD cells were treated with 3μM LPA (Sigma). For nocodazole experiments, CAD cells were treated with 300nM nocodazole (CalBiochem). DRG neurons were cultured and transfected as previously described.[150] Imaging was performed approximately 12hrs after NGF-induced differentiation in Ham's F-12K medium without phenol red (SAFC Biosciences) supplemented with 5% fetal calf serum, 15mM HEPES, 1 % L-Glutamine, and 1% penicillinstreptomycin.

Microscopy. Imaging was performed on an Olympus IX81 motorized inverted microscope equipped with ZDC focus drift compensator and TIRFM illuminator, a cooled digital 12-bit CCD camera (CoolSnap, Roper Scientific), a 100W Mercury arc lamp, and MetaMorph imaging software. Images were acquired using a 40X UPlanFLN 1.3 NA, 60X 1.45 NA PlanApoN TIRFM objective, or a 60X UPlanFLN 1.4 NA oil immersion objective. A Multi-pass dichroic mirror (89006bs, Chroma) was used with the

following band pass filters: CFP (ET 436/20, ET 480/40); FRET (ET 436/20, ET 540/30); and mCherry (HQ580/30, HQ 630/40). Coverslips were mounted in an Attofluor live cell chamber (Invitrogen) placed in a microscope stage with a heated stage adaptor (Warner).

Image analysis. FRET/CFP ratio images were calculated after shading correction, background subtraction, and binary masking using MetaMorph and MatLab software as previously described. To generate activation profiles, the linescan tool in MetaMorph was utilized. Linescan analysis was performed as described. In brief, lines were drawn perpendicular from the cell edge to the center of the growth cone, then averaged and normalized to the values at the growth cone center (center was defined by the last 5 pixels of the average of all lines containing at least 30% of all input pixels). To account for growth cone diversity subsequent to nocodazole treatment, linescans were aligned by making the starting value the pre-LPA peak rather than the cell edge. To measure RhoA activation during LPA stimulation, a polygon was drawn around the region of interest in the photobleach-corrected masked ratio image that best included that region for the duration of the movies. All pixel values greater than zero were included in the measurement. RhoA activation was normalized to the average of the first 10 time points prior to LPA addition. Growth cones and cell bodies were photobleach corrected separately due to small differences in their rates of bleaching.

CHAPTER 5

Automated Identification and Tracking of Focal Adhesions Reveals Phosphorylation of Paxillin at Serine 178 A Key Regulatory Mechanism of Adhesion Dynamics

Mathew Berginski[1,*], Eric A. Vitriol[2,*], Klaus M. Hahn[3,4], & Shawn M. Gomez[1]

[1]Department of Biomedical Engineering, [2]Department of Cell and Developmental Biology, [3]Department of Pharmacology, and [4]Lineberger Comprehensive Cancer Center, University of North Carolina, Chapel Hill, North Carolina 27599, USA

Correspondence to: Klaus M. Hahn[3,4] and Shawn M. Gomez.[1] Correspondence and requests for materials should be addressed to K.M.H. (Email: khahn@med.unc.edu) or S.M.G. (Email: smgomez@unc.edu).

[*]these authors contributed equally to this work

Abstract

Focal adhesions are macromolecular complexes that provide a linkage from a cell to its external environment. In a motile cell they form, enlarge, and disassemble; these processes are essential to and govern cell migration. To better understand the dynamic regulation of focal adhesions during cell motility we have developed software for the automated detection, tracking, and data extraction of these structures using Total Internal Reflection Fluorescence Microscopy (TIR-FM) image sets of fluorescently tagged adhesion components. Utilizing this software we can generate high-content data sets that include the size, shape, intensity, and position of every adhesion present in a living cell. Moreover these properties are followed over time to assess adhesion lifetime and turnover rates. Here we apply this analysis to the adhesion component Paxillin in migrating NIH 3T3 fibroblasts. We also show how a single point mutation in Paxillin at the Jun-kinase phosphorylation site Serine 178 changes focal adhesion size, distribution, and rate of assembly. We present this freely available software as a generally applicable tool that will advance the understanding of how focal adhesions are dynamically regulated in living cells

Introduction

Focal adhesions (FAs) are sophisticated protein complexes that serve as points of integration for both mechanical and chemical signaling, playing a central role in cellular adhesion, survival, and motility. They form and disassemble as a mechanism to transduce signals. Characterizing how these structures dynamically change is essential for understanding processes such as cell migration, which requires that the adhesions are

continuously remodeled as the cell moves forward. During motility, new adhesions are born at the leading edge of a protruding lamellipodia. These FAs enlarge and then are either disassembled at the base of the protrusion in a process known as adhesion turnover[158] or become longer-lived structures that are eventually dismantled in the retracting tail at the rear of the cell. In this and other FA-relevant processes, FA dynamics are highly regulated by structural and signaling molecules.[158-160] Alterations in the balance of these regulating factors plays a key role in adhesion turnover and thus normal cell function.

Microscopic imaging of FAs has driven a significant portion of our current understanding of adhesion dynamics, with methods such as total internal reflection fluorescence microscopy (TIR-FM) providing high-resolution images capable of being quantitatively analyzed. However, challenges in image capture and downstream analysis has generally led to the characterization of only a relatively small number of hand-picked adhesions within any given cell[158]. Recent technical and methodological improvements have led to the automated detection and characterization of focal adhesions for application in high-throughput screening studies. For instance, Paran and colleagues[161] have reported on the use of a high-throughput high-resolution imaging system to screen a plant extract library for effects on adhesion morphology and distribution. The same high-throughput imaging system was used to perform multicolor analysis on various adhesion components[162] and used in a siRNA screen against adhesion related genes.[163] In these instances, researchers were able to obtain molecular signatures of protein components within focal adhesions, resolve sub-domains within adhesions, and identify clusters of genes that had similar effects on focal adhesion morphology and placement. These

studies demonstrate the power of being able to identify and characterize all adhesions present within a cell. However, as these approaches rely on cell fixation, critical aspects of focal adhesion biology, including spatiotemporal adhesion dynamics, are lost.

Here we describe a novel system for the quantification of focal adhesion spatiotemporal dynamics. This approach utilizes high-resolution (60x, oil-immersion) time-series images of living cells generated with TIR-FM. Image sequences are then processed through an analysis system that identifies each individual adhesion, tracks their movement through time and collects associated properties concerning the location, shape, size and intensity. As the birth, lifetime and death of each adhesion is quantified in this approach, a thorough picture of global adhesion behavior is captured.

To demonstrate the power of this approach, we focus on the molecular scaffold protein Paxillin, a core constituent of focal adhesions. Through direct interactions with both structural and regulatory components, Paxillin serves as a platform for adhesion signal transduction.[164] A principal regulatory mechanism of Paxillin is phosphorylation, with over 40 sites of phosphorylation currently identified.[165] Many of these have yet to be characterized, but those that have demonstrate strong effects on cell migration. One of these is the c-Jun N-terminal kinase (JNK) phosphorylation site Serine 178 (S178). Mutation of this residue to Alanine, or inhibition of JNK signaling, inhibits cell motility.[166, 167] More recently, it has been shown that phosphorylation of S178 enhances Paxillin's interaction with FAK and Tyrosine phosphorylation at residues 31 and 118.[168] Expression of the phosphomimetic Y31D/Y118D Paxillin can rescue the S178A mutant phenotype. This and related work hints that JNK phosphorylation of Paxillin is an early step in adhesion formation.

In this study we use our imaging analysis system to characterize FAs labeled with EGFP-Paxillin, generating high-resolution and high-content data sets of adhesion distribution, morphology, and turnover in migrating NIH 3T3 fibroblasts. Results demonstrate that we can analyze adhesions in an unbiased manner, with typically 10^3-10^4 adhesions analyzed per cell. Utilizing wild-type Paxillin as a baseline for comparison, we utilize our software to detect alterations in adhesion spatiotemporal properties in response to S178 mutation. Through this we demonstrate that the loss of this single phosphorylation site effects adhesion site formation, size and assembly rates; using large data sets, even subtle differences are easily detected at a significant level. These results further improve our understanding of JNK regulation of Paxillin dynamics as well as demonstrating the utility of appropriately designed image analysis systems in the characterization of high-content data sets.

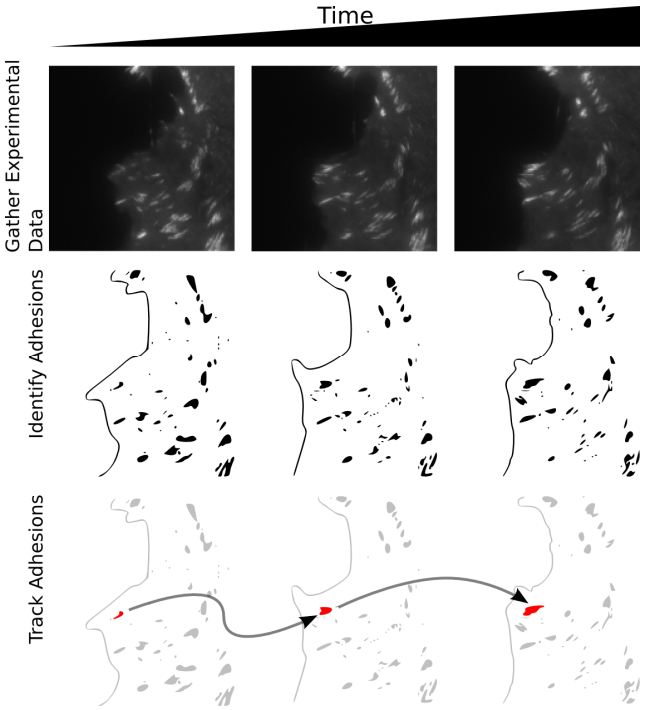

Figure 5.1. Automating the analysis of focal adhesion images requires a multi-stage pipeline. The first row shows several representative example images of fluorescently labeled Paxillin using TIR-FM micrscopy. In the second row, a cartoon depiction of the segmented adhesions and the cell edge are shown. Identification of the adhesions in each image allows a set of static morphological and fluorescence intensity based features to be extracted. The third row shows a single adhesion (highlighted in red) being tracked through the short sample time course. The properties of each adhesion are tracked over time, allowing the large scale dynamics of FA to be determined.

Results

Quantitative Analysis of TIR-FM Images of Focal Adhesions

To quantify aspects of focal adhesion spatiotemporal dynamic behavior, we first generated an NIH 3T3 fibroblast cell line expressing EGFP-Paxillin to label FA and myristolated-Red Fluorescent Protein (myr-RFP) to identify the cell edge. Cells were plated on fibronectin and imaged with TIR-FM for 1-4 hours as they exhibited motile behavior. We then implemented a multistage image analysis pipeline (Figure 5.1). Briefly, FAs were identified and segmented via a watershed-like algorithm (see Methods). Static properties of adhesions identified within each individual timepoint are quantified and include properties such as area, position and Paxillin intensity. Dynamic properties of adhesions, such as velocities and changes in fluorescent intensity, are determined by tracking and measuring adhesion properties across time steps/images. At each consecutive time step adhesion birth and death events are identified and registered by the software.

An example of the graphical output generated with this approach is shown in Figure 5.2, where a single frame of an image time series is shown, with adhesions identified through segmentation and highlighted (Figure 5.2A,B). Superimposition of adhesions across all 198 image frames from this movie is also shown (Figure 5.2C).We determined distributions for several adhesion properties including area, average EGFP-Paxillin intensity, axial ratio, distance from edge, and longevity (Figure 5.2D). In total, over 200,000 adhesion lineages were assessed. These results demonstrate that we are able to identify and quantitatively characterize large numbers of adhesions, allowing the unbiased assessment of FA behavior.

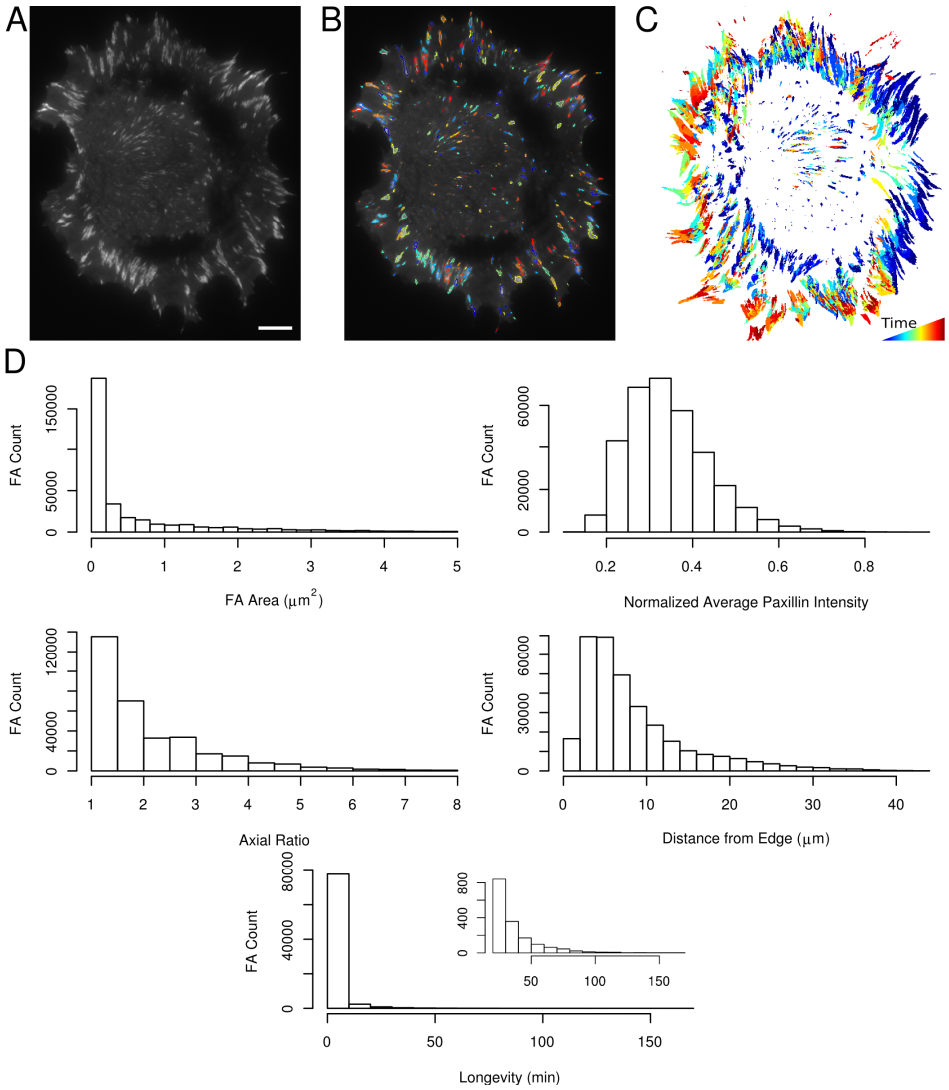

Figure 5.2. Applying quantitative image processing methods to FA images allows comprehensive characterization of FA properties. (A) One frame from a 200 minute movie of NIH 3T3 cells expressing GFP-Paxillin (the scale bar represents 10 μm). (B) The same cell as in (A), with each adhesion outlined in a different color. (C) The entire set of adhesions in an experiment can be visualized by overlaying the adhesions from each microscopy image going from the first image collected to the last image collected. This example includes the adhesions from 198 images. (D) A large range of properties can be extracted from the segmented FA, five samples are provided. The area histogram was filtered to only include adhesions with areas less than 5μm. The axial ratio histogram was filtered to only include adhesions with an axial ratio of 8 or less. The longevity histogram includes all adhesions, while the inset only includes adhesions with longevity greater than 20. The histograms include data from 21 cells.

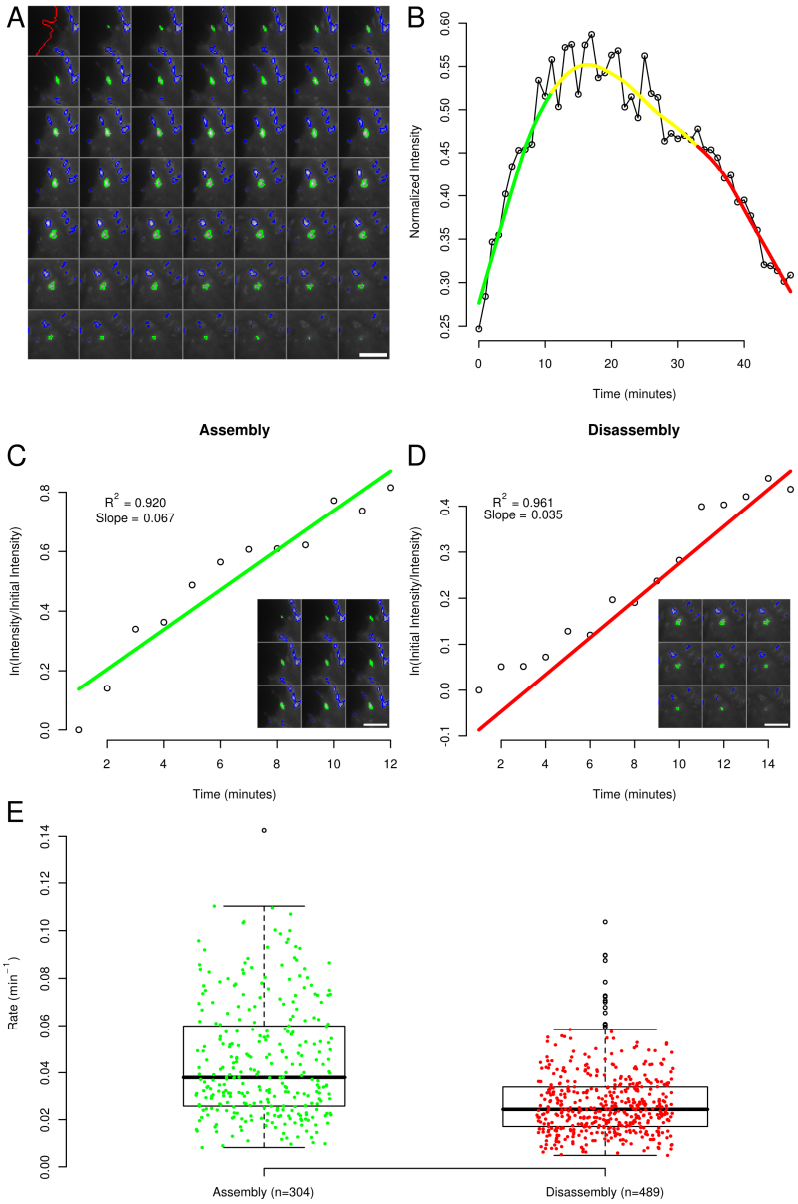

Figure 5.3. Automated measurement of focal adhesion dynamics. (A) Each of the adhesions in the cells is tracked, allowing the position and properties of single adhesions to be assessed. Here a single adhesion (in green), the surrounding adhesions (in blue) and the cell edge (in red) are followed for 49 minutes. The cell edge is only outlined in the first frame. (B) The intensity of EGFP- paxillin in the tracked adhesion in (A) through time. The red line is a smoothed fit to the data using the lowess algorithm. (C) The normalized log-linear fit of the Paxillin intensity through time during the assembly phase of the adhesion in part (B). The inset depicts several of the images from which the Paxillin intensity was gathered. (D) The normalized log-linear fit of the Paxillin intensity through time during the disassembly phase of the adhesion in part (B). The inset depicts several of the images from which the Paxillin intensity was gathered. (E) The assembly and disassembly rates for adhesions whose Paxillin intensity curve fits have R values of 0.9 or greater. The top and bottom lines of the boxplots indicate the 3 and 1 quartiles respectively, while the bold lines indicate the media values. The whiskers extend up to 1.5 times the interquartile range. The scale bar is 10 μm.

Kinetics of FA Assembly and Disassembly

Of particular importance for understanding FA function is the assessment of adhesion behavior through time. Figure 5.3A-D shows the process of determining FA assembly and disassembly rates for an individual adhesion. Figure 5.3A depicts an image series of a single adhesion (highlighted in green) progressing in 1-minute intervals from birth through maturation and death. Using time series information, we quantify the normalized intensity of each adhesion over its lifespan (Figure 5.3B). Readily apparent are the linear assembly and disassembly phases, which are automatically fit to linear log scales (see Methods for details). Our results complement previous work showing that adhesions assemble and disassemble with linear progression[158]. We found that the assembly and disassembly curves of over 50% of all adhesions analyzed (n = 1183 for assembly and n = 1486 for disassembly) could be described by a log-linear fit, showing R^2 values of 0.79 or better (Figure 5.4). In the example shown in Figure 3, linear approximation describes 92.0% and 96.1% of the variance in the rates of intensity increase and decrease, respectively (Figure 5.3C, D). In between these two phases we define a stable or stationary phase (Figure 5.3B).

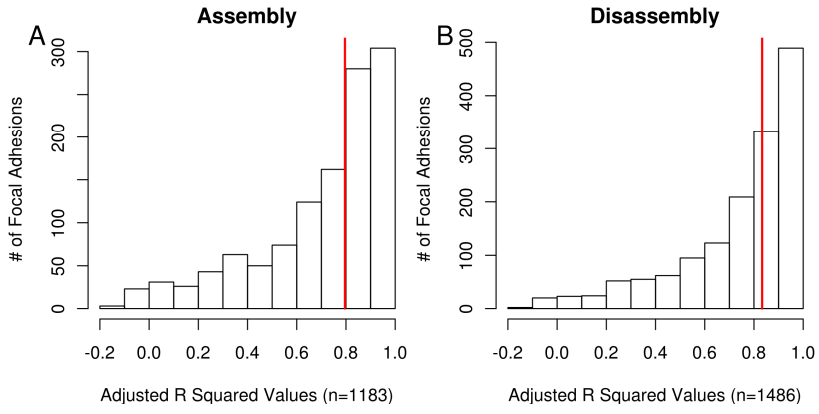

Figure 5.4. The assembly and disassembly log-linear models fit the Paxillin intensity time courses with high R values. The red lines indicate the median R values.

We utilized our system to broadly characterize the rates of FA assembly and disassembly by repeating the analysis detailed in Figure 5.3A-D on all adhesions identified by our software (n = 20 cells). Results were filtered by focusing only on FAs having lifetimes of at least 20 minutes and exhibiting near perfect log-linear fits of accumulation or decay rates ($R^2 > 0.9$; Figure 3E). These criterion yielded 304 adhesions with clearly definable assembly rates and 489 with well-defined rates of disassembly. The mean rate of assembly of 0.045±0.024 min^{-1} is 64% greater than that of disassembly (0.027±0.014 min^{-1}). It is of note that the unfiltered data set consisting of 1068 assembling and 1391 disassembling adhesions yielded similar results, with 0.031±0.023 min^{-1} and 0.020±0.014 min^{-1} (assembly 55% greater) determined for the assembly and disassembly rates, respectively. While these average rates are slower than earlier published reports, the values determined in previous studies can be found within the variance of our data set. We now provide a comprehensive picture of the breadth of adhesion assembly and disassembly dynamics in these migrating fibroblasts without biasing our analysis toward any particular subset.

Spatial Properties of FA Assembly and Disassembly

Comprehensive analysis of the dynamics of this class of prototypical adhesions allows the estimation of rates of assembly and disassembly. While this provides a view of FA behavior as a function of time, spatial aspects of FA behavior and dynamics can similarly be studied. Using the identical set of adhesions identified in the previous Paxillin kinetics analysis, we investigated the spatial property of where adhesions tend to be born or die (Figure 5.5). As seen in (5.5A), the vast majority (84%) of these adhesions

are born less than 5μm from the cell edge. In contrast, adhesions tend to die further from the edge with a mean value of 8.7μm in these experiments (B). This suggests the existence of two distinct, but partially overlapping "zones" within which preferential birth or death of FAs occurs. When looking at both FA birth/death location and assembly/disassembly rate simultaneously, we find that higher assembly rates are observed in births that occur near the edge while no obvious effect of spatial location on the rate of disassembly is apparent.

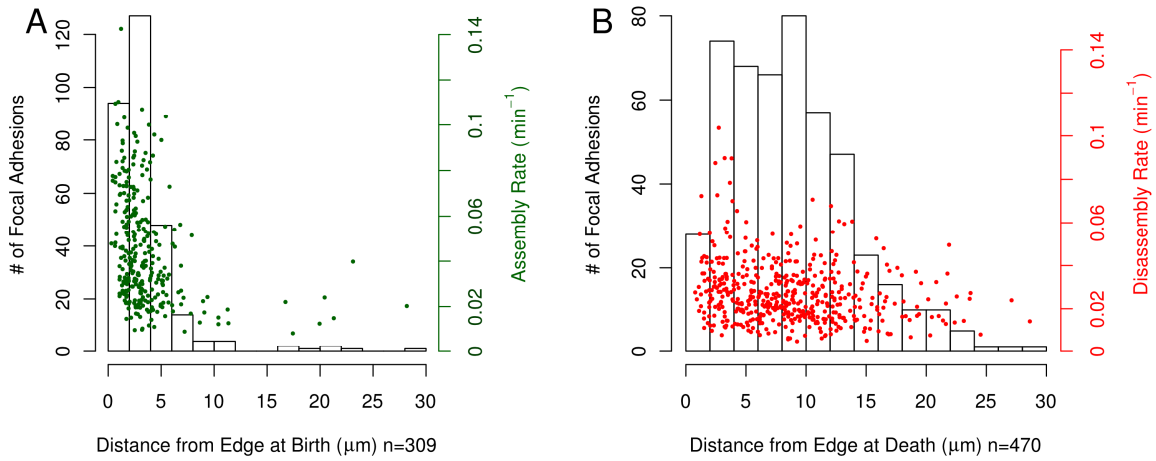

Figure 5.5. **Spatial properties of FA positions at birth and death.** The data set used for this figure consists of adhesions where the assembly and/or disassembly phases fit a log-linear model with R value of 0.9 or greater. (A) The majority of adhesions are born within 5μm of the cell edge and the greatest variance in assembly rates are also observed in this 5μm band. (B) The distribution of the distance of death location from the cell edge indicates that adhesion disassembly typically occurs along a broader band from the cell edge as compared to the position at adhesion birth. Also, the variance in disassembly rate is roughly the same regardless of the position at adhesion death.

Paxillin S178A Mutant Perturbation

We used mutation of Paxillin (Serine 178 to Alanine) as a system perturbation. As discussed earlier, this mutation blocks JNK phosphorylation of Paxillin and has known

effects on cell motility. However, the effect of this mutation on adhesion spatiotemporal dynamics has not been well characterized.

We found that the S178A mutation induced a number of significant effects on both dynamic and spatial properties of adhesions. The most dramatic of these changes is the approximately 38% reduction in the median rate of adhesion assembly (Figure 5.6A). We also observe a small (~12%) but statistically significant decrease in disassembly rate. Thus the kinetics of FA assembly is strongly affected by this mutation, but in a non-symmetric manner.

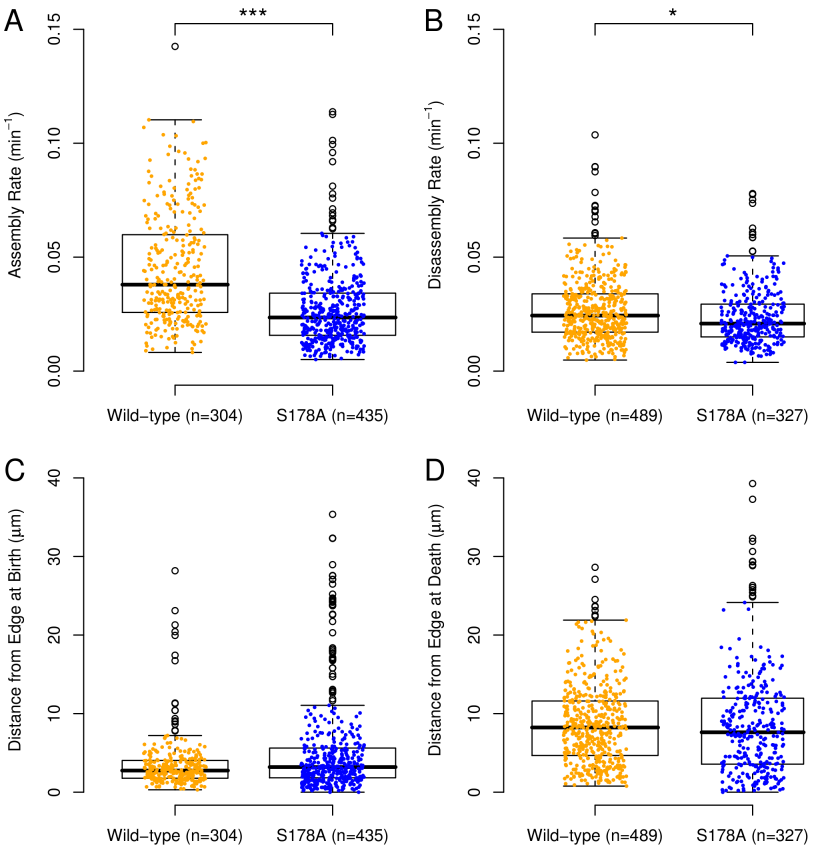

Figure 5.6 S178A mutation in Paxillin alters adhesion assembly and disassembly (A) The median assembly rate is decreased by 38% in the S178A mutants (*** indicates $p<10^{-5}$). (B) The median disassembly rate is also decreased by 14% (* indicates $p<0.01$). (C and D) The median position of adhesion centroids at birth ($p<0.1$) and death ($p<0.49$) are insignificantly affected by the S178A mutation. All p-values were calculated using the bootstrapped confidence intervals with 50000 replicates.

We previously observed that adhesions in WT cells have different distributions of birth and death position relative to the cell edge. In comparison to WT cells, we find that the median distance from the edge at birth is greater by 16% in S178A mutants (Figure 5.6C), but that this difference is not significant due to the high variance of the observed distances. There is no significant difference between WT and mutant cells with regard to where an adhesions die, suggesting that spatial aspects of the disassembly process (i.e. where disassembly occurs) is not dependent and/or sensitive to JNK phosphorylation (Figure 5.6D).

Finally, we did a lifecycle phase comparison between cells expressing WT and S178A EGFP-Paxillin. We determine that the S178A mutation causes longer lived adhesions that spend substantially longer time in the assembly phase than WT cells. There is a slight but significant ($p = 0.5$) increase in time spent in disassembly as well, but no difference in time spent in the stability phase (Figure 5.7). As a whole, our results demonstrate the most severe effects of the S178A mutation occur in the assembly phase: position at birth, assembly rate, and time spent assembling.

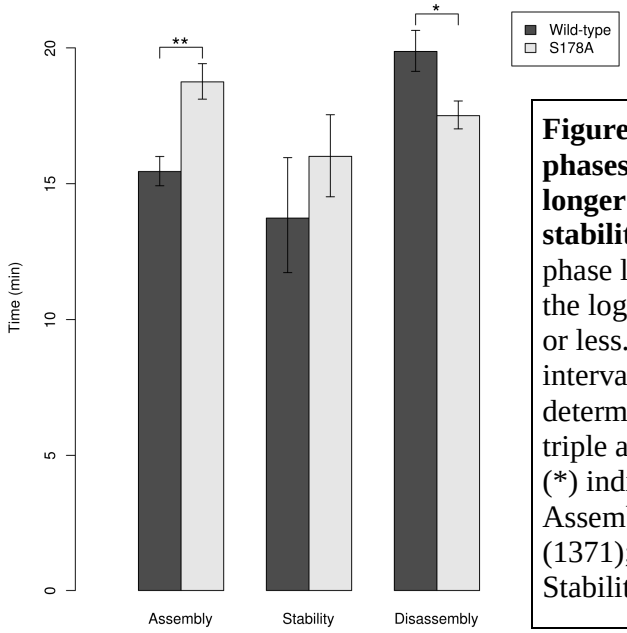

Figure 5.7. The assembly and disassembly phases in S178A mutant FAs are significantly longer than those in the wild-type, while the stability phase lengths are unaffected. The phase length values include all adhesions where the log-linear models fit with a p-value of 0.05 or less. Error bars indicate 95% confidence intervals on the mean phase length as determined through 50,000 bootstrap samples. A triple asterisk (***) indicates and single asterisk (*) indicates $p<0.05$. Wild-type N Values: Assembly (1057), Stability (456), Disassembly (1371); S178A N Values: Assembly (2089), Stability (868), Disassembly (1761).

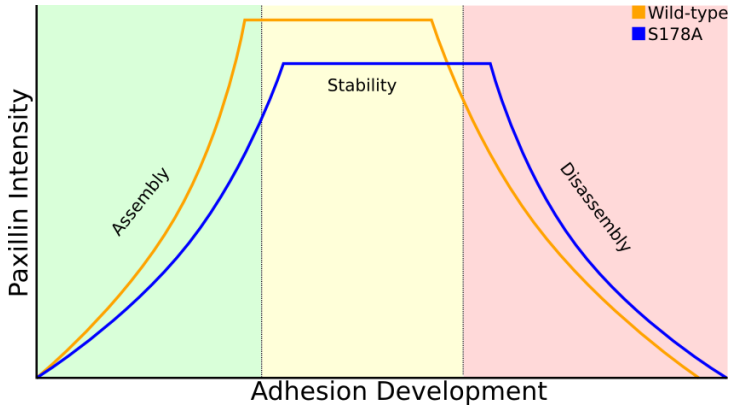

Figure 5.8. Mutations affecting the interaction of JNK with Paxillin alter the stages of FA development.

Discussion

We have described the development of a set of computational tools suitable for the global characterization of FA spatiotemporal dynamics and are well suited to assessing the results of FA signaling network perturbation on adhesion development and behavior. The S178A mutation was presented as a case study in applying these tools to analyzing complex FA phenotypes. Through this analysis, we were able to show that the S178A Paxillin mutant causes significant changes in FA assembly and disassembly rates and may help to explain the previously observed migration defects found in cells with the S178A Paxillin mutant. These changes indicate that Jun Kinase, via Paxillin, exhibits strong control over the entire FA lifecycle.

The computational tools presented allow the entire lifecycle of FAs to be analyzed. These tools include an automated adhesion detection, segmentation and tracking system; extracting a range of properties valuable for understanding FA development. The system also integrates methods capable of automatically identifying the assembly and disassembly phases of the time-lapse sequence of a FA's properties. All

of these methods were tested using simulated data that replicated many of the observed experimental processes, confirming these methods are able to accurately quantify adhesion properties under controlled conditions. The robustness of the differences detected between the wild-type and S178A mutants is preserved through a range of parameter choices for the adhesion detection limit and the minimum length of the assembly and disassembly phases. In particular, we note that all of the detected differences were maintained when using the complete set of extracted data, i.e. even when the data were not filtered for selection of long-lived adhesions. The rate at which images were taken in this work also appears to be well over the sampling rate needed to accurately measure the assembly and disassembly rates of long-lived adhesions.

We find that many of the assembly and disassembly rates detected using these automated methods encompass the rates determined using manual methods,[158] but the automated methods greatly increases the number of adhesions quantified. Differences in the mean rates detected by manual versus automated searches can be attributed to several factors. First, the rates determined using manual methods originate from user-specified adhesions of interest. Such adhesions may be chosen based on specific localization properties, such as selecting only those adhesions found within protrusions, while the presented results do not make any distinction between adhesions present in different cellular structures *a priori* (though the properties of adhesions at particular locations can be determined *a posteriori*). In addition, our analysis focused on long-lived adhesions, which might have different properties than those measured in studies of short-lived adhesions. Finally, as our software analyzes all adhesions regardless of the brightness of the adhesion, we avoid biases that may occur through, for example, preferential selection

of large and highly visible adhesions. Thus, the automated methods described greatly extend the types of adhesions that can be analyzed, as well as the range of properties that can be quantified.

The spatial properties of FA birth and death also paint an interesting picture that suggests that FAs have distinct regions where assembly and disassembly events are most concentrated. These assembly and disassembly regions overlap, but remain distinct. The greatest concentration of assembly events occur within 1.5μm of the cell edge. The assembly event range interestingly coincides with the end of the lamellipodia and the beginning of the lamella, where the structure of the actin cytoskeletal network changes significantly.

Analyzing the differences in the FAs of NIH 3T3 cells with and without a mutation that eliminates JNK phosphorylation of Paxillin *in vivo*, we were able to quantify significant differences in several relevant FA properties such as the rate of adhesion assembly and disassembly. In addition to the strong perturbations observed, several subtle changes in FA dynamics and localization were also detected. Measured differences in adhesion size were also observed in a recent siRNA screen of FA proteins that included JNK knockdown.[163] A model of FA dynamics supported by our findings is depicted in Figure 5.8. This model illustrates that the intensity of Paxillin during the stability period of the FA lifecycle is decreased compared to wild-type fibroblasts (data not shown). In this model, the S178A mutation shows distinct effects on both the assembly and disassembly phases of FA development, but these effects are different in magnitude. Determining what FA development signals are involved in perturbing the assembly, stability and disassembly processes is an ongoing process, but these proof of

principle TIR-FM experiments demonstrate the capabilities of the software analysis system.

Development of improvements and additional analysis modules related is ongoing. In prior studies, analysis of the cell edge velocity has proven to be a robust phenotype that can be used to quantify the effect of many different perturbations to the signaling networks that control cellular motility.[74] Integration of this type of data will allow the rates of cell edge movement to be analyzed in terms of FA phenotypes. Such studies will help to bridge the gap between the well-developed fields of cell edge analysis and FA dynamics. The data sets collected using the software also provide information about the specific properties of the adhesions during each phase of their lifecycle. While the "distance from cell edge" measure used here displays interesting patterns, the application of more powerful spatial statistics methods will allow the more rigorous quantification of spatial, as well as spatiotemporal properties. Such spatial methods will also be important as additional types of data, including local protein activity levels, are added to the experimental data collected.

We have described a system for quantifying FA dynamics and localization that allows high-content screening methods to be applied to understanding the perturbation of FA signaling networks. The system was applied to quantifying the differences in FA development generated through a single amino acid mutation of the FA scaffolding protein Paxillin. Future studies of other FA perturbation methods with high-content analysis methods should provide a comprehensive picture of the role of FA signaling proteins in the control of FA development and localization.

Methods

Cell Culture

NIH 3T3 fibroblasts (MEFs) and 293 LinXE ecotropic packaging cells were cultured in 5% CO^2 at 37°C in Dulbecco's modified Eagle's medium (DMEM, Mediatech) supplemented with 10% fetal calf serum, 1% L-Glutamine, and 1% penicillinstreptomycin. Fibroblasts were imaged in Ham's F-12K medium without phenol red (SAFC Biosciences) with 2% fetal bovine serum, 15mM HEPES, 1% L-Glutamine, and 1% penicillinstreptomycin.

To make stable cell lines, retroviral vectors were transfected into 293 LinXE cells plated in 6cm dishes with Fugene 6 (Roche) according to the manufacturer's protocol (using 18μL Fugene 6 and 8μg of DNA). The media was replaced after 12 hours. Viral supernatant was harvested 48 hours after media replacement, passed through a .45μm syringe filter and then added to MEFs plated at subconfluent densities at a ratio of 1:3 (viral supernatant/normal media). Cells were simultaneously infected with virus containing myr-RFP and the appropriate EGFP-Paxillin construct and went through 5-8 rounds of infection to reach expression levels sufficient for live cell imaging.

Microscopy

Prior to imaging, MEFs were plated onto coverslips coated with 5μg/mL Fibronectin (Sigma) for 30min. Fibroblasts expressing EGFP-PaxS187A required 2-3 hours to adhere to the coverslips due to a spreading defect. Immediately before being transferred to a sealed imaging chamber, complete culture media was replaced with imaging media.

Imaging was performed on an Olympus IX81 motorized inverted microscope

equipped with ZDC focus drift compensator and TIRFM illuminator, a 60X 1.45 NA PlanApoN TIRFM objective, a cooled digital 12-bit CCD camera (CoolSnap, Roper Scientific), a 100W Mercury arc lamp, and MetaMorph imaging software. The 488nm laser line from a Krypton-Argon ion laser (Series 43, Omnichrome) was controlled with a custom laser launch/AOTF (LSM Technologies).

TIRF images of EGFP and epifluorescence images of RFP were acquired using an 80/20 (TIRF / Epifluorescence) splitter mirror, a custom dichroic mirror (Chroma) and the following band-pass filters: EGFP (HQ 525/50); RFP (HQ580/30, HQ 630/40). Images were acquired with 2 x 2 binning. Illumination intensity was controlled with either the AOTF (TIRF excitation) or neutral density filters (epifluorescence excitation) until 300-1000ms exposures satisfied the dynamic range of the camera without saturation.

Image Processing

Methods to identify the FA were adapted from a prior publication[169], with some modification. Briefly, each image taken during an experiment was high pass filtered, using a round averaging filter with a radius of 11 pixels (4.95μm diameter). The high pass filtered images were threshholded by an empirically determined value set to identify adhesion pixels. The water segmentation method was used as described, but with the following modifications. When a pixel acts as bridge between two large adhesions, where large is defined as 40 or more pixels (1.85μm^2), the bridge pixel is assigned to the adhesion whose centroid is closest to the bridge pixel. Also, following addition of all pixels whose high passed image value was above threshold, pixels surrounded by adhesions were identified and added to adhesion set using the same water algorithm. Between 200 and 600 adhesions were found in each image from the experimental data.

With each focal adhesion identified all the collected images, many static adhesion properties are collected (Table 2).

Average local background fluorescence was subtracted from the average fluorescence of each adhesion to give the background correct fluorescence intensity. The local background region for a single adhesion was defined as the region within 10 pixels of the adhesion border. Pixels outside the cell, inside another adhesion or the adhesion itself were excluded from the average background fluorescence calculation.

The cell edges were found by analyzing the myr-RFP images using a method similar to that described in a prior publication.[170] Briefly, a histogram of all the intensity values for a single image was collected and split into 1000 equal sized bins. The counts of each bin were then smoothed with the loess algorithm (Polynomial order 2, 5% of data included in each fit) and the minima and maxima of the smoothed fit found. The maxima with the highest value was identified and the set of minima at intensity values greater than that the highest maxima collected. The intensity value of the minima closest to the highest maxima in intensity was used as the binary threshold cutoff for identifying the cell edge. Connected regions smaller than 10 pixels were discarded and all the holes in the binary cell edge image filled.

FA Tracking

With the focal adhesions identified in each image of the experimental data set, another series of algorithms were designed to track the focal adhesions through each sequential image. The tracking algorithm is based on a birth-death model of a FA lifetime. In each sequential image a FA can either be born, continue into the next time step, merge or die. The birth-death-merge processes are detected by examining the

properties extracted from the segmented adhesions. The results of this tracking algorithm are assignments of the FA identified in each image into lineages that track the development of the FA during the course of the experiment.

The tracking algorithm is initialized with all the adhesions detected in the first frame of the image sequence. The first step of the tracking algorithm attempts to locate FA that correspond to one another in the next time step of the experimental data (Figure Supplemental 1). This first step assumes that if a focal adhesion overlaps with a focal adhesion in the following frame, that these overlapping adhesions correspond to one another. When an adhesion overlaps with more than one adhesion in the following frame, the adhesion with the greatest percentage of overlap is assigned as the match in the next frame. If a FA does not overlap with any of the FA in the following image, the FA closest to that adhesion in terms of the Euclidean distance between each adhesion's centroid is assigned as a match. Adhesions in the next frame that are not selected via either of these methods, but still overlap with an adhesion in the current frame are marked as being created via a split birth event. Adhesion births that are the result of split events are dealt with in later filtering steps. All of the living focal adhesions are assigned a corresponding FA in the following image by these two rules.

This process of assigning live adhesions to corresponding adhesions in the following frame produces sets of adhesions that are predicted to merge. Some of these merge events are true merge events where one adhesion has joined with another, while others are adhesions which die, but are erroneously assigned as merge events. When a FA does not overlap with the FA it is predicted to become, this FA is assumed to have died and its lineage is ended. These adhesions are also marked as having undergone a death,

which will be used in later filtering steps. For the remaining merge events where more than one adhesion has been predicted to merge in the next frame, one of the merging FA lineages is selected to continue, while the other FA lineage is predicted to end. When the adhesions predicted to merge differ in size by at least 10%, the larger adhesion's lineage is continued. If the merging FAs sizes do not differ by at least 10%, the lineage whose current centroid is closer to the adhesion centroid in the following image is predicted to continue. By this sequence of rules, each merge event is resolved so that corresponding FA in adjacent experimental data images are collected.

Following tracking live adhesions and resolving the merge and death events, there remain FA in the following image which are not assigned to any of the current lineages. The unassociated FA are assigned into new lineages. This process of tracking the live adhesions, resolving merge and death events and starting new lineages is repeated for each image in the experimental data sequence until adhesion data from all the images has been included.

Calculating Assembly and Disassembly Rates

With the adhesions tracked through each experiment, the static properties determined for each adhesion in each frame of the time-lapse movie can be collected into a set of time series representing the properties of each adhesion through time. One type of time series follows the mean intensity of Paxillin through time, making it possible to estimate the rates of assembly and disassembly of Paxillin for each adhesion. An automated method to estimate the rates of assembly and disassembly was developed. This program automatically fits linear models to the log-transformed time series of Paxillin intensity values for both the assembly and disassembly phases of the FA life cycle.

In the first part of the algorithm, linear models are fit to all the possible assembly and disassembly phases of at least a user specified length. The assembly phase is assumed to occur at the beginning of the time series, whereas the disassembly phase is assumed to end with the last point in the time series. Each of the fits collected were normalized by the either first or last point in the time series and log-transformed, as described.[158]

In the second part of the algorithm, the optimum lengths of the assembly and disassembly phases were determined via a search for the maximum sum of adjusted R^2 values of the fits. It was assumed that the assembly and disassembly phases did not overlap. In the rare cases where there are multiple combinations of assembly and disassembly times that produce the highest sum of adjusted R^2 values, the combination with the longest combined assembly and disassembly times is selected.

Results Filtering

Several filters are used to analyze the data sets collected with these analysis methods. When determining the assembly and disassembly rates, only adhesions with at least 20 Paxillin intensity time points were analyzed. This ensured that there was sufficient data available to correctly detect assembly and disassembly rates. Adhesions whose birth was the result of a split event were also excluded from the assembly rate calculations, while adhesions whose lineage ended with a merge event were excluded from the disassembly rate calculation. Assembly and disassembly fits whose linear model p-values were above 0.05, indicating that the slope of the linear model was not significantly different from zero, were also excluded from the data set. Several figures

only include data from the assembly or disassembly fits whose linear models fit with an R^2 value of 0.9 or greater.

A separate set of filters were used to compile the stability phase of the adhesion lifetime data. In order to estimate the length of time an adhesion spends in the stability phase, both the assembly and disassembly phases have to be observed. There are few adhesions where both the assembly and disassembly phases fit log-linear models with high R^2 values (above 0.9), so the R^2 value requirements were excluded, but the filter did exclude adhesions were either the assembly or disassembly p-value was above 0.05.

REFERENCES

1. **Jay, D.G. Selective destruction of protein function by chromophore-assisted laser inactivation. *Proc Natl Acad Sci U S A* 85, 5454-8 (1988).**

2. **Beermann, A.E. & Jay, D.G. Chromophore-assisted laser inactivation of cellular proteins. *Methods Cell Biol* 44, 715-32 (1994).**

3. **Linden, K.G., Liao, J.C. & Jay, D.G. Spatial specificity of chromophore assisted laser inactivation of protein function. *Biophys J* 61, 956-62 (1992).**

4. **Liao, J.C., Roider, J. & Jay, D.G. Chromophore-assisted laser inactivation of proteins is mediated by the photogeneration of free radicals. *Proc Natl Acad Sci U S A* 91, 2659-63 (1994).**

5. **Jay, D.G. & Keshishian, H. Laser inactivation of fasciclin I disrupts axon adhesion of grasshopper pioneer neurons. *Nature* 348, 548-50 (1990).**

6. **Diamond, P. et al. Fasciclin I and II have distinct roles in the development of grasshopper pioneer neurons. *Neuron* 11, 409-21 (1993).**

7. **Schmucker, D., Su, A.L., Beermann, A., Jackle, H. & Jay, D.G. Chromophore-assisted laser inactivation of patched protein switches cell fate in the larval visual system of Drosophila. *Proc Natl Acad Sci U S A* 91, 2664-8 (1994).**

8. **Liao, J.C., Berg, L.J. & Jay, D.G. Chromophore-assisted laser inactivation of subunits of the T-cell receptor in living cells is spatially restricted. *Photochem Photobiol* 62, 923-9 (1995).**

9. **Wang, F.S., Wolenski, J.S., Cheney, R.E., Mooseker, M.S. & Jay, D.G. Function of myosin-V in filopodial extension of neuronal growth cones. *Science* 273, 660-3 (1996).**

10. **Lamb, R.F. et al. Essential functions of ezrin in maintenance of cell shape and lamellipodial extension in normal and transformed fibroblasts. *Curr Biol* 7, 682-8 (1997).**

11. **Castelo, L. & Jay, D.G. Radixin is involved in lamellipodial stability during nerve growth cone motility. *Mol Biol Cell* 10, 1511-20 (1999).**

12. **Liu, C.W., Lee, G. & Jay, D.G. Tau is required for neurite outgrowth and growth cone motility of chick sensory neurons. *Cell Motil Cytoskeleton* 43, 232-42 (1999).**

13. Schroder, R., Jay, D.G. & Tautz, D. Elimination of EVE protein by CALI in the short germ band insect Tribolium suggests a conserved pair-rule function for even skipped. *Mech Dev* 80, 191-5 (1999).

14. Takei, K. et al. The neural cell adhesion molecules L1 and NCAM-180 act in different steps of neurite outgrowth. *J Neurosci* 19, 9469-79 (1999).

15. Buchstaller, A. & Jay, D.G. Micro-scale chromophore-assisted laser inactivation of nerve growth cone proteins. *Microsc Res Tech* 48, 97-106 (2000).

16. Jay, D.G. The clutch hypothesis revisited: ascribing the roles of actin-associated proteins in filopodial protrusion in the nerve growth cone. *J Neurobiol* 44, 114-25 (2000).

17. Schroder, R., Jay, D.G. & Tautz, D. Elimination of EVE protein by CALI in the short germ band insect Tribolium suggests a conserved pair-rule function for even skipped. *Mech Dev* 90, 329 (2000).

18. Diefenbach, T.J. et al. Myosin 1c and myosin IIB serve opposing roles in lamellipodial dynamics of the neuronal growth cone. *J Cell Biol* 158, 1207-17 (2002).

19. Hoffman-Kim, D. et al. pp60(c-src) is a negative regulator of laminin-1-mediated neurite outgrowth in chick sensory neurons. *Mol Cell Neurosci* 21, 81-93 (2002).

20. Abe, T.K. et al. Dynactin is essential for growth cone advance. *Biochem Biophys Res Commun* 372, 418-22 (2008).

21. Iketani, M. et al. Regulation of neurite outgrowth mediated by neuronal calcium sensor-1 and inositol 1,4,5-trisphosphate receptor in nerve growth cones. *Neuroscience* 161, 743-52 (2009).

22. Beck, S. et al. Fluorophore-assisted light inactivation: a high-throughput tool for direct target validation of proteins. *Proteomics* 2, 247-55 (2002).

23. Adams, S.R. et al. New biarsenical ligands and tetracysteine motifs for protein labeling in vitro and in vivo: synthesis and biological applications. *J Am Chem Soc* 124, 6063-76 (2002).

24. Griffin, B.A., Adams, S.R. & Tsien, R.Y. Specific covalent labeling of recombinant protein molecules inside live cells. *Science* 281, 269-72 (1998).

25. **Tour, O., Meijer, R.M., Zacharias, D.A., Adams, S.R. & Tsien, R.Y. Genetically targeted chromophore-assisted light inactivation.** ***Nat Biotechnol*** **21, 1505-8 (2003).**

26. **Marek, K.W. & Davis, G.W. Transgenically encoded protein photoinactivation (FlAsH-FALI): acute inactivation of synaptotagmin I.** ***Neuron*** **36, 805-13 (2002).**

27. **Marks, K.M., Braun, P.D. & Nolan, G.P. A general approach for chemical labeling and rapid, spatially controlled protein inactivation.** ***Proc Natl Acad Sci U S A*** **101, 9982-7 (2004).**

28. **Yogo, T. et al. Selective photoinactivation of protein function through environment-sensitive switching of singlet oxygen generation by photosensitizer.** ***Proc Natl Acad Sci U S A*** **105, 28-32 (2008).**

29. **Lee, J., Yu, P., Xiao, X. & Kodadek, T. A general system for evaluating the efficiency of chromophore-assisted light inactivation (CALI) of proteins reveals Ru(II) tris-bipyridyl as an unusually efficient "warhead".** ***Mol Biosyst*** **4, 59-65 (2008).**

30. **Keppler, A. & Ellenberg, J. Chromophore-Assisted Laser Inactivation of alpha- and gamma-Tubulin SNAP-tag Fusion Proteins inside Living Cells.** ***ACS Chem Biol*** **(2009).**

31. **Rajfur, Z., Roy, P., Otey, C., Romer, L. & Jacobson, K. Dissecting the link between stress fibres and focal adhesions by CALI with EGFP fusion proteins.** ***Nat Cell Biol*** **4, 286-93 (2002).**

32. **Tanabe, T. et al. Multiphoton excitation-evoked chromophore-assisted laser inactivation using green fluorescent protein.** ***Nat Methods*** **2, 503-5 (2005).**

33. **Bulina, M.E. et al. A genetically encoded photosensitizer.** ***Nat Biotechnol*** **24, 95-9 (2006).**

34. **Carpentier, P., Violot, S., Blanchoin, L. & Bourgeois, D. Structural basis for the phototoxicity of the fluorescent protein KillerRed.** ***FEBS Lett*** **583, 2839-42 (2009).**

35. **Rodriguez, R. & Redman, R. Balancing the generation and elimination of reactive oxygen species.** ***Proc Natl Acad Sci U S A*** **102, 3175-6 (2005).**

36. **Yan, P. et al. Fluorophore-assisted light inactivation of calmodulin involves singlet-oxygen mediated cross-linking and methionine oxidation.** ***Biochemistry*** **45, 4736-48 (2006).**

37. Davies, M.J. Singlet oxygen-mediated damage to proteins and its consequences. *Biochem Biophys Res Commun* 305, 761-70 (2003).

38. Davies, M.J. Reactive species formed on proteins exposed to singlet oxygen. *Photochem Photobiol Sci* 3, 17-25 (2004).

39. McLean, M.A. et al. Mechanism of Chromophore Assisted Laser Inactivation Employing Fluorescent Proteins. *Anal Chem* (2009).

40. Surrey, T. et al. Chromophore-assisted light inactivation and self-organization of microtubules and motors. *Proc Natl Acad Sci U S A* 95, 4293-8 (1998).

41. Tour, O. EGFP as your targeted 'hitman'. *Nat Methods* 2, 491-2 (2005).

42. Giepmans, B.N., Adams, S.R., Ellisman, M.H. & Tsien, R.Y. The fluorescent toolbox for assessing protein location and function. *Science* 312, 217-24 (2006).

43. Remington, S.J. Fluorescent proteins: maturation, photochemistry and photophysics. *Curr Opin Struct Biol* 16, 714-21 (2006).

44. Guo, J., Chen, H., Puhl, H.L., 3rd & Ikeda, S.R. Fluorophore-assisted light inactivation produces both targeted and collateral effects on N-type calcium channel modulation in rat sympathetic neurons. *J Physiol* 576, 477-92 (2006).

45. Rahmanzadeh, R., Huttmann, G., Gerdes, J. & Scholzen, T. Chromophore-assisted light inactivation of pKi-67 leads to inhibition of ribosomal RNA synthesis. *Cell Prolif* 40, 422-30 (2007).

46. Stroffekova, K., Proenza, C. & Beam, K.G. The protein-labeling reagent FLASH-EDT2 binds not only to CCXXCC motifs but also non-specifically to endogenous cysteine-rich proteins. *Pflugers Arch* 442, 859-66 (2001).

47. Martin, B.R., Giepmans, B.N., Adams, S.R. & Tsien, R.Y. Mammalian cell-based optimization of the biarsenical-binding tetracysteine motif for improved fluorescence and affinity. *Nat Biotechnol* 23, 1308-14 (2005).

48. Stauffer, T.P., Ahn, S. & Meyer, T. Receptor-induced transient reduction in plasma membrane PtdIns(4,5)P2 concentration monitored in living cells. *Curr Biol* 8, 343-6 (1998).

49. Stauffer, T.P. & Meyer, T. Compartmentalized IgE receptor-mediated signal transduction in living cells. *J Cell Biol* 139, 1447-54 (1997).

50. Dormann, D., Weijer, G., Parent, C.A., Devreotes, P.N. & Weijer, C.J. Visualizing PI3 kinase-mediated cell-cell signaling during Dictyostelium development. ***Curr Biol*** **12, 1178-88 (2002).**

51. Funamoto, S., Meili, R., Lee, S., Parry, L. & Firtel, R.A. Spatial and temporal regulation of 3-phosphoinositides by PI 3-kinase and PTEN mediates chemotaxis. ***Cell*** **109, 611-23 (2002).**

52. Zaidel-Bar, R., Milo, R., Kam, Z. & Geiger, B. A paxillin tyrosine phosphorylation switch regulates the assembly and form of cell-matrix adhesions. ***J Cell Sci*** **120, 137-48 (2007).**

53. Ballestrem, C. et al. Molecular mapping of tyrosine-phosphorylated proteins in focal adhesions using fluorescence resonance energy transfer. ***J Cell Sci*** **119, 866-75 (2006).**

54. Kirchner, J., Kam, Z., Tzur, G., Bershadsky, A.D. & Geiger, B. Live-cell monitoring of tyrosine phosphorylation in focal adhesions following microtubule disruption. ***J Cell Sci*** **116, 975-86 (2003).**

55. Volberg, T., Romer, L., Zamir, E. & Geiger, B. pp60(c-src) and related tyrosine kinases: a role in the assembly and reorganization of matrix adhesions. ***J Cell Sci*** **114, 2279-89 (2001).**

56. Robles, E., Woo, S. & Gomez, T.M. Src-dependent tyrosine phosphorylation at the tips of growth cone filopodia promotes extension. ***J Neurosci*** **25, 7669-81 (2005).**

57. Pollok, B.A. & Heim, R. Using GFP in FRET-based applications. ***Trends Cell Biol*** **9, 57-60 (1999).**

58. Selvin, P.R. The renaissance of fluorescence resonance energy transfer. ***Nat Struct Biol*** **7, 730-4 (2000).**

59. Förster, T. Transfer Mechanisms of Electronic Excitation. ***Faraday Soc.*** **27, 7-17 (1959).**

60. Gordon, G.W., Berry, G., Liang, X.H., Levine, B. & Herman, B. Quantitative fluorescence resonance energy transfer measurements using fluorescence microscopy. ***Biophys J*** **74, 2702-13 (1998).**

61. Takanishi, C.L., Bykova, E.A., Cheng, W. & Zheng, J. GFP-based FRET analysis in live cells. ***Brain Res*** **1091, 132-9 (2006).**

62. Tsien, R.Y. Constructing and exploiting the fluorescent protein paintbox (Nobel Lecture). ***Angew Chem Int Ed Engl*** **48, 5612-26 (2009).**

63. Shaner, N.C., Steinbach, P.A. & Tsien, R.Y. A guide to choosing fluorescent proteins. *Nat Methods* 2, 905-9 (2005).

64. Hoffmann, C. et al. A FlAsH-based FRET approach to determine G protein-coupled receptor activation in living cells. *Nat Methods* 2, 171-6 (2005).

65. Kraynov, V.S. et al. Localized Rac activation dynamics visualized in living cells. *Science* 290, 333-7 (2000).

66. Tzima, E., Kiosses, W.B., del Pozo, M.A. & Schwartz, M.A. Localized cdc42 activation, detected using a novel assay, mediates microtubule organizing center positioning in endothelial cells in response to fluid shear stress. *J Biol Chem* 278, 31020-3 (2003).

67. Dragan, A.I. & Privalov, P.L. Use of fluorescence resonance energy transfer (FRET) in studying protein-induced DNA bending. *Methods Enzymol* 450, 185-99 (2008).

68. Chigaev, A., Buranda, T., Dwyer, D.C., Prossnitz, E.R. & Sklar, L.A. FRET detection of cellular alpha4-integrin conformational activation. *Biophys J* 85, 3951-62 (2003).

69. Coutinho, A., Garcia, C., Gonzalez-Rodriguez, J. & Lillo, M.P. Conformational changes in human integrin alphaIIbbeta3 after platelet activation, monitored by FRET. *Biophys Chem* 130, 76-87 (2007).

70. Gardiner, E.M. et al. Spatial and temporal analysis of Rac activation during live neutrophil chemotaxis. *Curr Biol* 12, 2029-34 (2002).

71. Nishiya, N., Kiosses, W.B., Han, J. & Ginsberg, M.H. An alpha4 integrin-paxillin-Arf-GAP complex restricts Rac activation to the leading edge of migrating cells. *Nat Cell Biol* 7, 343-52 (2005).

72. Del Pozo, M.A. et al. Integrins regulate GTP-Rac localized effector interactions through dissociation of Rho-GDI. *Nat Cell Biol* 4, 232-9 (2002).

73. Katsumi, A. et al. Effects of cell tension on the small GTPase Rac. *J Cell Biol* 158, 153-64 (2002).

74. Machacek, M. et al. Coordination of Rho GTPase activities during cell protrusion. *Nature* 461, 99-103 (2009).

75. Post, P.L., DeBiasio, R.L. & Taylor, D.L. A fluorescent protein biosensor of myosin II regulatory light chain phosphorylation reports a gradient of phosphorylated myosin II in migrating cells. *Mol Biol Cell* 6, 1755-68 (1995).

76. **Hall, B. et al. A fluorescence resonance energy transfer activation sensor for Arf6. *Anal Biochem* 374, 243-9 (2008).**

77. **Janetopoulos, C. & Devreotes, P. Monitoring receptor-mediated activation of heterotrimeric G-proteins by fluorescence resonance energy transfer. *Methods* 27, 366-73 (2002).**

78. **Cai, W.J. et al. Activation of the integrins alpha 5beta 1 and alpha v beta 3 and focal adhesion kinase (FAK) during arteriogenesis. *Mol Cell Biochem* 322, 161-9 (2009).**

79. **Zhang, J., Campbell, R.E., Ting, A.Y. & Tsien, R.Y. Creating new fluorescent probes for cell biology. *Nat Rev Mol Cell Biol* 3, 906-18 (2002).**

80. **Hodgson, L., Pertz, O. & Hahn, K.M. Design and optimization of genetically encoded fluorescent biosensors: GTPase biosensors. *Methods Cell Biol* 85, 63-81 (2008).**

81. **Aoki, K., Kiyokawa, E., Nakamura, T. & Matsuda, M. Visualization of growth signal transduction cascades in living cells with genetically encoded probes based on Forster resonance energy transfer. *Philos Trans R Soc Lond B Biol Sci* 363, 2143-51 (2008).**

82. **Toutchkine, A., Kraynov, V. & Hahn, K. Solvent-sensitive dyes to report protein conformational changes in living cells. *J Am Chem Soc* 125, 4132-45 (2003).**

83. **Nalbant, P., Hodgson, L., Kraynov, V., Toutchkine, A. & Hahn, K.M. Activation of endogenous Cdc42 visualized in living cells. *Science* 305, 1615-9 (2004).**

84. **Frantz, C., Karydis, A., Nalbant, P., Hahn, K.M. & Barber, D.L. Positive feedback between Cdc42 activity and H+ efflux by the Na-H exchanger NHE1 for polarity of migrating cells. *J Cell Biol* 179, 403-10 (2007).**

85. **El-Sibai, M. et al. Cdc42 is required for EGF-stimulated protrusion and motility in MTLn3 carcinoma cells. *J Cell Sci* 120, 3465-74 (2007).**

86. **Hodgson, L., Nalbant, P., Shen, F. & Hahn, K. Imaging and photobleach correction of Mero-CBD, sensor of endogenous Cdc42 activation. *Methods Enzymol* 406, 140-56 (2006).**

87. **Pawson, T. Specificity in signal transduction: from phosphotyrosine-SH2 domain interactions to complex cellular systems. *Cell* 116, 191-203 (2004).**

88. **Sells, M.A. et al. Human p21-activated kinase (Pak1) regulates actin organization in mammalian cells. *Curr Biol* 7, 202-10 (1997).**

89. **Pertz, O., Hodgson, L., Klemke, R.L. & Hahn, K.M. Spatiotemporal dynamics of RhoA activity in migrating cells.** ***Nature*** **440, 1069-72 (2006).**

90. **Poskanzer, K.E., Marek, K.W., Sweeney, S.T. & Davis, G.W. Synaptotagmin I is necessary for compensatory synaptic vesicle endocytosis in vivo.** ***Nature*** **426, 559-63 (2003).**

91. **Schafer, D.A. & Cooper, J.A. Control of actin assembly at filament ends.** ***Annu Rev Cell Dev Biol*** **11, 497-518 (1995).**

92. **Schafer, D.A. et al. Visualization and molecular analysis of actin assembly in living cells.** ***J Cell Biol*** **143, 1919-30 (1998).**

93. **Bear, J.E. et al. Negative regulation of fibroblast motility by Ena/VASP proteins.** ***Cell*** **101, 717-28 (2000).**

94. **Cooper, J.A. & Schafer, D.A. Control of actin assembly and disassembly at filament ends.** ***Curr Opin Cell Biol*** **12, 97-103 (2000).**

95. **Bear, J.E. et al. Antagonism between Ena/VASP proteins and actin filament capping regulates fibroblast motility.** ***Cell*** **109, 509-21 (2002).**

96. **Krause, M., Dent, E.W., Bear, J.E., Loureiro, J.J. & Gertler, F.B. Ena/VASP proteins: regulators of the actin cytoskeleton and cell migration.** ***Annu Rev Cell Dev Biol*** **19, 541-64 (2003).**

97. **Pollard, T.D. & Borisy, G.G. Cellular motility driven by assembly and disassembly of actin filaments.** ***Cell*** **112, 453-65 (2003).**

98. **Barzik, M. et al. Ena/VASP proteins enhance actin polymerization in the presence of barbed end capping proteins.** ***J Biol Chem*** **280, 28653-62 (2005).**

99. **Mejillano, M.R. et al. Lamellipodial versus filopodial mode of the actin nanomachinery: pivotal role of the filament barbed end.** ***Cell*** **118, 363-73 (2004).**

100. **Schafer, D.A., Korshunova, Y.O., Schroer, T.A. & Cooper, J.A. Differential localization and sequence analysis of capping protein beta-subunit isoforms of vertebrates.** ***J Cell Biol*** **127, 453-65 (1994).**

101. **Miyoshi, T. et al. Actin turnover-dependent fast dissociation of capping protein in the dendritic nucleation actin network: evidence of frequent filament severing.** ***J Cell Biol*** **175, 947-55 (2006).**

102. Rochlin, M.W., Dailey, M.E. & Bridgman, P.C. Polymerizing microtubules activate site-directed F-actin assembly in nerve growth cones. *Mol Biol Cell* 10, 2309-27 (1999).

103. Schaefer, A.W., Kabir, N. & Forscher, P. Filopodia and actin arcs guide the assembly and transport of two populations of microtubules with unique dynamic parameters in neuronal growth cones. *J Cell Biol* 158, 139-52 (2002).

104. Bashaw, G.J., Hu, H., Nobes, C.D. & Goodman, C.S. A novel Dbl family RhoGEF promotes Rho-dependent axon attraction to the central nervous system midline in Drosophila and overcomes Robo repulsion. *J Cell Biol* 155, 1117-22 (2001).

105. Edlund, M., Lotano, M.A. & Otey, C.A. Dynamics of alpha-actinin in focal adhesions and stress fibers visualized with alpha-actinin-green fluorescent protein. *Cell Motil Cytoskeleton* 48, 190-200 (2001).

106. Vignjevic, D. et al. Role of fascin in filopodial protrusion. *J Cell Biol* 174, 863-75 (2006).

107. Brown, S.S. & Spudich, J.A. Mechanism of action of cytochalasin: evidence that it binds to actin filament ends. *J Cell Biol* 88, 487-91 (1981).

108. Rubinson, D.A. et al. A lentivirus-based system to functionally silence genes in primary mammalian cells, stem cells and transgenic mice by RNA interference. *Nat Genet* 33, 401-6 (2003).

109. Gordon, G.W., Chazotte, B., Wang, X.F. & Herman, B. Analysis of simulated and experimental fluorescence recovery after photobleaching. Data for two diffusing components. *Biophys J* 68, 766-78 (1995).

110. Gonzalez, R.C. & Woods, R.E. Digital Image Processing (Addison-Wesley, Reading, MA, 1992).

111. Hinz, B., Alt, W., Johnen, C., Herzog, V. & Kaiser, H.W. Quantifying lamella dynamics of cultured cells by SACED, a new computer-assisted motion analysis. *Exp Cell Res* 251, 234-43 (1999).

112. Toutchkine, A. et al. Experimental and DFT studies: novel structural modifications greatly enhance the solvent sensitivity of live cell imaging dyes. *J Phys Chem A* 111, 10849-60 (2007).

113. Karatan, E. et al. Molecular recognition properties of FN3 monobodies that bind the Src SH3 domain. *Chem Biol* 11, 835-44 (2004).

114. Cowan-Jacob, S.W. et al. The crystal structure of a c-Src complex in an active conformation suggests possible steps in c-Src activation. *Structure* 13, 861-71 (2005).

115. Ishizawar, R. & Parsons, S.J. c-Src and cooperating partners in human cancer. *Cancer Cell* 6, 209-14 (2004).

116. Thomas, S.M. & Brugge, J.S. Cellular functions regulated by Src family kinases. *Annu Rev Cell Dev Biol* 13, 513-609 (1997).

117. Playford, M.P. & Schaller, M.D. The interplay between Src and integrins in normal and tumor biology. *Oncogene* 23, 7928-46 (2004).

118. Weis, S., Cui, J., Barnes, L. & Cheresh, D. Endothelial barrier disruption by VEGF-mediated Src activity potentiates tumor cell extravasation and metastasis. *J Cell Biol* 167, 223-9 (2004).

119. Courtneidge, S.A. Isolation of novel Src substrates. *Biochem Soc Trans* 31, 25-8 (2003).

120. Veracini, L. et al. Two distinct pools of Src family tyrosine kinases regulate PDGF-induced DNA synthesis and actin dorsal ruffles. *J Cell Sci* 119, 2921-34 (2006).

121. Timpson, P., Jones, G.E., Frame, M.C. & Brunton, V.G. Coordination of cell polarization and migration by the Rho family GTPases requires Src tyrosine kinase activity. *Curr Biol* 11, 1836-46 (2001).

122. DerMardirossian, C., Rocklin, G., Seo, J.Y. & Bokoch, G.M. Phosphorylation of RhoGDI by Src regulates Rho GTPase binding and cytosol-membrane cycling. *Mol Biol Cell* 17, 4760-8 (2006).

123. Martinez-Quiles, N., Ho, H.Y., Kirschner, M.W., Ramesh, N. & Geha, R.S. Erk/Src phosphorylation of cortactin acts as a switch on-switch off mechanism that controls its ability to activate N-WASP. *Mol Cell Biol* 24, 5269-80 (2004).

124. Bouton, A.H., Riggins, R.B. & Bruce-Staskal, P.J. Functions of the adapter protein Cas: signal convergence and the determination of cellular responses. *Oncogene* 20, 6448-58 (2001).

125. Frame, M.C., Fincham, V.J., Carragher, N.O. & Wyke, J.A. v-Src's hold over actin and cell adhesions. *Nat Rev Mol Cell Biol* 3, 233-45 (2002).

126. Fincham, V.J. & Frame, M.C. The catalytic activity of Src is dispensable for translocation to focal adhesions but controls the turnover of these structures during cell motility. *EMBO J* 17, 81-92 (1998).

127. Seong, J. et al. Visualization of Src activity at different compartments of the plasma membrane by FRET imaging. *Chem Biol* 16, 48-57 (2009).

128. Wang, Y. et al. Visualizing the mechanical activation of Src. *Nature* 434, 1040-5 (2005).

129. Gardner, O.S., Dewar, B.J., Earp, H.S., Samet, J.M. & Graves, L.M. Dependence of peroxisome proliferator-activated receptor ligand-induced mitogen-activated protein kinase signaling on epidermal growth factor receptor transactivation. *J Biol Chem* 278, 46261-9 (2003).

130. Rizzo, M.A., Springer, G.H., Granada, B. & Piston, D.W. An improved cyan fluorescent protein variant useful for FRET. *Nat Biotechnol* 22, 445-9 (2004).

131. Buccione, R., Orth, J.D. & McNiven, M.A. Foot and mouth: podosomes, invadopodia and circular dorsal ruffles. *Nat Rev Mol Cell Biol* 5, 647-57 (2004).

132. Veracini, L. et al. Two functionally distinct pools of Src kinases for PDGF receptor signalling. *Biochem Soc Trans* 33, 1313-5 (2005).

133. Cary, L.A., Klinghoffer, R.A., Sachsenmaier, C. & Cooper, J.A. SRC catalytic but not scaffolding function is needed for integrin-regulated tyrosine phosphorylation, cell migration, and cell spreading. *Mol Cell Biol* 22, 2427-40 (2002).

134. Malo, G.D. et al. X-ray structure of Cerulean GFP: a tryptophan-based chromophore useful for fluorescence lifetime imaging. *Biochemistry* 46, 9865-73 (2007).

135. Zhou, F.Q. & Snider, W.D. Intracellular control of developmental and regenerative axon growth. *Philos Trans R Soc Lond B Biol Sci* 361, 1575-92 (2006).

136. Song, H.J. & Poo, M.M. Signal transduction underlying growth cone guidance by diffusible factors. *Curr Opin Neurobiol* 9, 355-63 (1999).

137. Jaffe, A.B. & Hall, A. Rho GTPases: biochemistry and biology. *Annu Rev Cell Dev Biol* 21, 247-69 (2005).

138. Etienne-Manneville, S. & Hall, A. Rho GTPases in cell biology. *Nature* 420, 629-35 (2002).

139. Mueller, B.K., Mack, H. & Teusch, N. Rho kinase, a promising drug target for neurological disorders. *Nat Rev Drug Discov* 4, 387-98 (2005).

140. Gallo, G. RhoA-kinase coordinates F-actin organization and myosin II activity during semaphorin-3A-induced axon retraction. *J Cell Sci* 119, 3413-23 (2006).

141. McKerracher, L. & Higuchi, H. Targeting Rho to stimulate repair after spinal cord injury. *J Neurotrauma* 23, 309-17 (2006).

142. Loudon, R.P., Silver, L.D., Yee, H.F., Jr. & Gallo, G. RhoA-kinase and myosin II are required for the maintenance of growth cone polarity and guidance by nerve growth factor. *J Neurobiol* 66, 847-67 (2006).

143. Yuan, X.B. et al. Signalling and crosstalk of Rho GTPases in mediating axon guidance. *Nat Cell Biol* 5, 38-45 (2003).

144. Birkenfeld, J. et al. GEF-H1 modulates localized RhoA activation during cytokinesis under the control of mitotic kinases. *Dev Cell* 12, 699-712 (2007).

145. Woo, S. & Gomez, T.M. Rac1 and RhoA promote neurite outgrowth through formation and stabilization of growth cone point contacts. *J Neurosci* 26, 1418-28 (2006).

146. Arakawa, Y. et al. Control of axon elongation via an SDF-1alpha/Rho/mDia pathway in cultured cerebellar granule neurons. *J Cell Biol* 161, 381-91 (2003).

147. Sebok, A. et al. Different roles for RhoA during neurite initiation, elongation, and regeneration in PC12 cells. *J Neurochem* 73, 949-60 (1999).

148. Suter, D.M., Schaefer, A.W. & Forscher, P. Microtubule dynamics are necessary for SRC family kinase-dependent growth cone steering. *Curr Biol* 14, 1194-9 (2004).

149. Buck, K.B. & Zheng, J.Q. Growth cone turning induced by direct local modification of microtubule dynamics. *J Neurosci* 22, 9358-67 (2002).

150. Zhou, F.Q., Zhou, J., Dedhar, S., Wu, Y.H. & Snider, W.D. NGF-induced axon growth is mediated by localized inactivation of GSK-3beta and functions of the microtubule plus end binding protein APC. *Neuron* 42, 897-912 (2004).

151. Rubinson, D.A. et al. A lentivirus-based system to functionally silence genes in primary mammalian cells, stem cells and transgenic mice by RNA interference. *Nat Genet* 33, 401-6 (2003).

152. Wen, Y. et al. EB1 and APC bind to mDia to stabilize microtubules downstream of Rho and promote cell migration. *Nat Cell Biol* 6, 820-30 (2004).

153. Palazzo, A.F., Cook, T.A., Alberts, A.S. & Gundersen, G.G. mDia mediates Rho-regulated formation and orientation of stable microtubules. *Nat Cell Biol* 3, 723-9 (2001).

154. Bement, W.M., Benink, H.A. & von Dassow, G. A microtubule-dependent zone of active RhoA during cleavage plane specification. *J Cell Biol* 170, 91-101 (2005).

155. Bayless, K.J. & Davis, G.E. Microtubule depolymerization rapidly collapses capillary tube networks in vitro and angiogenic vessels in vivo through the small GTPase Rho. *J Biol Chem* 279, 11686-95 (2004).

156. Krendel, M., Zenke, F.T. & Bokoch, G.M. Nucleotide exchange factor GEF-H1 mediates cross-talk between microtubules and the actin cytoskeleton. *Nat Cell Biol* 4, 294-301 (2002).

157. Qi, Y., Wang, J.K., McMillian, M. & Chikaraishi, D.M. Characterization of a CNS cell line, CAD, in which morphological differentiation is initiated by serum deprivation. *J Neurosci* 17, 1217-25 (1997).

158. Webb, D.J. et al. FAK--Src signalling through paxillin, ERK and MLCK regulates adhesion disassembly. *Nature Cell Biology* 6 (2004).

159. Nayal, A. et al. Paxillin phosphorylation at Ser273 localizes a GIT1-PIX-PAK complex and regulates adhesion and protrusion dynamics. *J Cell Biol* 173, 587-9 (2006).

160. Bryce, N.S. et al. Cortactin promotes cell motility by enhancing lamellipodial persistence. *Curr Biol* 15, 1276-85 (2005).

161. Paran, Y. et al. High-throughput screening of cellular features using high-resolution light-microscopy; Application for profiling drug effects on cell adhesion. *Journal of Structural Biology* 158 (2007).

162. Zamir, E., Geiger, B. & Kam, Z. Quantitative Multicolor Compositional Imaging Resolves Molecular Domains in Cell-Matrix Adhesions. *PLoS ONE* 3, e1901 (2008).

163. Winograd-Katz, S.E., Itzkovitz, S., Kam, Z. & Geiger, B. Multiparametric analysis of focal adhesion formation RNAi-mediated gene knockdown. *J. Cell Biol.* 186 (2009).

164. Brown, M.C. & Turner, C.E. Paxillin: adapting to change. *Physiol Rev* 84, 1315-39 (2004).

165. Webb, D.J. et al. Paxillin phosphorylation sites mapped mass spectrometry. *Journal of Cell Science* 118 (2005).

166. Huang, C., Rajfur, Z., Borchers, C., Schaller, M.D. & Jacobson, K. JNK phosphorylates paxillin and regulates cell migration. *Nature* 424, 219-23 (2003).

167. Kimura, K., Teranishi, S., Yamauchi, J. & Nishida, T. Role of JNK-dependent serine phosphorylation of paxillin in migration of corneal epithelial cells during wound closure. *Invest Ophthalmol Vis Sci* 49, 125-32 (2008).

168. Huang, Z., Yan, D.P. & Ge, B.X. JNK regulates cell migration through promotion of tyrosine phosphorylation of paxillin. *Cell Signal* 20, 2002-12 (2008).

169. Zamir, E. et al. Molecular diversity of cell-matrix adhesions. *J Cell Sci* 112 (1999).

170. Machacek, M. & Danuser, G. Morphodynamic Profiling of Protrusion Phenotypes. *Biophys. J.* 90 (2006).